Corrected 1 July 2024. See full text.

RESEARCH ARTICLE

NANOMATERIALS

Carbon nanotube fibers with dynamic strength up to 14 GPa

Xinshi Zhang[1,2]†, Xudong Lei[3,4]†, Xiangzheng Jia[5]†, Tongzhao Sun[2,6], Jiajun Luo[1,2], Shichen Xu[1,2], Lijun Li[2], Dan Yan[1,2], Yuanlong Shao[1,2], Zhenzhong Yong[7,8,9], Yongyi Zhang[7,8,9]*, Xianqian Wu[3,4]*, Enlai Gao[5]*, Muqiang Jian[2]*, Jin Zhang[1,2]*

High dynamic strength is of fundamental importance for fibrous materials that are used in high–strain rate environments. Carbon nanotube fibers are one of the most promising candidates. Using a strategy to optimize hierarchical structures, we fabricated carbon nanotube fibers with a dynamic strength of 14 gigapascals (GPa) and excellent energy absorption. The dynamic performance of the fibers is attributed to the simultaneous breakage of individual nanotubes and delocalization of impact energy that occurs during the high–strain rate loading process; these behaviors are due to improvements in interfacial interactions, nanotube alignment, and densification therein. This work presents an effective strategy to utilize the strength of individual carbon nanotubes at the macroscale and provides fresh mechanism insights.

Ultrahigh dynamic strength and energy-absorbing fibrous materials are needed in high–strain rate applications, such as ballistic impact and untraceable debris impact on aircraft and spacecraft (*1*, *2*). The impact resistance of fibrous materials is closely related to the hierarchical structures, starting from individual building blocks at the nanoscale, then moving to microfibrils, and finally to the macroscopic ensembles, which provide various methods to dissipate the mechanical energy. A few high-performance fibers, such as ultrahigh–molecular weight polyethylene (UHMWPE), poly(*p*-phenylene-2,6-benzobisoxazole) (PBO), and aramid fibers (*3*, *4*), have been developed and play vital roles in modern industries. Despite these achievements, the fabrication of higher-performance fibers is still driven by increasing industrial demands. One promising route is the assembly of ultrahigh-performance nanomaterials into macroscopic architectures (*5*, *6*).

Carbon nanotubes (CNTs) with an intrinsic strength of more than 100 GPa (*7*, *8*) have been considered as promising building blocks for constructing high-performance and multifunctional fibers for applications in both quasi-static and dynamic environments (*2*, *9*–*13*). For example, Xie *et al.* (*2*) demonstrated the potential applications of CNT fibers (CNTFs) for high–strain rate environments using a stroboscopic quantification method. Three spinning methods are used to fabricate CNTFs, including wet spinning (*14*, *15*), vertically aligned array spinning (*16*), and direct aerogel spinning (*17*). Among them, direct aerogel spinning is promising for the continuous and scalable fabrication of ultrastrong fibers consisting of high–aspect ratio CNTs (*18*–*20*). However, the quasi-static and dynamic mechanical properties of CNTFs are limited by the poor interfacial interactions, low nanotube alignment, and high porosity formed in the spinning process (*21*–*24*). To solve these issues, various posttreatment approaches have been developed to modify the hierarchical structures of CNTFs (*25*, *26*), including solution densification (*27*, *28*), mechanical treatment (*20*), and thermal annealing (*29*). However, the tensile strength of CNTFs (<10 GPa), especially the dynamic strength, is far lower than that of individual CNTs (>100 GPa), indicating that there is still plenty of room for improving the strength of CNTFs.

We developed a strategy that includes progressive stretching, infusion with PBO nanofibers and molecular chains (hereafter PBOs), and mechanical rolling to improve the interfacial interactions, nanotube alignment, densification of CNTFs (Fig. 1A and fig. [illegible]). Briefly, functionalized CNTFs (F-CNTFs) are first immersed in chlorosulfonic acid (CSA) solution containing PBOs and swell visibly owing to the protonation effect (*30*). Afterward, PBOs are infused into F-CNTFs during the progressive stretching treatment (PBO-CNTFs). Finally, mechanical rolling is used to densify PBO-CNTFs (D-PBO-CNTFs) (*31*). This approach can be used to continuously produce high-performance tows (Fig. 1B and fig. S2). Our experimental characterizations demonstrate that the as-obtained fibers have a highly ordered and densely packed structure with strong interfacial interactions (Fig. 1, C and D). Consequently, D-PBO-CNTFs exhibit a high quasi-static tensile strength of 8.2 ± 0.2 GPa and a toughness of 170.3 ± 17.9 MJ m^{-3}, yielding a 355% increase in the tensile strength and a 106% increase in the toughness compared with F-CNTFs (Fig. 1E). The resultant fibers exhibit a dynamic strength of 14.0 ± 0.7 GPa and a toughness of 462.6 ± 102.1 MJ m^{-3} under a high strain rate of about 1400 s^{-1}, values that are higher than those of commercial fibers (e.g., 7.2 ± 0.8 GPa and 295.0 ± 59.5 MJ m^{-3} for PBO fibers, 4.6 ± 0.2 GPa and 174.6 ± 11.6 MJ m^{-3} for Kevlar 29 fibers tested under the same conditions as D-PBO-CNTFs; Fig. 1E).

Fabrication and structure of CNTFs

We first produced continuous CNTFs by floating catalyst chemical vapor deposition (fig. S3A) (*17*). The as-spun fibers contained impurities such as metallic catalyst particles and amorphous carbon (fig. S3B). To purify and functionalize these fibers with oxygen-containing functional groups (e.g., hydroxy groups), we adopted the posttreatments of weak oxidation and acid washing (fig. S1A). Through these treatments, thermogravimetric analyses demonstrated that most of the residual impurities in F-CNTFs had been removed (fig. S4), and Raman spectra and x-ray photoelectron spectroscopy (XPS) of F-CNTFs confirmed the functionalization of CNTs (figs. S5 and S6 and table S1) (*31*). Compared with the pristine fibers, F-CNTFs produced by the purification process exhibited a more compact structure (fig. S7), and the as-obtained fibers subjected to a 12-hour oxidation treatment exhibited an improved tensile strength (fig. S8 and table S1); these fibers were chosen as the raw fibers for further optimization in the following investigation.

When immersed in a CSA bath, F-CNTFs swell by side-wall protonation (fig. S9), which offers plenty of room to rearrange the entangled and porous networks for the improvements of alignment and densification of fibers. By subjecting F-CNTFs to CSA treatment for 10 min with a stretching ratio of 20%, the as-obtained CSA-CNTFs exhibited a substantial

[1]Beijing National Laboratory for Molecular Sciences, School of Materials Science and Engineering, College of Chemistry and Molecular Engineering, Peking University, Beijing 100871, China. [2]Beijing Graphene Institute (BGI), Beijing 100095, China. [3]Institute of Mechanics, Chinese Academy of Sciences, Beijing 100190, China. [4]School of Engineering Science, University of Chinese Academy of Sciences, Beijing 100049, China. [5]Department of Engineering Mechanics, School of Civil Engineering, Wuhan University, Wuhan 430072, China. [6]State Key Laboratory of High-efficiency Coal Utilization and Green Chemical Engineering, College of Chemistry and Chemical Engineering, Ningxia University, Yinchuan 750021, China. [7]Key Laboratory of Multifunctional Nanomaterials and Smart Systems, Advanced Materials Division, Suzhou Institute of Nano-Tech and Nano-Bionics, Chinese Academy of Sciences, Suzhou 215123, China. [8]Division of Nanomaterials and Jiangxi Key Lab of Carbonene Materials, Jiangxi Insitute of Nanotechnology, Nanchang 330200, China. [9]School of Nano-Tech and Nano-Bionics, University of Science and Technology of China, Hefei 230026, China.
*Corresponding author. Email: yyzhang2011@sinano.ac.cn (Y.Z.); wuxianqian@imech.ac.cn (X.W.); enlaigao@whu.edu.cn (E.G.); jianmq-cnc@pku.edu.cn (M.J.); jinzhang@pku.edu.cn (J.Z.)
†These authors contributed equally to this work.

Corrected 28 June 2024. See full text.

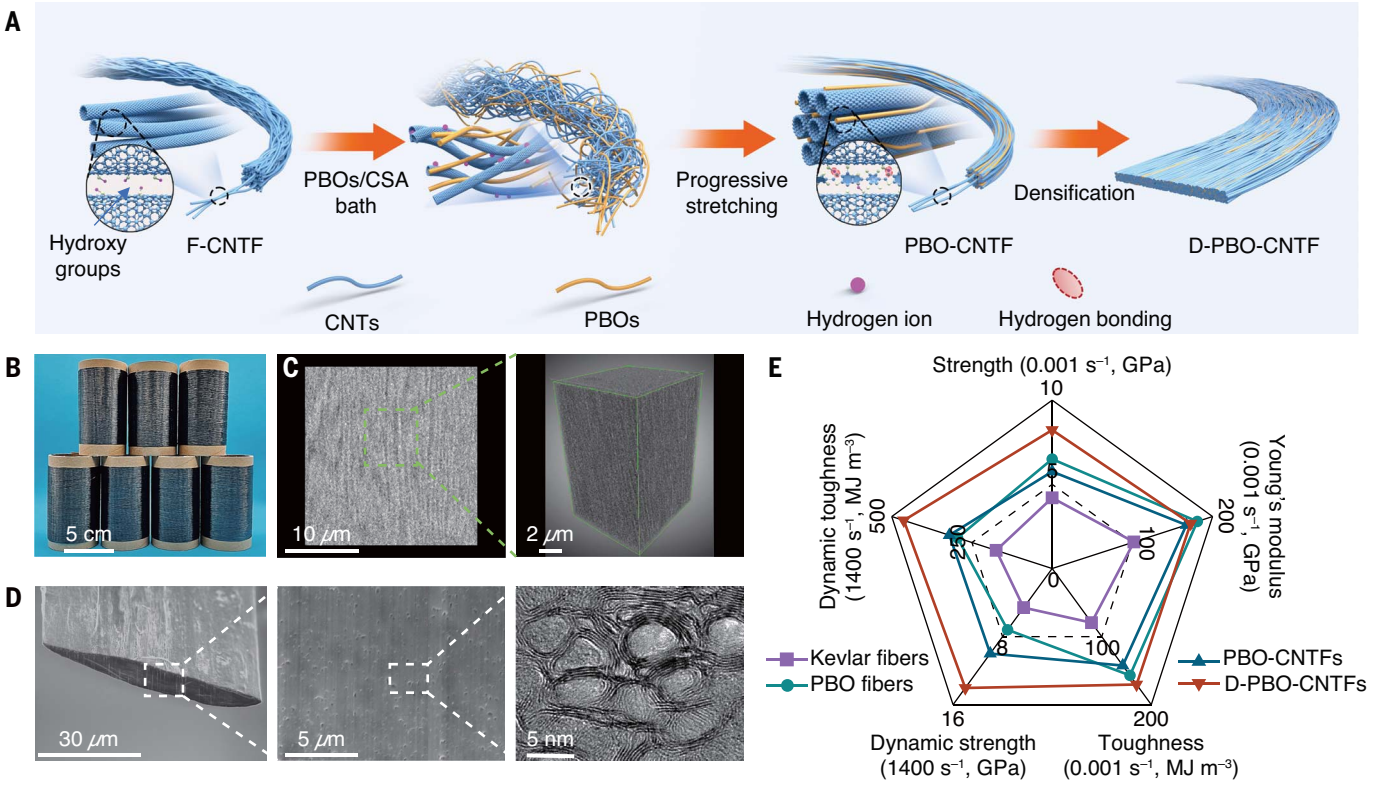

Fig. 1. Preparation, morphology, and mechanical properties of CNTFs. (**A**) Strategy to develop highly packed and well-aligned CNTFs. (**B**) Digital photograph of PBO-CNTF tows. (**C**) Three-dimensionally reconstructed void microstructure (right) derived from nano-CT results (left) for D-PBO-CNTFs. (**D**) SEM (left and middle) and TEM (right) images of the radial cross section of D-PBO-CNTF cut by a focused ion beam. (**E**) Radar chart for comparing the mechanical performance of different CNTFs and commercial fibers (PBO and Kevlar 29 fibers).

improvement in tensile strength (figs. S10 and S11 and tables S2 and S3). Furthermore, a progressive stretching treatment was introduced. After optimizing the drawing speeds under a certain stretching process, longitudinal scanning electron microscopy (SEM) and transmission electron microscopy (TEM) images showed that the CNTs yield an increase in the alignment along the fiber axial direction (fig. S12). Herman's orientation factor (*f*) values measured by wide-angle x-ray scattering (WAXS) also support an improvement in the alignment of CNTs. The *f* for CSA-CNTFs obtained at an optimized stretching rate of 3% per min was 0.90, higher than that of F-CNTFs (0.66) and other fibers prepared at higher drawing speeds (fig. S13 and table S4) (*31*). This might be because the mechanical treatment at a low drawing speed provides adequate time to disentangle and reorient the CNTs, resulting in the enhancement of tensile strength, Young's modulus, and toughness (fig. S14 and table S5). Solely progressive stretching treatment cannot fully eliminate the voids, as shown in the CSA-CNTFs (fig. S16A). To address this issue, PBOs were infused into CNTFs by uniformly dissolving PBO fibers in a CSA bath at different weight percentages (wt %) (fig. S15) during the progressive stretching treatment. Both the elemental analyses and thermogravimetric analyses demonstrated that PBO-CNTFs treated in the PBOs-CSA solution with a PBO concentration of 0.05 wt % exhibited the highest PBO content (fig. S17 and table S6). Such PBO-CNTFs showed high densification (fig. S16), alignment (Fig. 2A and fig. S18), and mechanical properties (fig. S19 and table S7). Optimal D-PBO-CNTFs were fabricated by applying mechanical rolling on these PBO-CNTFs.

We compared the alignment, densification, and interfacial interactions of F-CNTFs, CSA-CNTFs, PBO-CNTFs, and D-PBO-CNTFs. First, we investigated the alignment of these fibers. The orientation factors measured by WAXS for CSA-CNTFs (0.90), PBO-CNTFs (0.94), and D-PBO-CNTFs (0.92) were higher than that for F-CNTFs (0.66), which is consistent with results of polarized Raman spectra (fig. S20). This indicates that the PBOs-assisted progressive stretching treatment can effectively improve the alignment of CNTs along the fiber axis (Fig. 2, B to D, and table S8). Second, the densification of these fibers was evaluated by small-angle x-ray scattering (SAXS) (*32*), which indicated that D-PBO-CNTFs have the densest structure (fig. S21). We also reconstructed the microstructures of fibers using nanoscale x-ray computed tomography (nano-CT) and measured the porosities accordingly (Fig. 2, F and H, fig. S22, and movies S1 to S4). The porosities of F-CNTFs (4.8%), CSA-CNTFs (2.7%), and PBO-CNTFs (1.9%) are higher than that of D-PBO-CNTFs (1.0%). These results are consistent with the cross-sectional SEM images, SAXS characterization, and density measurements (Fig. 2, E and G, and table S9). Third, we explored the interfacial interactions by Fourier transform infrared spectroscopy (FTIR) spectra. The redshift of the hydroxy group peak indicated the hydrogen-bond interactions between CNTs and PBOs (fig. S23A).

Performance of CNTFs

The structural optimization endows the fibers with improvements in quasi-static mechanical properties and electrical conductivities. D-PBO-CNTFs have a tensile strength of 8.2 ± 0.2 GPa, a Young's modulus of 172.7 ± 9.6 GPa, a toughness of 170.3 ± 17.9 MJ m^{-3}, and an electrical conductivity of 2.9×10^6 S m^{-1}, which are 4.6, 1.7, 2.1, and 5.8 times those of F-CNTFs (1.8 ± 0.2 GPa, 99.8 ± 7.3 GPa, 82.5 ± 6.4 MJ m^{-3}, and 0.5×10^6 S m^{-1}; Fig. 3, A and B, and table S9), respectively. F-CNTFs show an intertube slippage failure morphology, whereas D-PBO-CNTFs exhibit a failure morphology with much fewer pull-out bundles (fig. S24).

Corrected 28 June 2024. See full text.

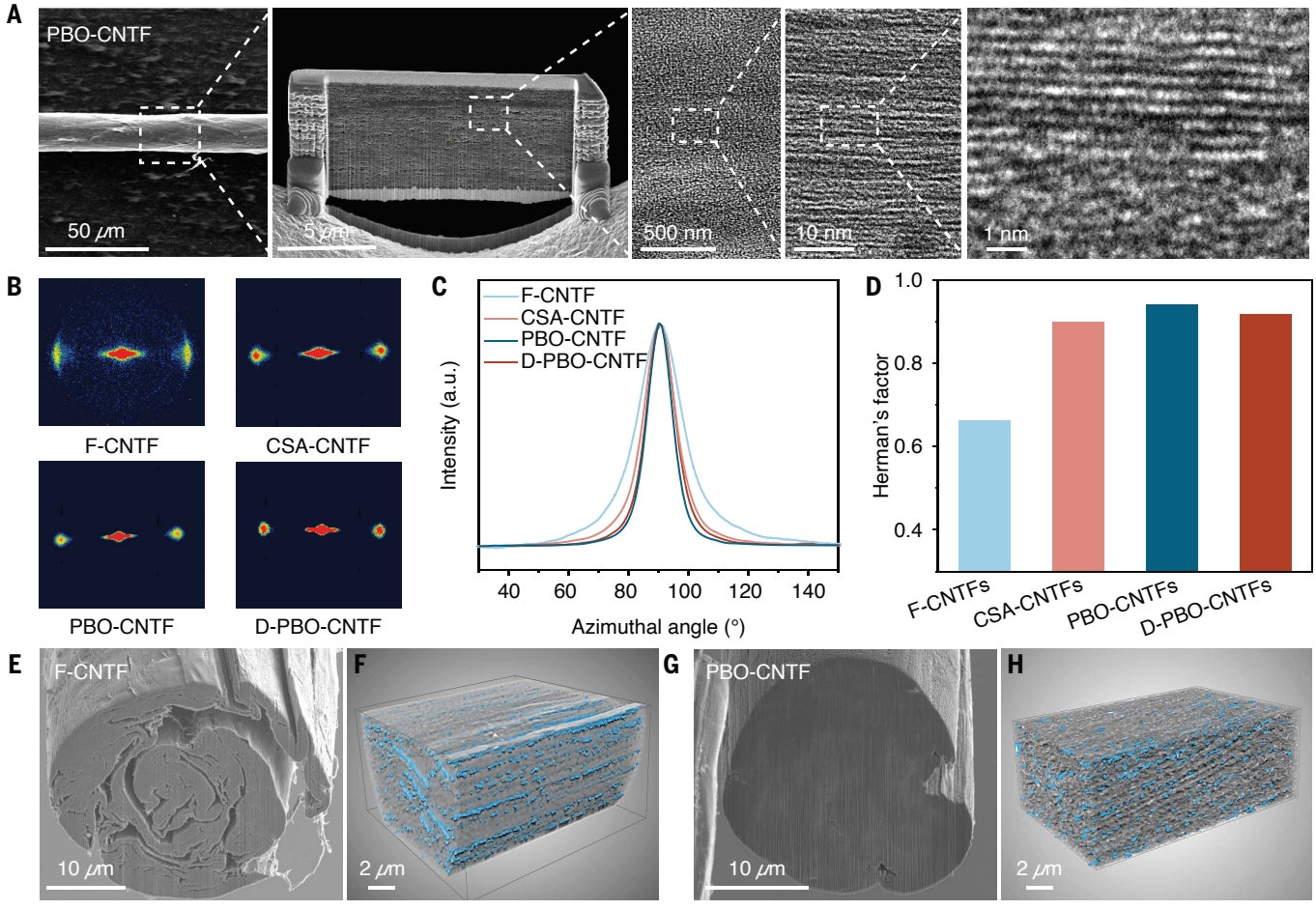

Fig. 2. Structural characterization of CNTFs. (**A**) SEM (two images on the left) and TEM (remaining) images of the axial cross section of PBO-CNTFs cut by a focused ion beam. (**B**) WAXS patterns of F-CNTFs, CSA-CNTFs, PBO-CNTFs, and D-PBO-CNTFs. (**C**) Azimuthal intensity profile of different fibers. a.u., arbitrary units. (**D**) Comparison of the alignment of CNTs within fibers. (**E** and **G**) SEM images of cross sections cut by a focused ion beam for F-CNTFs (E) and PBO-CNTFs (G). (**F** and **H**) Three-dimensional void microstructures reconstructed by nano-CT (blue represents the internal voids) for F-CNTFs (F) and PBO-CNTFs (H).

From the ultrahigh quasi-static mechanical properties, we can further estimate the ballistic resistance of fibers via Cunniff velocity (c^*) = $[(\sigma\varepsilon/2\rho)(E/\rho)^{1/2}]^{1/3}$ (*4*), where σ, ε, E, and ρ are tensile strength, elongation at break, Young's modulus, and density of fibers, respectively. These data show that D-PBO-CNTFs have the best potential for the application of ballistic-resistant materials (Fig. 3C and table S11). It should be noted that c^* is a rough estimation because it depends on the loading rates and local plastic deformation (*2*). More accurately, the high–strain rate performance of fibers was investigated using a mini-split Hopkinson tension bar (figs. S25 to S27) (*3*, *31*). The shape of stress-strain curves of CNTFs at the high strain rates (Fig. 3D), that is, the stress after the peak value does not drop suddenly, is different from that at quasi-static loading (Fig. 3A). This is because CNTFs have insufficient time to regulate rate-sensitive conformations, such as disentanglement, reorientation, and slippage of nanotubes, thus exhibiting a "cascade-like" breaking of individual CNTs (*22*, *33*). Compared with the quasi-static strength, D-PBO-CNTFs exhibit a dynamic strength of 9.2 ± 0.8, 11.0 ± 0.7, and 14.0 ± 0.7 GPa at strain rates of about 500, 950, and 1400 s^{-1}, which increase by 12.2, 34.1, and 70.7%, respectively. This indicates an improvement in strengthening efficiency as the strain rate increases (table S12). The dynamic strength of D-PBO-CNTFs at a strain rate of about 1400 s^{-1} is 6.1, 2.3, and 1.4 times that of F-CNTFs, CSA-CNTFs, and PBO-CNTFs, respectively (Fig. 3, D and E), and substantially surpasses those of all other high-performance fibers (Fig. 3F and table S12). Meanwhile, the dynamic toughness of D-PBO-CNTFs reaches 462.6 ± 102.1 MJ m^{-3} (Fig. 3G), which exceeds that of other high-performance fibers (*34*, *35*). Furthermore, the fracture morphologies show that the intertube slippage of CNTFs at the high strain rates is inhibited, and PBO-CNTFs and D-PBO-CNTFs exhibit a ductile-to-brittle transition in the fracture mode (fig. S28) (*22*, *31*).

To directly assess the impact resistance of these fibers, we performed laser-induced high-velocity transverse impact testing (Fig. 3H and figs. S31 and S32). The specific energy dissipation power (SEDP) of a single fiber, which is equal to 7.5 × 10^{10} kg^{-1} multiplied by its transverse velocity (c_T), is a figure of merit to evaluate its dynamic energy absorption capacity (figs. S29 and S30) (*2*, *31*), where c_T is the transverse velocity. It is challenging to accurately measure the SEDP of D-PBO-CNTFs with a narrow ribbon-like cross section because it depends on the bending resistance along the impact direction (fig. S33 and table S13). Hence, we only compared the SEDP values of the other three fibers. Among these fibers, PBO-CNTFs have the highest SEDP value [(8.7 ± 1.0) × 10^{13} m kg^{-1} s^{-1}; Fig. 3I and table S14] (*2*). The impact resistance of PBO-CNTFs is attributed to the high longitudinal wave speed. Finite element simulations demonstrated that the high longitudinal wave speed [$c_L = (E/\rho)^{1/2}$ = 11.4 km s^{-1}] helps to delocalize the impact energy (fig. S34, A and B), which is consistent with experimental results (fig. S32 and table S14). After the high-velocity transverse impact, the craters on the surface of PBO-CNTFs are

Corrected 28 June 2024. See full text.

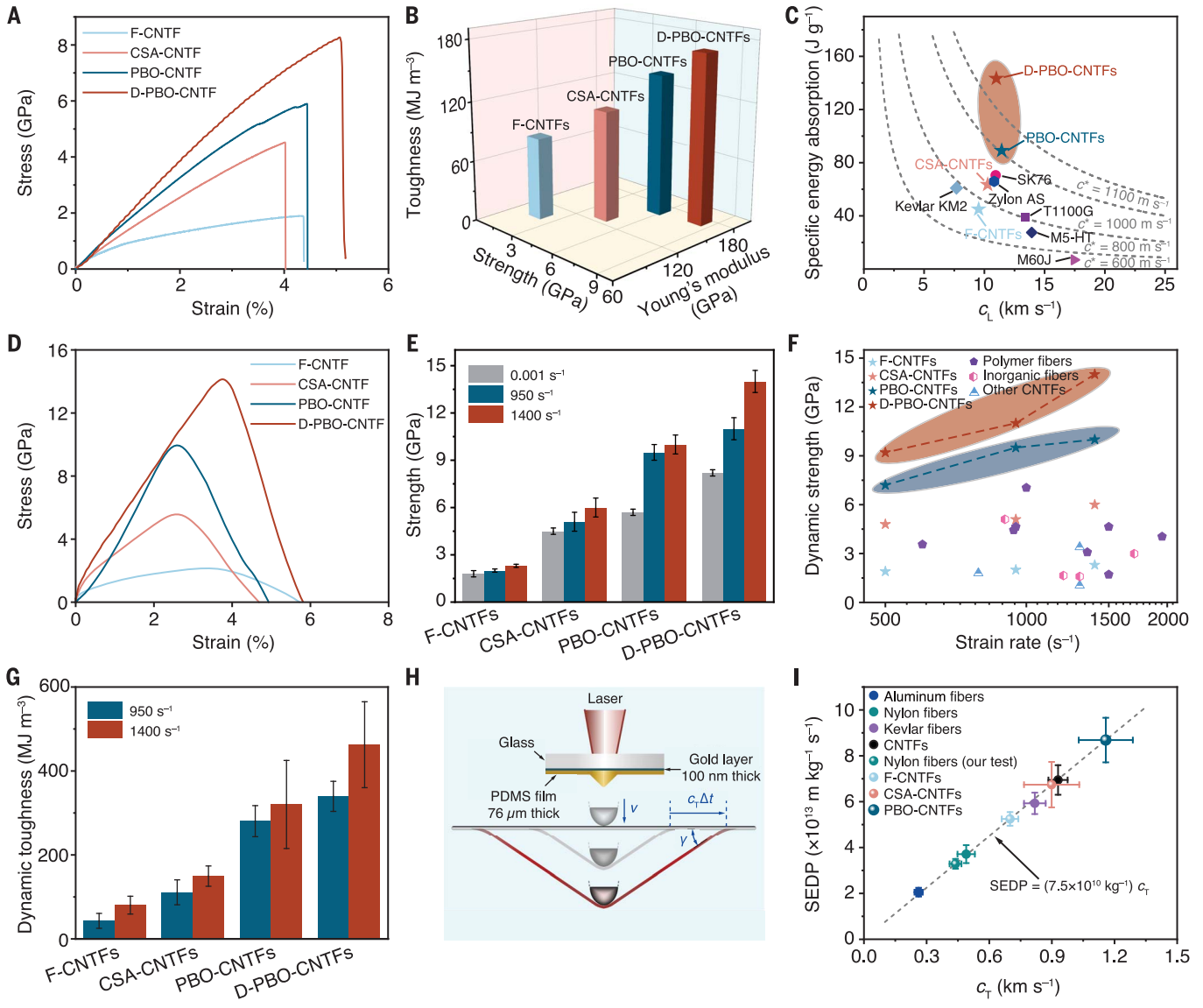

Fig. 3. Mechanical properties of CNTFs. (**A**) Quasi-static stress-strain curves of F-CNTFs, CSA-CNTFs, PBO-CNTFs, and D-PBO-CNTFs. (**B**) Comparison of quasi-static tensile strength, Young's modulus, and toughness of different CNTFs. (**C**) Comparison of specific energy absorption and longitudinal wave velocity of our fibers (indicated by stars) and other high-performance fibers. (**D**) Stress-strain curves of F-CNTFs, CSA-CNTFs, PBO-CNTFs, and D-PBO-CNTFs at high strain rates of about 1400 s^{-1}. (**E**) Comparison of the strength of CNTFs at different strain rates. Error bars indicate the standard deviation of the means of independent measurements. (**F**) Comparison of the dynamic strength of our fibers and other high-performance fibers at high strain rates. (**G**) Comparison of the dynamic toughness of CNTFs at different strain rates. Error bars indicate the standard deviation of the means of independent measurements. (**H**) Schematic diagram of laser-induced high-velocity transverse impact on a single fiber. Here, PDMS, v, Δt, and γ represent polydimethylsiloxane, impact velocity, interval time, and deflection angle, respectively. (**I**) SEDP values of different fibers. Error bars indicate the standard deviation.

not visible compared with those on CSA-CNTFs (fig. S34, C and D), suggesting that the high dynamic strength of PBO-CNTFs helps to maintain the structural integrity.

Strengthening mechanism of CNTFs

To further determine whether covalent bonds are broken, we measured Raman mapping spectra on the impact region of the fibers and observed an increase in the I_D/I_G value (fig. S37), where I_D is the intensity of D-band and I_G is the intensity of G-band, which is a signal of bond breaking or atomic rearrangement that also contributes to dissipating energy (*2*, *36*–*38*). The analyses we describe next show that the simultaneous breakage of CNTs is of central importance to achieving ultrahigh dynamic performance, which results from improvements in interfacial interactions, nanotube alignment, and densification of CNTFs. Regarding the interfacial interactions, we performed experiments using in situ Raman spectroscopy and stress relaxation. When the applied strain of F-CNTFs is less than 1.3%, the G-band frequency in the Raman spectra shows a small downshift. Afterward, a plateau region extends from 1.3 to 2.5% (Fig. 4A), indicating that the further increase of applied strain does not transfer the stress into CNTs. For CSA-CNTFs, because both the alignment and densification are improved compared with F-CNTFs, the plateau region extends from 2.5 to 3.3% (fig. S38A). By contrast, there is a continuous strengthening stress

Corrected 28 June 2024. See full text.

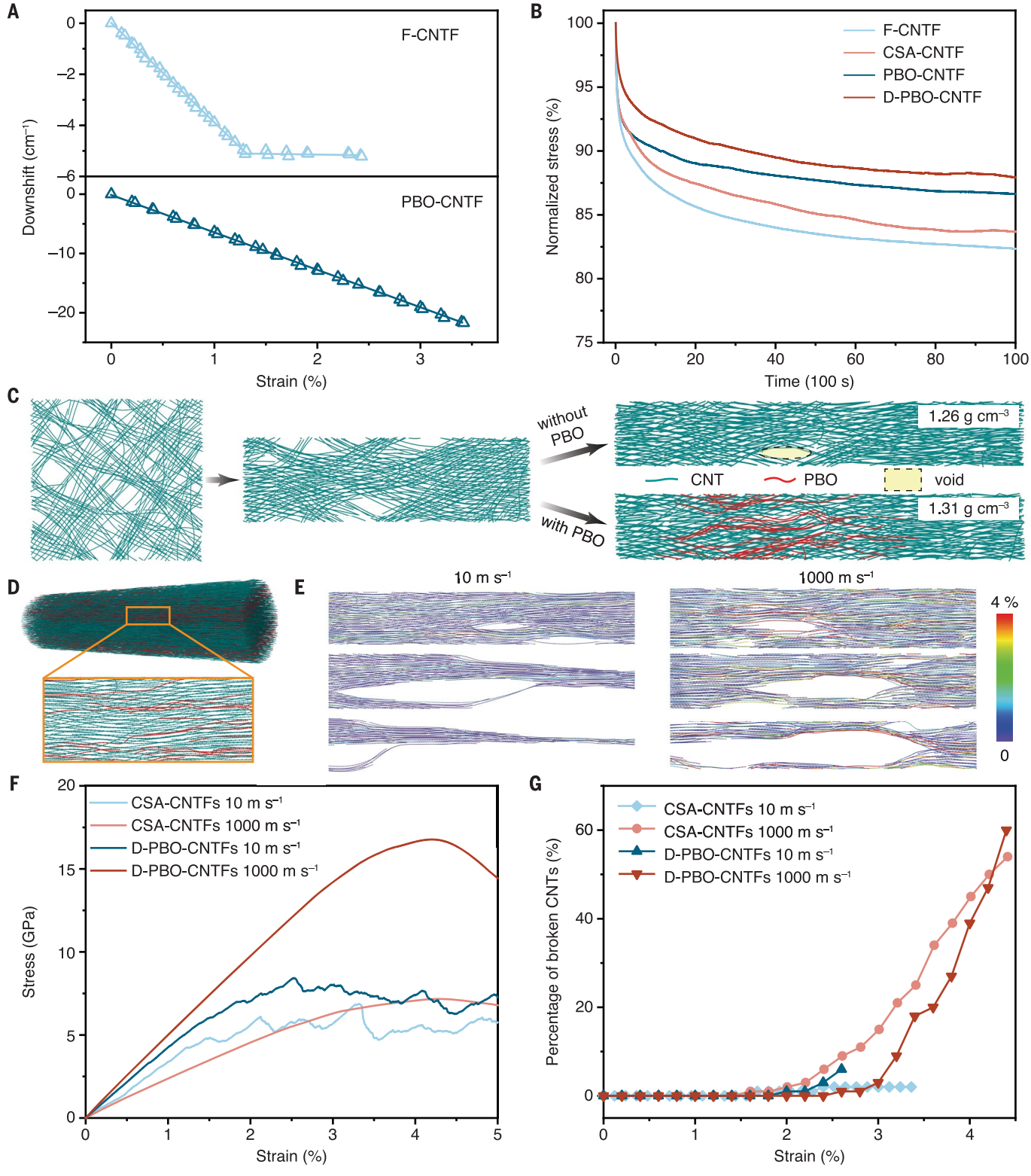

Fig. 4. Mechanistic analyses of the dynamic performance of CNTFs. (**A**) Dependence of Raman frequency downshifts on the applied strains for F-CNTFs and PBO-CNTFs. (**B**) Stress-relaxation curves of different fibers at 1.5% strain. (**C**) Simulation snapshots of progressive stretching treatment for CNTFs with and without PBO. (**D**) Structures and cross-sectional morphology of the simulated model. (**E**) Snapshots of deformed D-PBO-CNTFs under low (left) and high (right) loading velocities. The atoms are colored according to the bond strain. (**F**) Stress-strain curves of CSA-CNTFs and D-PBO-CNTFs under low and high loading velocities. (**G**) Percentage of broken CNTs for CSA-CNTFs and D-PBO-CNTFs during the tensile process, which is counted up to the peak stress in the stress-strain curves.

transfer to CNTs over the whole strain range for PBO-CNTFs and D-PBO-CNTFs, and the downshift per unit strain is about twice as high in PBO-CNTFs and D-PBO-CNTFs compared with F-CNTFs and CSA-CNTFs (Fig. 4A and fig. S38). Meanwhile, D-PBO-CNTFs show the highest resistance to stress relaxation (Fig. 4B). The increased load transfer efficiency suggests that there are strong interfacial interactions between PBOs and CNTs. We also investigated the interfacial interactions by atomistic simulations. At the nanoscale, our calculations show that the persistence lengths of multiwalled CNTs and PBOs are 1.9×10^6 and 38 nm, respectively, which are generally consistent with prior reports (*39*, *40*). These results indicate that PBOs are much more flexible than CNTs. The discrepancy in flexibility between PBOs and CNTs implies that PBOs would preferentially adsorb onto the rigid CNTs (figs. S39 and S40). The combination of relatively flexible PBOs and relatively rigid CNTs would result in an increased effective contact area. Meanwhile, the interfacial energy between PBOs and CNTs (71.2 meV per atom) is also higher than that between two CNTs (55.5 meV per atom). Consequently, the increased contact area and interfacial energy account for the improvements in interfacial interactions and load transfer efficiency (fig. S41).

We explored the effect of nanotube alignment and densification on the behavior of CNTFs using coarse-grained molecular dynamics (CGMD) simulations. The simulations of progressive stretching treatment show that the fibers undergo a reorganization of microstructures—including curving, reorientation, straightening, and sliding of nanotubes and bundles—toward a more uniform, compact, and ordered structure (Fig. 4C and fig. S42). As shown in Fig. 4C, the voids are observed in CNTFs without the addition of PBOs, whereas these voids are filled in CNTFs with the addition of PBOs. This leads to an increase in simulated densities from 1.26 to 1.31 g cm^{-3}, values that are generally consistent with experimental characterizations of CSA-CNTFs (1.24 g cm^{-3}) and PBO-CNTFs (1.28 g cm^{-3}), as summarized in table S9. Meanwhile, the alignment of CNTs in CGMD simulations is also improved from 0.91 for CSA-CNTFs to 0.93 for PBO-CNTFs, which is attributed to an increased load transfer efficiency due to the addition of PBOs. These simulations are generally consistent with our above experimental characterizations of the alignment and densification. Finally, we did tensile tests of fibers under low and high loading velocities (Fig. 4, D to F). The strain distributions show that the strain primarily localizes at the slippage region under the low loading velocity, whereas CNTs deform more uniformly under the high loading velocity (Fig. 4E). Our simulations demonstrate that the tensile strength of D-PBO-CNTFs under low and high loading velocities is 8.4 and 16.3 GPa, respectively (Fig. 4F). To understand the macroscopic performance of CNTFs under low and high loading velocities, we performed analyses by tracking the microscopic behaviors of each CNT within the fibers. Figure 4G shows that under the low loading velocity, only about 2 and 6% of CNTs within CSA-CNTFs and D-PBO-CNTFs, respectively, break (*31*), indicating that the slippage of nanotubes dominates the failure. By comparison, under the high loading velocity, CNTFs have insufficient time to fully regulate rate-sensitive conformations, such as disentanglement, reorientation, and slippage of nanotubes, which results in a high percentage of CNTs breaking. Up to the peak stress, about 54 and 60% of CNTs break for CSA-CNTFs and D-PBO-CNTFs, respectively. The percentage of broken CNTs within CSA-CNTFs is higher than that broken within D-PBO-CNTFs before a strain of about 4%. This is because the inferior structure of CSA-CNTFs leads to stress concentration as well as premature breakage of CNTs. The breakage of CNTs within the D-PBO-CNTFs is much more simultaneous than that within CSA-CNTFs, and the percentage of broken CNTs within the D-PBO-CNTFs becomes larger after a strain of about 4% (Fig. 4G). This simultaneous breakage of CNTs within the D-PBO-CNTFs under a high loading velocity originates from the improvements in interfacial interactions, alignment, and densification, which accounts for the high dynamic strength of these fibers.

Summary

We developed a strategy to fabricate CNTFs with a dynamic strength of 14 GPa. This strategy leads to improvements in interfacial interactions, nanotube alignment, and densification within the fibers. Multiscale analyses combined with experimental evidence revealed that the dynamic performance of CNTFs is primarily due to the simultaneous breakage of individual nanotubes and the exceptional impact-energy delocalization that occurs during the high–strain rate loading process. Our work provides a feasible route to harness the intrinsic strength of individual CNTs at the macroscale to fabricate impact-resistant fibrous materials.

REFERENCES AND NOTES

1. S. Eswarappa Prameela *et al*., *Nat. Rev. Mater.* **8**, 81–88 (2023).
2. W. Xie *et al*., *Nano Lett.* **19**, 3519–3526 (2019).
3. J. Luo *et al*., *Nat. Commun.* **14**, 3019 (2023).
4. Y. Q. Li, H. L. Fan, X. L. Gao, *Compos. Part B* **238**, 109890 (2022).
5. B. Fang, D. Chang, Z. Xu, C. Gao, *Adv. Mater.* **32**, e1902664 (2020).
6. I. A. Kinloch, J. Suhr, J. Lou, R. J. Young, P. M. Ajayan, *Science* **362**, 547–553 (2018).
7. B. Peng *et al*., *Nat. Nanotechnol.* **3**, 626–631 (2008).
8. Y. Bai *et al*., *Science* **369**, 1104–1106 (2020).
9. Y. Wen *et al*., *Nano Lett.* **22**, 6035–6047 (2022).
10. J. Mu *et al*., *Science* **365**, 150–155 (2019).
11. H. Chu *et al*., *Science* **371**, 494–498 (2021).
12. C. Chen *et al*., *Chem. Rev.* **123**, 613–662 (2023).
13. L. W. Taylor *et al*., *Nano Lett.* **21**, 7093–7099 (2021).
14. N. Behabtu *et al*., *Science* **339**, 182–186 (2013).
15. S. G. Kim *et al*., *Carbon* **196**, 59–69 (2022).
16. M. Zhang, K. R. Atkinson, R. H. Baughman, *Science* **306**, 1358–1361 (2004).
17. Y. L. Li, I. A. Kinloch, A. H. Windle, *Science* **304**, 276–278 (2004).
18. H. G. Chae, S. Kumar, *Science* **319**, 908–909 (2008).
19. K. Koziol *et al*., *Science* **318**, 1892–1895 (2007).
20. W. Xu, Y. Chen, H. Zhan, J. N. Wang, *Nano Lett.* **16**, 946–952 (2016).
21. J. J. Vilatela, J. A. Elliott, A. H. Windle, *ACS Nano* **5**, 1921–1927 (2011).
22. D. Y. Wang *et al*., *J. Mech. Phys. Solids* **173**, 105241–105267 (2023).
23. P. F. Wang *et al*., *Carbon* **102**, 18–31 (2016).
24. X. P. Hu *et al*., *Compos. Commun.* **28**, 100933 (2021).
25. Y. Jung, Y. S. Cho, J. W. Lee, J. Y. Oh, C. R. Park, *Compos. Sci. Technol.* **166**, 95–108 (2018).
26. J. S. Bulmer, A. Kaniyoor, J. A. Elliott, *Adv. Mater.* **33**, e2008432 (2021).
27. J. Lee *et al*., *Nat. Commun.* **10**, 2962 (2019).
28. X. Zhang *et al*., *Sci. Adv.* **8**, eabq3515 (2022).
29. D. Lee *et al*., *Sci. Adv.* **8**, eabn0939 (2022).
30. Y. J. Wang, S. Xia, H. Li, J. F. Wang, *Adv. Funct. Mater.* **29**, 1903876 (2019).
31. Materials and methods are available as supplementary materials.
32. J. Qiu *et al*., *ACS Nano* **7**, 8412–8422 (2013).
33. Y. N. Zhang, L. X. Zheng, G. Z. Sun, Z. Y. Zhan, K. Liao, *Carbon* **50**, 2887–2893 (2012).
34. J. Lim, W. W. Chen, J. Q. Zheng, *Polym. Test.* **29**, 701–705 (2010).
35. M. Cheng, W. N. Chen, T. Weerasooriya, *J. Eng. Mater. Technol.* **127**, 197–203 (2005).
36. W. B. Lu, T. Chou, B. Kim, *Phys. Rev. B* **83**, 134113 (2011).
37. N. G. Chopra *et al*., *Nature* **377**, 135–138 (1995).
38. S. Ozden *et al*., *Nano Lett.* **14**, 4131–4137 (2014).
39. N. Fakhri, D. A. Tsyboulski, L. Cognet, R. B. Weisman, M. Pasquali, *Proc. Natl. Acad. Sci. U.S.A.* **106**, 14219–14223 (2009).
40. D. B. Roitman, M. McAdon, *Macromolecules* **26**, 4381–4383 (1993).

ACKNOWLEDGMENTS

We thank T. Zhou and S. Qu for providing CNTF samples and participating in discussions. We thank H. Lu for helpful discussions. We are grateful for technical support for Nano-X from Suzhou Institute of Nano-Tech and Nano-Bionics (SINANO), Chinese Academy of Sciences, and Carl Zeiss (Shanghai) Management Co., Ltd. The numerical calculations in this work were done on the supercomputing system in the Supercomputing Center of Wuhan University. **Funding:** This work was supported by Ministry of Science and Technology of China grants 2022YFA1203302 and 2022YFA1203304; National Natural Science Foundation of China grants 52202032, 52021006, T2188101, 52102035, 12272391, and 12232020; Beijing Natural Science Foundation grant 2222094; Strategic Priority Research Program of CAS grant XDB36030100; and Beijing National Laboratory for Molecular Sciences grant BNLMS-CXTD-202001. **Author contributions:** Conceptualization: J.Z., M.J., X.Z.; Methodology: X.Z., X.L., X.J., T.S., J.L., S.X., L.L., D.Y.; Investigation: X.Z., X.L., X.J.; Visualization: X.Z., X.L., and X.J.; Supervision: J.Z., M.J., E.G., X.W., Y.Z.; Writing – original draft: X.Z., X.L., X.J.; Writing – review and editing: J.Z., M.J., E.G., X.W., Y.Z., Y.S., Z.Y. **Competing interests:** The authors declare that they have no competing interests. **Data and materials availability:** All data are available in the main text or the supplementary materials.

SUPPLEMENTARY MATERIALS

science.org/doi/10.1126/science.adj1082
Materials and Methods
Supplementary Text
Figs. S1 to S42
Tables S1 to S17
References (*41*–*64*)
Movies S1 to S4

Submitted 7 June 2023; resubmitted 29 February 2024
Accepted 10 May 2024
10.1126/science.adj1082

Science
AAAS

Supplementary Materials for

Carbon nanotube fibers with dynamic strength up to 14 GPa

Xinshi Zhang *et al*.

Corresponding authors: Yongyi Zhang, yyzhang2011@sinano.ac.cn; Xianqian Wu, wuxianqian@imech.ac.cn; Enlai Gao, enlaigao@whu.edu.cn; Muqiang Jian, jianmq-cnc@pku.edu.cn; Jin Zhang, jinzhang@pku.edu.cn

Science **384**, 1318 (2024)
DOI: 10.1126/science.adj1082

The PDF file includes:

Other Supplementary Material for this manuscript includes the following:

Table of Contents

Materials and Methods

Preparation of the pristine carbon nanotube fibers (CNTFs)

The as-spun CNTFs were prepared by the floating catalyst chemical vapor deposition method (*17*). The diameter of the reactor tube was 100 mm and the length of the high-temperature reaction zone was 760 mm. The precursor solution containing a liquid carbon source (typically, acetone) with dissolved ferrocene (Aladdin, 99%) and thiophene (Aladdin, 99%) was injected uniformly into the reactor tube at a rate of 30 mL h^{-1} and carried into the high-temperature zone by a mixture of hydrogen and argon (5 L min^{-1}). The CNTs were formed in the reaction zone at 1300 ℃ and further assembled into the hollow cylinder-like aerogels. Then the aerogels formed continuous fibers as they were passing through the water bath, and the CNTFs were collected on a bobbin with a spinning rate ranging from 15 to 25 m min^{-1}. Finally, the CNTFs were dried at 400 ℃.

Preparation of F-CNTFs

The pristine CNTFs were first treated in H_2O_2 solution (Macklin, 30%) at 60 ℃ and washed with deionized water to remove the amorphous carbon and introduce the oxygen-containing functional groups. Based on the different treatment time (6, 12, and 24 h, respectively), the following three fibers were obtained: H_2O_2-6 h-CNTFs, H_2O_2-12 h-CNTFs, and H_2O_2-24 h-CNTFs. The oxidized fibers were immersed in acid to remove the iron catalyst impurities. Then the fibers were washed with deionized water and dried in an oven at 120 ℃ under an air atmosphere to remove the residual water, and the F-CNTFs were finally obtained.

Preparation of CSA-CNTFs

The F-CNTFs were first immersed into chlorosulfonic acid (CSA) solution (Aladdin, 99.5%) for varying durations (5, 10, and 20 min), and their mechanical properties were explored to determine the proper immersion time. Then the effect of stretching ratios (5%, 10%, 20%, and 25%) on the tensile strength of F-CNTFs was examined with an immersion time of 10 min. Based on the above results, the F-CNTFs were immersed into a CSA solution and treated by a progressive stretching treatment. The following three fibers were prepared based on the different stretching rates (6, 4, and 3% min^{-1}) under 5 stretching processes: CSA-6% min^{-1}-CNTFs, CSA-4% min^{-1}-CNTFs, and CSA-3% min^{-1}-CNTFs. Then the fibers termed CSA-CNTFs were introduced into the acetone (Aladdin, 99%) bath for densification.

Preparation of PBO-CNTFs

The poly(*p*-phenylene-2,6-benzobisoxazole) (PBO) fibers were infused into the CSA solution with a weight of 0.025, 0.05, and 0.1 wt%, respectively, which were provided by China Bluestar Chengrand Research Institute of Chemical Industry (http://www.lxcgy.chemchina.com/zlcgen/28882.html). The molecular weight and viscosity of PBO were measured as 69,322 g mol^{-1} and 1.37 dL g^{-1}, respectively. The mixed solutions were magnetically stirred for 3 h at room temperature, forming the yellow PBOs dispersions. Then the F-CNTFs were introduced into the uniform PBOs-CSA baths and treated by the aforementioned progressive stretching treatment, and these obtained fibers were denoted as PBO-CNTFs.

Preparation of D-PBO-CNTFs

The mechanical densification treatment (MSK-2150, SHENZHEN KEJINGSTAR technology company, Ltd., China) was developed to further improve the packing density for the preparation of D-PBO-CNTFs. First, the PBO-CNTFs were sandwiched between two aluminum foils. Then

the two rollers were adjusted until there was no visible gap between them, and the running rollers were used to roll the samples. Finally, the D-PBO-CNTFs were produced.

Linear density tests of fibers by the weighing method

The linear density of fibers was measured by the weighing method, which was calculated by

$$D = W/L, \tag{1}$$

where D (tex), W (g), and L (km) are the linear density, weight, and length of the fibers, respectively. The measured linear densities, densities, specific strength, and specific modulus were summarized in table S10.

Wide angle x-ray scattering (WAXS) and small angle x-ray scattering (SAXS) measurements

WAXS and SAXS measurements were conducted on a SAXS/WAXS system (Xenocs, Xeuss 3.0) using an incident Cu-Kα x-ray beam perpendicular to the fiber axis. The sample-to-detector distances during WAXS and SAXS measurements were 60 and 900 mm, respectively. The analysis of WAXS patterns was performed by FIT 2D software. The orientation of CNTs was quantified by Herman's orientation factor (f) (*41*), which was defined as follows,

$$f = \frac{3\cos^2\varphi - 1}{2}, \tag{2}$$

where φ is the angle between the fiber axis and the crystal plane, and $\cos^2\varphi$ is the average value of the square of the cosine of the azimuthal angle of CNTFs, which is calculated as follows,

$$\cos^2\varphi = \frac{\int_0^{\pi/2} I(\varphi)\cos^2\varphi\sin\varphi \mathrm{d}\varphi}{\int_0^{\pi/2} I(\varphi)\sin\varphi \mathrm{d}\varphi}, \tag{3}$$

where $I(\varphi)$ is the intensity at an azimuthal angle of φ.

The resulting analysis of SAXS patterns was performed by FIT 2D software and xPolar software. SAXS can be used to evaluate the difference in electron density between different phases and thus to analyze the internal structure of fibers. Here the analysis was focused on the fiber streak, and fig. S21B shows plots of the fiber streak intensity for different fibers as a function of the scattering vector q (defined as $4\pi \sin\theta/\lambda$) (*32*).

Orientational order parameters (s) from polarized Raman spectra

To further demonstrate the evolution of orientation of modified CNTFs, the polarized Raman spectra of G bands were performed (fig. S20). The orientational order parameter (s) was calculated from the polarized resonant Raman spectroscopy (532 nm excitation) by measuring the G peak intensity I from three different scattering geometries (I_{VV}, I_{VH}, and I_{HH}) by the following equation (*42*):

$$s = \frac{3I_{VV} + 3I_{VH} - 4I_{HH}}{3I_{VV} + 12I_{VH} + 8I_{HH}}. \tag{4}$$

Half-wave plates were used to rotate the incident and/or scattered polarity. The values of s for F-CNTFs, CSA-CNTFs, PBO-CNTFs, and D-PBO-CNTFs are 0.46 ± 0.2, 0.78 ± 0.1, 0.85 ± 0.3, and 0.82 ± 0.2, respectively, which were evaluated at least 6 places on each fiber.

Quasi-static mechanical properties

Quasi-static mechanical properties of different fibers were performed by a universal testing machine (Shimadzu, EZ-LX with a 5 N load cell) with a loading rate of 1 mm min^{-1}. The fiber

samples for the tensile tests were attached to a paper frame using epoxy glue, and the gauge length was 10 mm. Before the quasi-static tensile testing, the cross-sectional areas of CNTFs were obtained using ImageJ software from cross-sectional scanning electron microscopy (SEM, FEI Quattro S, Thermo Fisher Scientific, acceleration voltage 5-10 kV) images. The samples were sandwiched between the two clamps, and released by cutting the legs of the paper frame. Then the uniaxial tension was exerted on the samples and the stress-strain curves were recorded. After the measurements, mathematic analysis of Young's modulus and toughness was obtained. The modulus was equal to the slope of curves at 0.1-0.5% strain, and the toughness was calculated by integrating the area of the stress-strain curves. The average mechanical properties (tensile strength, Young's modulus, elongation at break, and toughness) and their corresponding standard deviations were calculated based on the 4-5 measurement results. It is worth noting that the few samples that broke near the clamps were excluded from the calculations.

Stress relaxation measurements

The stress relaxation experiments were carried out by stretching the fibers to 1.5% strain at a loading rate of 1 mm min^{-1} using a mechanical testing machine (Shimadzu, AGS-X, 5 N load cell). Then the dependence of stress on time was recorded while the strain was maintained.

Dynamic mechanical properties

The dynamic mechanical properties of single fibers under high strain rates were measured by a developed mini-split Hopkinson tension bar (mini-SHTB) (fig. S25). The fibers were glued to the paper frame with a gauge length of 5 mm and then fixed onto the mini-SHTB. Similarly, before the testing, the legs of the paper frame were cut carefully to release the single fiber. A gas gun was used to launch the sleeve-typed projectile on the energy-absorbing bar fixed at the end of the incident bar to generate a tensile stress wave simultaneously. It propagated along the incident bar and arrived at the samples, resulting in the fracture of fibers under the dynamic tension. A high-frequency quartz piezoelectric force sensor (Kistler 9001, 180 kHz) was used to measure the rupture force of the fiber. The loading end of the incident bar could be regarded as a free boundary condition compared with the fibers due to the sufficient high impact impedance of the incident bar. As a result, the strain rate $\dot{\varepsilon}(t)$, strain $\varepsilon(t)$, and stress $\sigma(t)$ of a single fiber at different time can be analyzed,

$$\dot{\varepsilon}(t) = 2C_0 \frac{\varepsilon_I}{l_s}, \tag{5}$$

$$\varepsilon(t) = 2C_0 \int_0^t \frac{\varepsilon_I}{l_s} \mathrm{dt}, \tag{6}$$

$$\sigma(t) = \frac{F}{A_s}, \tag{7}$$

where C_0, l_s, and A_s are elastic wave velocity of the incident bar, length, and cross section area of fibers, respectively. ε_I and F are strain in the incident bar and force of fibers, respectively.

The measured strain as given by Eq. (6) is contributed by the axial elongation of fibers and the relative sliding between the specimens and fixture. Therefore, the actual strain of a single fiber needs a calibration (*34*), which can be determined according to the linear relationship between $\Delta l/F$ and l_s/A_s, where Δl is the displacement of fibers measured directly by the mini-SHTB. The PBO fiber samples with gauge lengths of 5 mm, 6 mm, and 8 mm were prepared and tested at a high strain rate as shown in fig. S26. The value of system compliance, C_S, is determined as the

intercept 0.0015 mm N^{-1} for the zero-gauge length. As a result, the actual strain of a single fiber is obtained as

$$\varepsilon_{\text{Corrected}} = \frac{\Delta l - C_S F}{l_0}. \tag{8}$$

The typical incident stress wave and force signals of a single fiber are shown in fig. S27A and the corresponding engineering stress-strain curves are shown in fig. S27B. The constant strain rate condition is obtained when the strain is larger than 1%, validating the experimental measurements of dynamic mechanical properties of single fibers. Figure 3D shows the typical engineering stress-strain curves of F-CNTFs, CSA-CNTFs, PBO-CNTFs, and D-PBO-CNTFs at the strain rate of about 1400 s^{-1}, from which the fracture toughness of fibers is the area of the region enclosed by the stress-strain curve and coordinate axis.

Laser-induced high-velocity transverse impact testing

Xie et al. (*2*) proposed a measurement, "SEDP", to evaluate the specific energy dissipation power of fibers under ultrahigh strain rate (USR) tests. The results show that SEDP of fibers increases linearly with increasing the transverse wave velocity, c_T, under their experimental conditions for four types of fibers.

In Xie's article (*2*), it is unknown why SEDP = 7.5×10^{10} kg^{-1} c_T in the impact velocity of about 500 m s^{-1} and whether the linear relationship between SEDP and c_T is applied to other fibers under a wide range of impact conditions. According to their work (*2*), the SEDP is defined as the maximum slope of E^*, which can be calculated as

$$\text{SEDP} = \max \frac{\mathrm{d}\left[E^*(t)\right]}{\mathrm{d}t}, \tag{9}$$

$$E^*(t) \equiv \frac{E_k(0) - E_k(t)}{E_k(0)\lambda}, \tag{10}$$

where λ is the linear mass density of the fiber, $E_k(0)$ and $E_k(t)$ are the initial kinetic energy and the kinetic energy at time t of the probe-particle, respectively.

To unveil the underlying mechanism between SEDP and c_T, the kinetic energy and strain energy of a fiber under the high-velocity transverse impact are analyzed. During the transverse impact, the kinetic energy of a probe-particle is converted into the strain energy (W_S) and the kinetic energy (W_K) of the fiber,

$$W_S = A c_L t \int_0^{\varepsilon_{ins}} \sigma(\varepsilon)\mathrm{d}\varepsilon, \tag{11}$$

$$W_K = \frac{1}{2}\left(\frac{c_T t}{\cos\gamma}\lambda\right) v^2(t), \tag{12}$$

where A is the cross section of fiber, ε_{ins} is the instantaneous strain, $\sigma(\varepsilon)$ is the stress, and γ is the deflection angle (fig. S29).

According to the conservation of energy, after a time interval (Δt),

$$\text{SEDP} = \frac{\Delta E^*}{\Delta t} = \frac{1}{E_k(0)} \frac{2\left[A c_L \Delta t \int_0^{\varepsilon_{ins}} \sigma(\varepsilon)\mathrm{d}\varepsilon + \frac{1}{2}\left(\frac{c_T \Delta t}{\cos\gamma}\lambda\right) v^2(t)\right]}{\lambda \Delta t}. \tag{13}$$

Assuming that the fiber is in the linear elastic deformation stage,

$$\mathrm{SEDP}=\frac{1}{E_k(0)}\frac{2\left[\frac{1}{2}Ac_{\mathrm{L}}E\varepsilon_{\mathrm{ins}}^2+\frac{1}{2}\left(\frac{c_{\mathrm{T}}}{\cos\gamma}\lambda\right)v^2(t)\right]}{\lambda}=\frac{1}{E_k(0)}\frac{Ac_{\mathrm{L}}E\varepsilon_{\mathrm{ins}}^2+\left(\frac{c_{\mathrm{T}}}{\cos\gamma}\lambda\right)v^2(t)}{\lambda}, \tag{14}$$

Eq. (14) is rewritten as

$$\mathrm{SEDP}=\frac{1}{E_k(0)}\left[{c_{\mathrm{L}}}^3\varepsilon_{\mathrm{ins}}^2+\frac{c_{\mathrm{T}}}{\cos\gamma}v^2(t)\right]. \tag{15}$$

For the transverse impact of the fiber, the relationship among the c_{T}, c_{L}, and v_0 is (*43*)

$$c_{\mathrm{T}}=(\frac{c_{\mathrm{L}}}{2})^{\frac{1}{3}}v_0^{\frac{2}{3}}. \tag{16}$$

Substituting Eq. (16) into Eq. (15),

$$\mathrm{SEDP}=\frac{1}{E_k(0)}\left[\frac{8c_{\mathrm{T}}^8\varepsilon_{\mathrm{ins}}^2}{v_0^6}+\frac{v^2(t)}{\cos\gamma}\right]c_{\mathrm{T}}. \tag{17}$$

The relationship among c_{L}, v_0, and $\varepsilon_{\mathrm{ins}}$ is (*44*)

$$v_0=c_{\mathrm{L}}\sqrt{\varepsilon_{\mathrm{ins}}\left[2\sqrt{\varepsilon_{\mathrm{ins}}\left(1+\varepsilon_{\mathrm{ins}}\right)}-\varepsilon_{\mathrm{ins}}\right]}. \tag{18}$$

Since Xie et al. (*2*) used an ultrahigh-speed camera to capture the movement of the probe-particle, the time interval is very small and therefore we neglect the decay of the speed of the probe-particle at the initial impact process,

$$v(t)=v_0. \tag{19}$$

As a result, Eq. (17) can be rewritten as

$$\mathrm{SEDP}=\frac{1}{E_k(0)}\left[\frac{8c_{\mathrm{T}}^8\varepsilon_{\mathrm{ins}}^2}{v_0^6}+\frac{v_0^2}{\cos\gamma}\right]c_{\mathrm{T}}=\xi c_{\mathrm{T}}, \tag{20}$$

$$\xi=\frac{1}{E_k(0)}\left[\frac{8c_{\mathrm{T}}^8\varepsilon_{\mathrm{ins}}^2}{v_0^6}+\frac{v_0^2}{\cos\gamma}\right]. \tag{21}$$

Taking γ and c_{T} from the study of Xie et al. (*2*), the values of ξ for various fibers are calculated as listed in table S15 according to Eq. (21), which are very close to 7.5×10^{10} kg^{-1}. Therefore, the underlying mechanism of SEDP and c_{T} for four types of fibers is obtained.

Based on Eq. (17) and Eq. (19), the indicator SEDP can be written as

$$\mathrm{SEDP}=\frac{1}{E_k(0)}\left[\frac{8c_{\mathrm{T}}^8\varepsilon_{\mathrm{ins}}^2}{v_0^6}+\frac{v_0^2}{\cos\gamma}\right]c_{\mathrm{T}}. \tag{22}$$

The relationship among c_{L}, v_0, and γ is taken as (*45*)

$$\gamma\approx\tan^{-1}(\frac{2v_0}{c_{\mathrm{L}}})^{\frac{1}{3}}. \tag{23}$$

Substituting Eq. (23) into Eq. (22),

$$\mathrm{SEDP}=\frac{1}{E_k(0)}\left\{\frac{8c_{\mathrm{T}}^8\varepsilon_{\mathrm{ins}}^2}{v_0^6}+\frac{v_0^2}{\cos\left[\tan^{-1}(\frac{2v_0}{c_{\mathrm{L}}})^{\frac{1}{3}}\right]}\right\}c_{\mathrm{T}}. \tag{24}$$

Eq. (18) can be rewritten as

$$v_0^4 = c_L^4 \varepsilon_{ins}^2 \left[4\varepsilon_{ins} + 5\varepsilon_{ins}^2 - 4\varepsilon_{ins}\sqrt{\varepsilon_{ins}(1+\varepsilon_{ins})} \right]. \quad (25)$$

Since ε_{ins} is a generally tiny value between 0 and 0.1 under a transverse impact, Eq. (25) can be simplified as

$$v_0^4 \approx 4 c_L^4 \varepsilon_{ins}^3. \quad (26)$$

As a result, Eq. (24) can be simplified as

$$\mathrm{SEDP} = \frac{1}{E_k(0)} \left[\frac{v_0^2}{2} + \frac{v_0^2}{\cos\left[\tan^{-1}\left(\frac{2v_0}{c_L}\right)^{\frac{1}{3}} \right]} \right] c_T = \frac{1}{E_k(0)} \zeta c_T, \quad (27)$$

$$\zeta = \frac{v_0^2}{2} + \frac{v_0^2}{\cos\left[\tan^{-1}\left(\frac{2v_0}{c_L}\right)^{\frac{1}{3}} \right]}. \quad (28)$$

For different initial velocities of probe-particle, the relationship between c_L and ζ in Eq. (28) is illustrated in fig. S30. As c_L of high-performance fibers such as aramid fibers (*46*), carbon fibers (*47*), M5 fibers (*48*), ultrahigh molecular weight polyethylene (UHMWPE) fibers (*49*), PBO fibers (*50*), CNTFs (*51*), and Kevlar 129 fibers (*52*) are generally larger than 7000 m s^{-1}, ζ is almost a constant value for a given v_0. As a result, the SEDP of high-performance fibers can be determined by measuring c_T at a given impact velocity v_0.

Based on the above discussion, the SEDP can be determined by directly measuring c_T as long as the impact velocity is ensured to be approximately constant, e.g., large-mass particle impact, in which condition we do not need to capture accurately the velocity history of the projectile. In view of this, we develop an effective experimental method to obtain the SEDP of fibers under high-velocity transverse impact, which is similar to advanced laser-induced micro-projectile impact testing (α-LIPIT) as shown in fig. S31. After the laser ablation of the 100-nm-thick gold film, a polydimethylsiloxane (PDMS) layer with 76-μm-thick was rapidly expanded, causing the swelling PDMS film, i.e., the conical-shaped projectile, to impact the fiber specimen at a high speed. The high-speed camera (KIRANA UHS Camera) with an imaging velocity of 5×10^6 fps and the SI-LUX640 automatic laser lighting system were used to capture the impact process. The SEDP of the fiber can therefore be determined through image measurements of the rigid velocity of the conical-shaped projectile and c_T of the fiber. It can be seen that the efficiency of the new experimental method is improved compared to the experimental method of Xie et al. (*2*).

Therefore, the SEDP of these fibers is obtained by measuring c_T under the supersonic transverse impact by a high-speed imaging system. The initial two frames and the last two frames were used to calculate the impact velocities and c_T of a single fiber, respectively (fig. S32). The impact velocity in our work was about 500 m s^{-1}. The measured SEDP of nylon fibers is consistent with the previous study (*2*), providing a validation of our experimental method.

Numerical Modeling

We used ABAQUS to simulate the performance of a single fiber under the transverse impact. The conic PDMS film induced by the laser was modeled as a rigid body. The single fiber was modeled as a three-dimensional continuum. Due to the symmetry of the numerical model, the 1/4 model with 626,400 elements was built to simplify the computation. The fiber was fine-meshed

with 232 elements in the cross section and 2,700 elements along the length. The transversely isotropic linear elastic constitutive model was chosen to describe the mechanical behavior of the fiber. The quasi-static elastic modulus was used, and other parameters, such as the shear modulus and Poisson's ratio, were obtained from the study of Xie et al. (*2*). The simulated details are listed in table S16. The simulation results manifest that the bending stiffness of fibers has a noticeable impact on the SEDP, which is determined by the cross-sectional morphology and impact direction (fig. S33 and table S13). Notably, the higher bending stiffness leads to a smaller deflection angle (Fig. 3H), resulting in a higher c_T. Interestingly, the finite element simulation results of CSA-CNTFs and PBO-CNTFs indicate that more volume of fiber participates in the consumption of impact energy because of the increase in c_L after the infusion of PBOs (fig. S34, A and B).

Deformation of the fiber after an impact

Figure S35 demonstrates the deformation of the fiber after an impact of 400 ns. Figure S36 shows the history of displacement, velocity, and acceleration of the conic PDMS film. We can evaluate the force applied on the fibers by the product of mass and acceleration of the conic PDMS film. The compression of the fibers at the moment of impact makes the acceleration of conic PDMS film reach the peak value (2.88×10^8 m s^{-2}), and the calculated force is about 2.44 N, which is higher than that in Xie's article (70 mN) due to the fact that in our work the fiber has a larger cross-sectional area (4.84 times) and a heavier impactor (265 times). In order to accurately obtain the force on the fibers in a transverse impact, we will also use sensors to monitor in the future.

All-atom molecular dynamics simulations

All-atom molecular dynamics (MD) simulations were performed using large-scale atomic/molecular massively parallel simulator (LAMMPS) computational package (*53*). The polymer consistent force field (PCFF) was employed to describe the interatomic potentials (*54*). The long-range Columbia interaction was included using particle-particle-particle mesh (PPPM) method (*55*), while the van der Waals interaction was described by the 6/9 Lennard-Jones potential $\varepsilon[2(\sigma/r)^9\text{-}3(\sigma/r)^6]$ with a cutoff distance of 1.0 nm. To integrate the Newton equations of motion, the Verlet algorithm was adopted with a time step of 0.5 fs. Prior to initiating the tensile deformation protocol, the constructed structures underwent energy minimization using a conjugate gradient algorithm. The mechanical responses to tensile loads of these structures were then investigated at nearly zero K using a Nosé-Hoover thermostat.

To investigate the effect of PBOs on the mechanical resistance of functionalized CNTs, we constructed models consisting of two CNTs with a length of 16 nm and a radius of 0.67 nm. Randomly distributed hydroxy groups were used to functionalize two CNTs, and the edges of tubes were terminated by hydrogen atoms. The chemical composition of CNT was n_C:n_O:n_H = 1:0.08:0.10, which was from experimental evidence. PBO chains were wrapped around CNTs. The interlayer distance between CNTs was 0.85 nm, consistent with that between graphene oxide (GO) sheets characterized in experiments (*56*). A non-periodic boundary condition was applied. To apply pull-out loads on the system, we fixed the left end of the bottom CNT and displaced the right end of the top CNT at a constant velocity of 10 m s^{-1} along the axial direction (fig. S41, A and B).

To calculate the interfacial energy between PBO chains and CNTs, a single PBO chain was placed onto a functionalized sp^2 carbon sheet to acquire the binding energy. In-plane periodic boundary conditions were used, and the vacuum layer with a thickness over 6 nm was adopted along the out-of-plane direction. The binding energy can be calculated by the sum of the energies of the individual PBO chain and the isolated functionalized sp^2 carbon sheet minus the total energy

of the composite system. Then the energy was divided by the total number of atoms (except for hydrogen atoms) to obtain the normalized binding energy.

Coarse-grained model and simulations

To explore the structural evolution and mechanical behaviors of fibers, we employed mesoscale coarse-grained molecular dynamics (CGMD) simulations. The CNT and PBO were modeled as coarse-grained bead-spring chains with bond interactions (fig. S40B). The angle interactions were adopted among three successive beads to capture the bending behaviors. Within each chain, the stretching contribution between bonding beads with distance R to the total energy was given by $E_T = K_T(R-R_0)^2$, where $K_T = YA/R_0$ was the spring constant that is related to the Young's modulus (Y), the cross section area (A), and the equilibrium distance (R_0). In our model, the equilibrium bond lengths were adopted as 3 nm and 1.5 nm for CNT and PBO chains, respectively. The bending energy contribution within adjacent beads triplets was described as $E_B = K_B(1+\cos\theta)$, where $K_B = 2YI/R_0$ was the angular spring constant, where I and $D = YI$ are the bending moment of inertia and bending stiffness of chains, and θ is the bending angle within adjacent beads triplets. D was calculated by fitting bending stiffness with all-atom MD simulations. The van der Waals interactions between beads of CNTs and PBOs were described by the 12-6 Lennard-Jones formula $4\varepsilon[(\sigma/R)^{12}-(\sigma/R)^6]$. These parameters are summarized in table S17. Notably, the lengths of the CNT and PBO chains in experiments were on the order of tens of microns, whereas the simulated chains were on the order of hundreds of nanometers. To address this discrepancy, the van der Waals parameter ε was increased to capture the essential interfacial interactions of chains, which can be seen as an increase in the interacted length of chains according to shear-lag theory (*57*).

To investigate the enhancement effect of PBO nanofibers on the mechanical behaviors of CNT bundles, the models consisting of CNT bundles and PBO nanofibers were constructed. First, the PBO nanofibers were placed onto the surface of CNT bundles, and the structural equilibrium demonstrates that PBO nanofibers would also preferentially adsorb on the surface of CNT bundles by undergoing self-induced bending (fig. S40C). Subsequently, pull-out tests were conducted on coarse-grained CSA-CNTs with and without the addition of PBO nanofibers. The pull-out loads were applied on one of the CNTs at the surface by displacing the end of the CNT at a constant velocity of 10 m s^{-1} along the axial direction (fig. S41, C and D). The discrepancy observed in the pull-out force suggests that the addition of PBO nanofibers would result in an enhancement in the interfacial interactions due to an increased effective contact area.

To investigate the mechanical behavior of fibers, the periodic boundary conditions were adopted along all three directions. CNTs with a contour length of 600 nm were constructed with an initial curvature considering the thermal fluctuations. For PBO-CNTFs, about 8 wt% PBOs with a contour length of 300 nm were added and distributed randomly. The chains were deposited in a layer-by-layer manner. The Langevin equations of motion were integrated to equilibrate the microstructure of fibers. After structural equilibrium, progressive loading was conducted along the x direction until the density approached that in experiments. The structures were further equilibrated and then deformed in the axial direction, where the simulation box consisted of CNT and PBO fibers with dimensions of 748 nm × 86 nm × 12 nm. During the tensile process, the failure strains were set to 5% and 10% for CNT and PBO, respectively (*58*). To explore the loading velocity effects, the velocities were adopted as 10 m s^{-1} and 1000 m s^{-1}, respectively. The equations of motion were integrated using a velocity Verlet algorithm with a time step of 10 fs that can ensure the numerical convergence of integration. The pressure in the y and z directions was controlled as 1 atmosphere during the uniaxial tensile loading process by using a Berendsen barostat.

To calculate the percentage of broken CNTs within the fibers under various strains, we tracked the inter-bead strain in each CNT in the coarse-grained simulations. When the inter-bead strain in a CNT exceeds the failure threshold, the CNT is considered to be broken. The percentage of broken CNTs was calculated through dividing the number of broken CNTs by the total number of CNTs within a cross-sectional unit.

Alignment of CNTs in simulations

Herein, we defined an orientation order parameter (o) to quantify the alignment of each CNT in simulations (*59*), which can be written as

$$o = 2\cos^2\theta - 1, \tag{29}$$

where θ is the angle between CNTs and x axis. The orientation order parameter of each CNT was calculated and averaged to obtain the alignment of structures.

Persistence length of PBO and CNT

Polymers will behave like a rigid rod at room temperature T for lengths shorter than the persistence length ($l_p = D/kT$, where D and k are the bending stiffness and Boltzmann constant, respectively). For materials such as CNTs, the bending stiffness can be obtained from $D = YI$. In our calculations, the value of D is about 5×10^5 eV Å, corresponding to the l_p of 1.9×10^6 nm (*39*). The length of CNTs in experiments is tens of microns, far lower than their persistence length. As for PBO chains, the bending stiffness is calculated from the energy (E_b) required to bend an arbitrarily long segment into a circle with a radius R ($D = E_bR/\pi$) (*60*). With this method, D and l_p are calculated as 9.84 eV Å and 38 nm, respectively, consistent with the previous report (*40*). In experiments, PBO with a length of about 10 μm was used, far larger than their persistence length. These results indicate that PBO chains are much more flexible than CNTs.

Other characterizations

The SEM images of morphology and microstructure of different fibers were examined by the FEI Quattro S with acceleration voltages of 5-10 kV. The radial and axial cross sections of fibers were cut by a focused ion beam (FIB) using a ZEISS Crossbeam 550. The cross-sectional areas of CNTFs were obtained using ImageJ software from cross-sectional SEM images cut by FIB (*27*). The transmission electron microscopy (TEM) images of CNTs, PBOs, and fibers were obtained with the FEI Tecnai F20 at an acceleration voltage of 200 kV. Raman spectra of fibers were performed with a Horiba LabRAM HR 800 (532 nm laser wavelength). All G bands in the Raman spectra of CNTFs under different applied strains were fitted with Lorentzian functions to obtain the peak positions. X-ray photoelectron spectroscopy (XPS) spectra were measured by a Kratos Analytical Axis-Ultra spectrometer with an Al Kα x-ray source. Fourier transform infrared (FTIR) spectra were obtained using a Thermo Nicolet Nexus-470 FTIR instrument in the attenuated total reflection mode. The PBO weight ratios of different fibers were investigated by elemental analyses (vario EL cube). The purification efficiency of fibers was measured by thermogravimetric analyses with a temperature scan rate of 10 °C min^{-1} under an air atmosphere using a Netzsh STA 449 F5. The PBOs contents in fibers were measured by thermogravimetric analyses under a nitrogen atmosphere. The weight fraction of PBOs (w_1) in CNTFs was calculated from the weight loss curve over the temperature range from 0 to 600 °C and was approximately given by

$$w_1 = \frac{M_{\text{PBO-CNTF}} - M_{\text{CSA-CNTF}}}{M_{\text{PBOs}} - M_{\text{CSA-CNTF}}}, \tag{30}$$

where $M_{PBO\text{-}CNTFs}$, $M_{CSA\text{-}CNTFs}$, and M_{PBOs} (about 44%) are the fraction of weight loss from 0 to 600 ℃ for PBO-CNTFs, CSA-CNTFs, and PBOs, respectively.

The electrical conductivity of fibers was measured with a homemade 4-point probe. Nanoscale x-ray computed tomography (nano-CT) was examined by a 50-nm-resolution ZEISS Xradia 810 Ultra with a 5.4 keV Cu-Kα x-ray source under the high-resolution mode. It should be noted here that the porosities with sizes less than the resolution of the nano-CT (50 nm) may not be accurately counted, potentially resulting in an underestimation of the porosities within the fibers. The molecular weight and viscosity of PBOs were measured by gel permeation chromatography (1260 Infinity II GPC/SEC) with columns in series (PL1110-6504) and ubbelohde viscometer, respectively.

Supplementary Text

Effect of weak oxidation and acid washing processes on the structure, morphology, and mechanical properties of CNTFs

The weak oxidation by hydrogen peroxide and subsequent hydrochloric acid washing treatments were applied to prepare F-CNTFs. The introduction of surface functional groups and the influence of fiber structures and morphology were measured by thermogravimetric analyses, XPS, Raman spectra, and SEM. Thermogravimetric analyses demonstrate the impurities, especially iron-based catalysts, have been effectively removed, and the residual mass is only 6.1 wt% as the oxidation time is 24 h (fig. S4). According to the Raman spectra of fibers, the G band (about 1590 cm^{-1}) arises from the sp^2-hybridized carbon network, and D band (about 1340 cm^{-1}) corresponds to the disordered carbon bonds or defects (sp^3 hybridization, kinks, or Stone-Wales defects). The intensity ratio of G band to D band (I_G/I_D) is used to evaluate the defect densities of fibers. The I_G/I_D ratios of F-CNTFs decrease from 4.7 to 2.6 after the oxidation process (fig. S5 and table S1), indicating that the treatment can introduce defects into the nanotube structures. Based on the XPS results, the C 1s peak can be fitted by four peaks at 284.6 (C-C), 285.2 (C-OH), 286.8 (-C=O), and 289.2 eV (-COOH). Moreover, with increasing the oxidation time, the C/O ratios decrease from 26.7 to 4.8, and more hydroxy groups are introduced into the fibers (fig. S6 and table S1). The diameter of the F-CNTFs (24 h) decreases from 41.7 ± 1.3 μm (pristine CNTFs) to 36.2 ± 0.6 μm (fig. S7). Furthermore, the increase in the size of CNT bundles after the purification process, as depicted in fig. S7D, provides evidence that the removal of impurity can promote the van der Waals interactions between individual CNTs, resulting in a decrease in the distance between adjacent CNTs. Because of the volume shrinkage after the removal of the internal impurities, a strong condensation of CNTs inward manifested as a rough surface morphology. Thus, the purification process endows the fibers with a more compact structure and a reduction of the CNTFs' diameter because the removal of impurities yields better interactions between CNTs, leading to an improvement in the mechanical properties. Particularly, the tensile strength of CNTFs increases from 1.1 GPa to 1.8 GPa when the oxidation time is 12 h (fig. S8 and table S1), indicating the improvement of fiber strength due to the purification treatment.

Optimization of the CSA densification process

When the F-CNTFs are immersed in CSA solution, fibers will swell obviously because of the side-wall protonation by CSA (fig. S9). Appropriate immersion time and stretching ratio of F-CNTFs can rearrange the tangled CNTs to improve their alignment and densification, and thereby enhance the mechanical properties of fibers. First, we examined the effect of immersion time in CSA on the mechanical properties. The tensile strength of F-CNTFs improves distinctly as the immersion time increases from 5 to 10 min, but then decreases as the treatment time further increases (fig. S10). Then the effect of stretching ratios on the tensile strength was explored. With increasing the stretching ratios from 5% to 20%, the tensile strength of fibers monotonically increases (fig. S11), and then decreases as the stretching ratio is higher than 20%. Therefore, the appropriate immersion time and stretching ratio are 10 min and 20%, respectively.

Effect of the progressive stretching treatment on the structure and mechanical properties of F-CNTFs

We developed a progressive stretching treatment with different stretching rates under 5 processes (fig. S12, A to C). Based on the above results, the immersion time and stretching ratio of F-CNTFs in a CSA bath were fixed at 10 min and 20%, respectively. As the stretching rates

decrease from 6% min^{-1} to 3% min^{-1}, F-CNTFs show more aligned and denser structures (fig. S12, D to F), which is consistent with the simulation results that the fibers can reorganize entangled CNTs to a more uniform, compact and ordered architecture due to the reorganization of microstructures, including curving, reorientation, straightening and sliding of the internal nanotubes and bundles during the progressive stretching treatment (fig. S42). The SEM and TEM images of the axial cross section of F-CNTFs obtained by the progressive stretching treatment with a stretching rate of 3% min^{-1} demonstrate a highly aligned and dense microstructure (fig. S12G). The alignment degree (Herman's orientation factor, *f*) of CSA-CNTFs under different stretching rates was characterized using WAXS patterns (fig. S13). The CSA-6% min^{-1}-CNTFs have a full width at half maximum (FWHM) of 14.1° and *f* of 0.81, while the CSA-3% min^{-1}-CNTFs have a lower FWHM and higher *f* (FWHM of 12.3° and *f* of 0.90) (table S4), suggesting that the progressive stretching treatment at a low stretching rate provides adequate time for the sufficient disentanglement and more efficient reorientation of CNTs, thereby resulting in the more dense, ordered, and uniform structures. Thus, the well-organized architecture contributes to the improvement in tensile strength of 4.5 ± 0.2 GPa, Young's modulus of 130.8 ± 7.5 GPa, and toughness of 111.1 ± 7.1 MJ m^{-3} (fig. S14 and table S5).

Infiltration mechanism of PBOs

PBO fibers can be dissolved into nanofibers and molecular chains (PBOs) in CSA solution (fig. S15), which results from the interchain repulsions. When CNTFs are immersed in a CSA bath, the size of CNTFs swells remarkably because of the side-wall protonation effect (fig. S9). This offers plenty of room to infuse PBOs. During the immersion of PBOs into the fibers, PBOs can maintain the forms of nanofibers and molecular chains. Finally, the CSA is washed in an acetone bath for densification, and the interchain repulsions are largely eliminated. As a result, the PBOs are expected to adsorb on CNT surfaces (fig. S39), which is determined by a complex spatial-temporal evolution of CNTs and PBOs. Our atomistic simulations indicated that the PBOs have strong interfacial interactions with CNTs (binding energies of 71.2 meV per atom, 55.5 meV per atom, and 31.5 meV per atom for PBO/CNT, CNT/CNT, and PBO/PBO, respectively), suggesting that PBOs are more likely adsorbed on CNTs compared to the aggregation of individual PBOs.

Fracture behavior of fibers at different strain rates

As shown in fig. S24, F-CNTFs and CSA-CNTFs show similar fracture behavior under the quasi-static testing, where CNTs slip between each other and single nanotubes or small bundles are pulled out. By contrast, after the progressive stretching and densification treatments, the fracture morphology of PBO-CNTFs and D-PBO-CNTFs show an approximatively brittle fracture structure with larger bundles, because the strong interactions between PBOs and CNTs can prevent the bundles from slipping between each other (fig. S24, C and D) and lead to the effective redistribution of local stress. What's more, after the dynamic mechanical test of different fibers under high strain rate loadings (about 1400 s^{-1}), the interface sliding mode is observed for F-CNTFs and CSA-CNTFs without PBOs, in which abundant CNT bundles on the periphery are pulled out due to the weak van der Waals interactions between CNTs (fig. S28, A and B). In contrast, a pretty smooth profile forms for the PBO-CNTFs and D-PBO-CNTFs due to the PBOs between the adjacent CNTs strongly restricting the slippage behavior of bundles (fig. S28, C and D). The interesting translation of fracture modes from the interface sliding to the crosslink-restricted deformation indicates the change of energy dissipation mechanisms, which results in the dramatic improvement of dynamic strength.

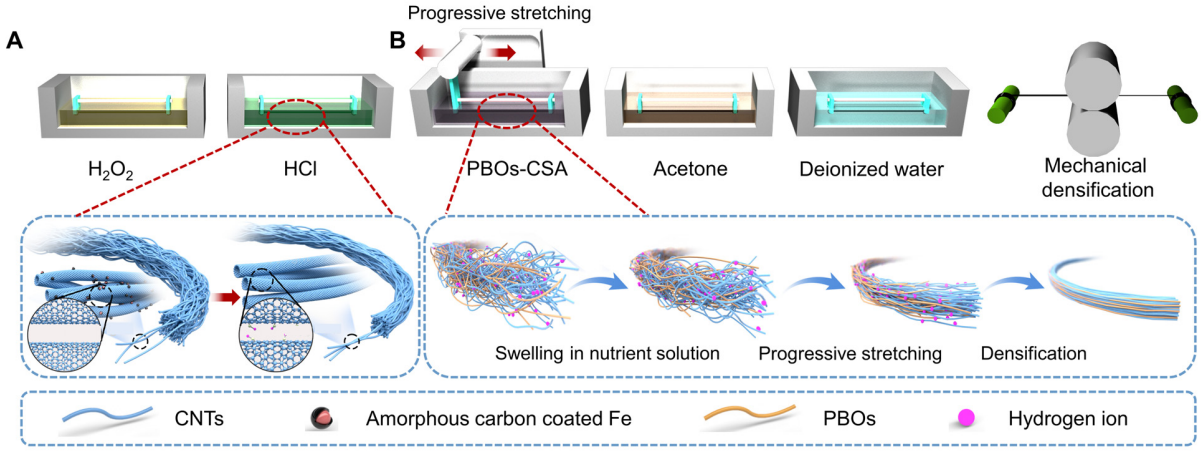

Fig. S1. Schematic diagram for fabricating highly packed and aligned fibers.

(**A**) Schematic diagram of functionalization and purification of pristine carbon nanotube fibers (CNTFs). (**B**) Schematic diagram of the progressive stretching and densification treatment for the highly packed and aligned fibers.

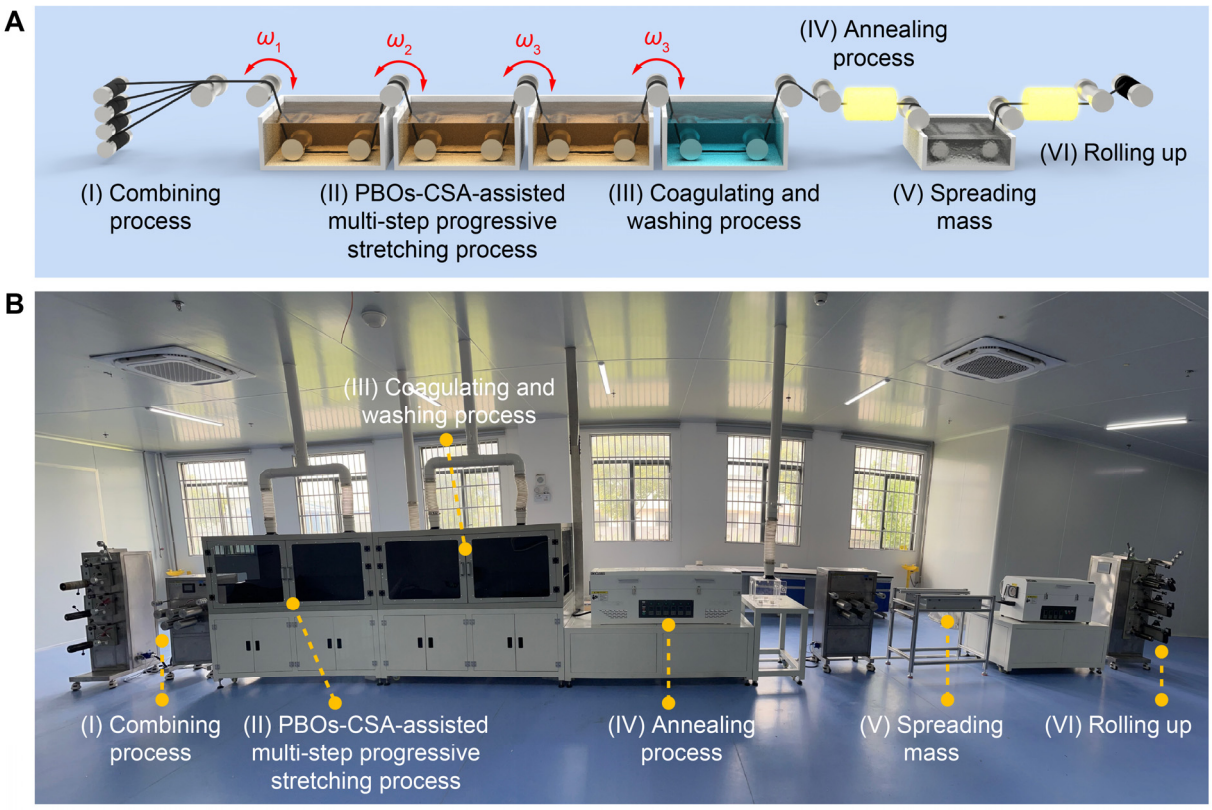

Fig. S2. Continuous multi-step progressive stretching process for preparing high-performance tows.

(**A**) Schematic diagram of continuous production of PBO-CNT tows. (**B**) Photograph of the corresponding equipment. The continuous treatment process consists of combining monofilaments, PBOs-CSA-assisted multi-step progressive stretching, coagulating and washing, annealing, sizing, and rolling up processes. The multi-step progressive stretching process is achieved by regulating the angular velocity (ω) and direction of different rollers. In the first step, the angular velocities of different rollers were regulated as $\omega_1 < \omega_2 < \omega_3$, and the tows were stretched to a certain strain. In the second step, the direction of rollers was reversed and maintained as $\omega_1 < \omega_2 < \omega_3$, causing the tows to undergo a relaxation. Subsequently, the progressive stretching processes can be conducted in the same method.

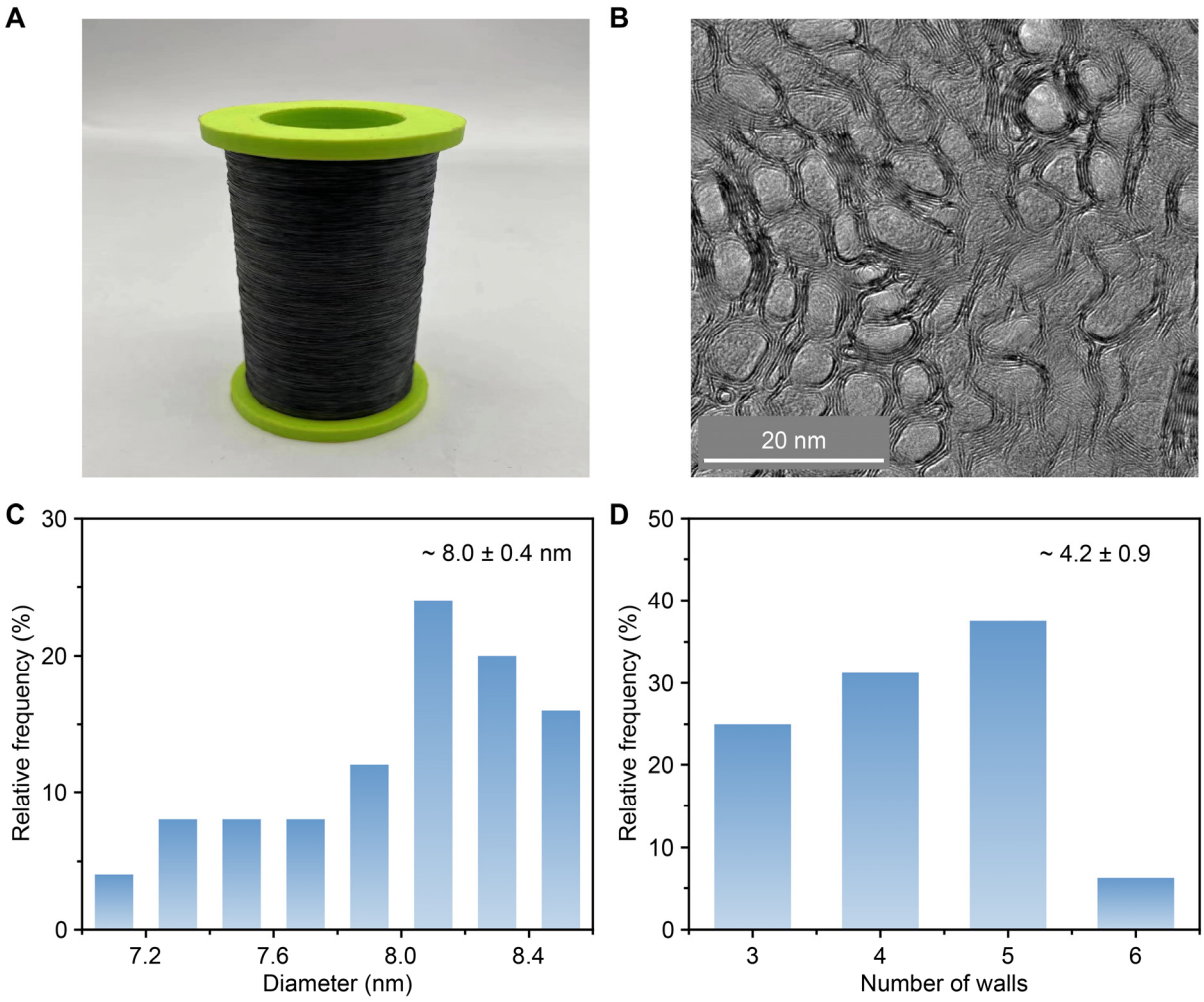

Fig. S3. Pristine CNTFs and structures of CNTs therein.

(**A**) Digital photograph of pristine CNTFs. (**B**) Transmission electron microscopy (TEM) image of the cross section of a pristine CNTF. Distributions of (**C**) diameters and (**D**) number of walls of CNTs.

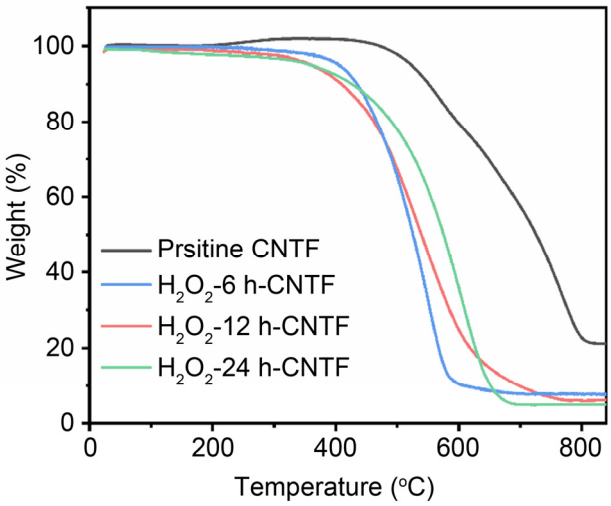

Fig. S4. Thermogravimetric analyses results of pristine CNTFs and F-CNTFs with different oxidation time (6, 12, and 24 h).

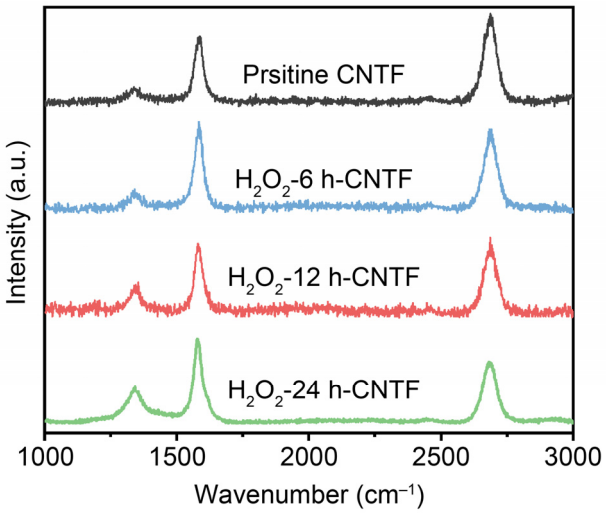

Fig. S5. Raman spectra of pristine CNTFs and F-CNTFs with different oxidation time (6, 12, and 24 h).

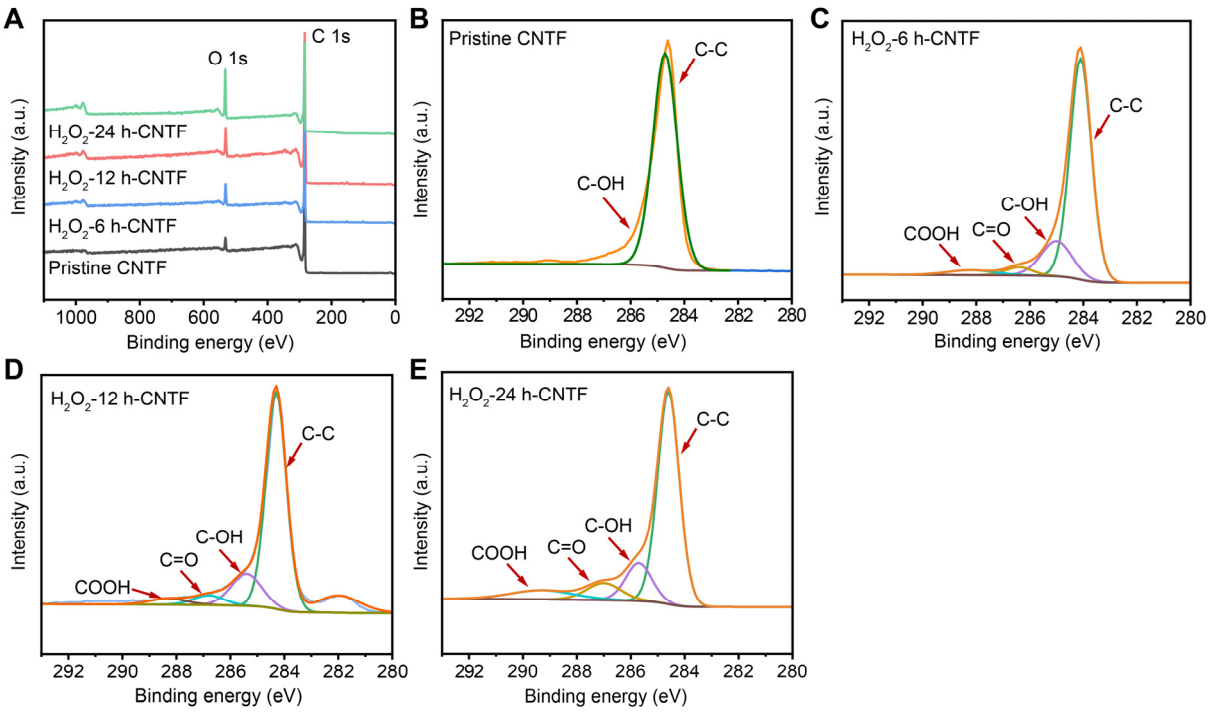

Fig. S6. XPS spectra and C 1s of pristine CNTFs and different F-CNTFs.

(**A**) X-ray photoelectron spectroscopy (XPS) spectra of pristine CNTFs and F-CNTFs. XPS result of C 1s of (**B**) pristine CNTFs and F-CNTFs treated by H_2O_2 solution for (**C**) 6 h, (**D**) 12 h, and (**E**) 24 h.

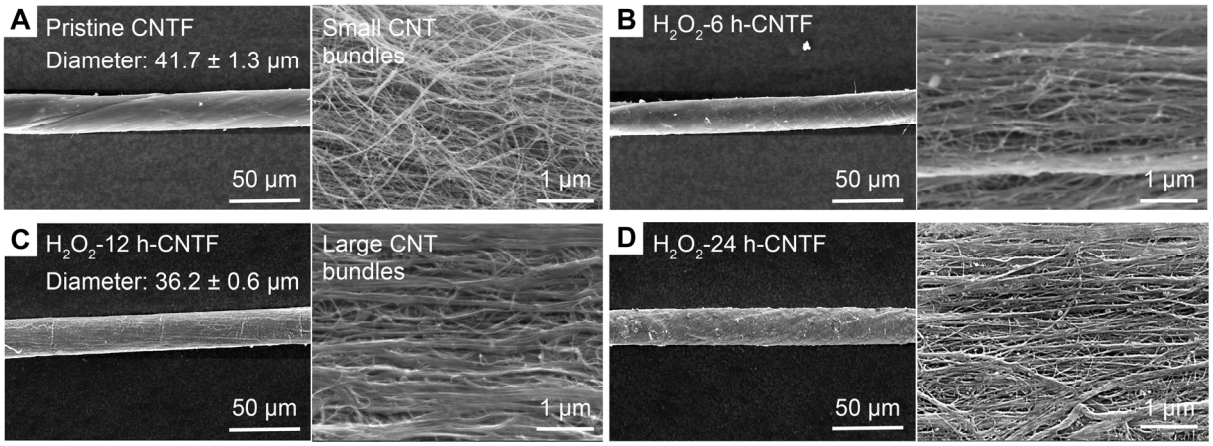

Fig. S7. Morphology of pristine CNTFs and different F-CNTFs.

(**A**) Scanning electron microscopy (SEM) images of pristine CNTFs and F-CNTFs treated by H_2O_2 solution for (**B**) 6 h, (**C**) 12 h, and (**D**) 24 h.

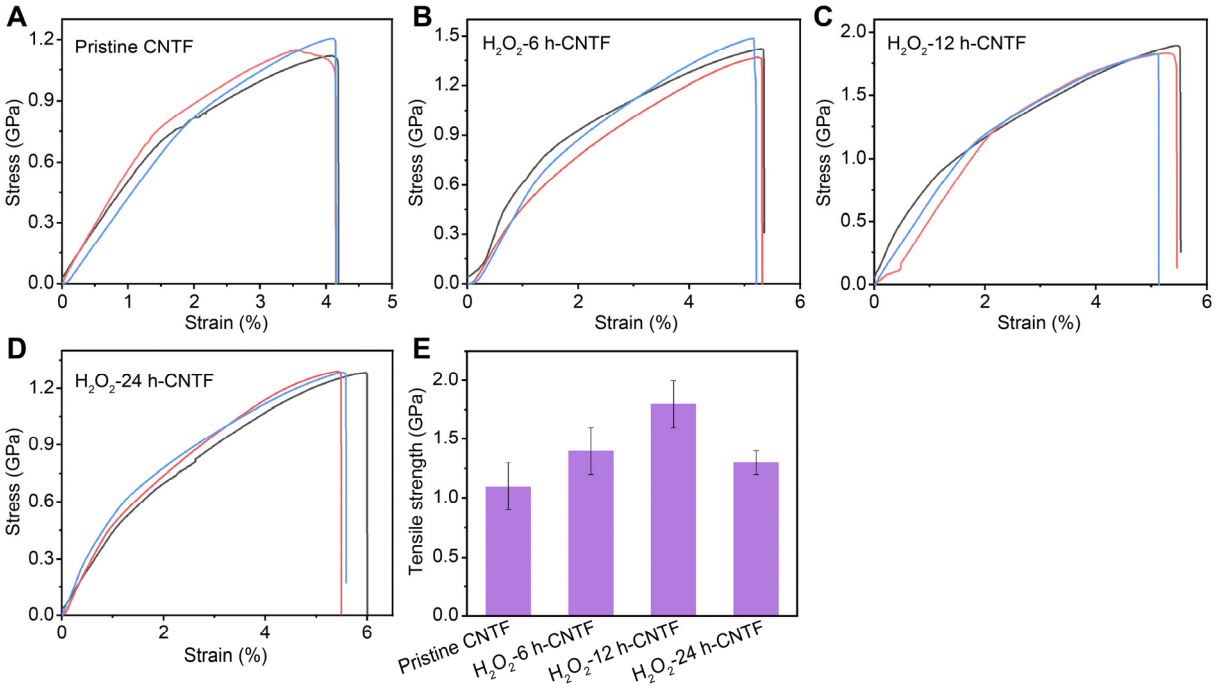

Fig. S8. Comparison of stress-strain curves and tensile strength of pristine CNTFs and different F-CNTFs.

Stress-strain curves of (**A**) pristine CNTFs and F-CNTFs treated with (**B**) 6 h, (**C**) 12 h, and (**D**) 24 h. (**E**) Comparison of the tensile strength of pristine CNTFs and F-CNTFs with different oxidation time (6, 12, and 24 h).

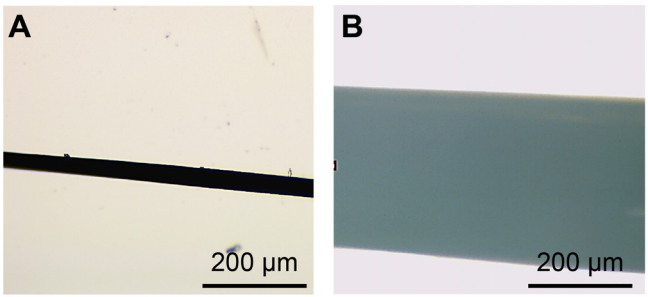

Fig. S9. Optical images of a F-CNTF (A) before and (B) after immersing into the CSA solution.

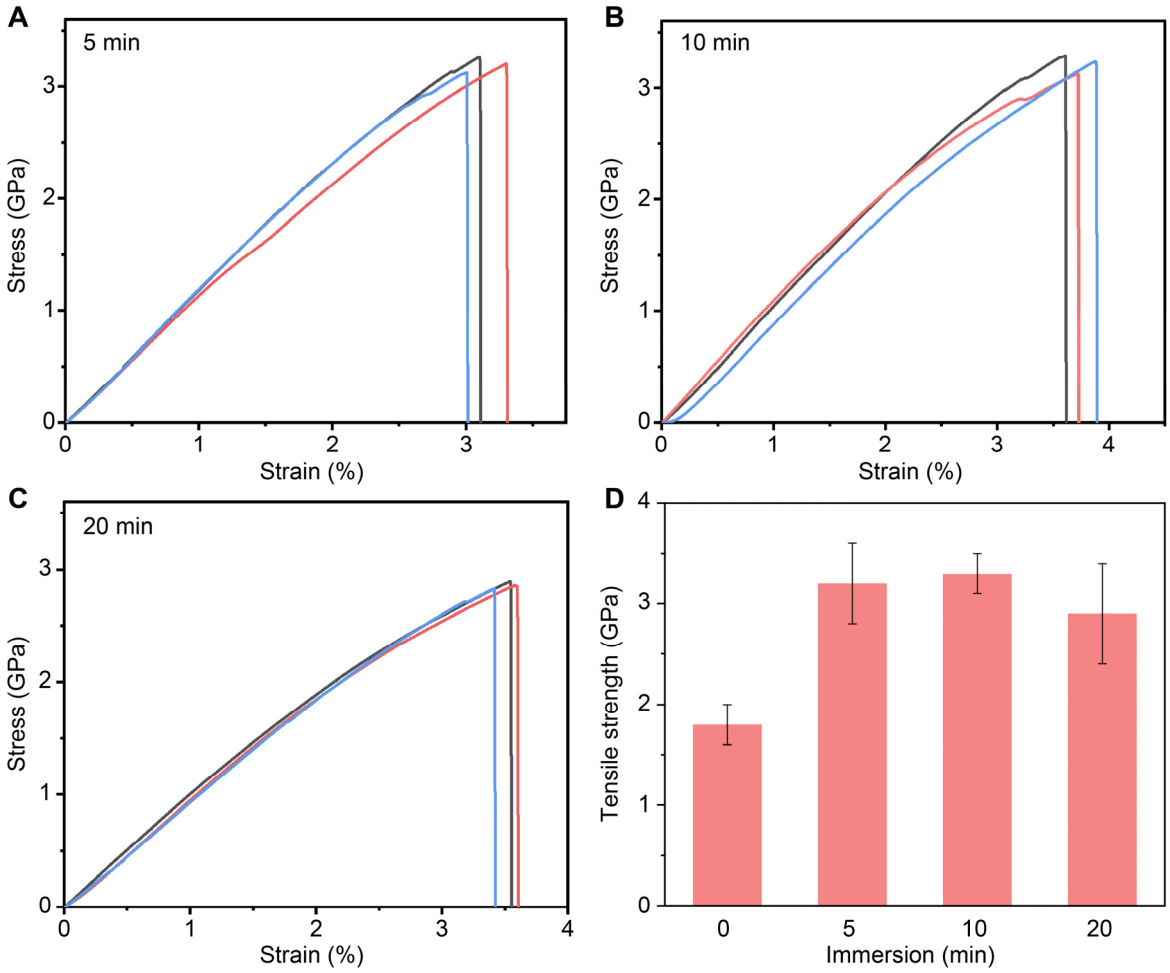

Fig. S10. Comparison of stress-strain curves and tensile strength of fibers with different immersion time.

Stress-strain curves of F-CNTFs treated in CSA solution for (**A**) 5 min, (**B**) 10 min, and (**C**) 20 min. (**D**) Comparison of the tensile strength of F-CNTFs treated in CSA solution with different time.

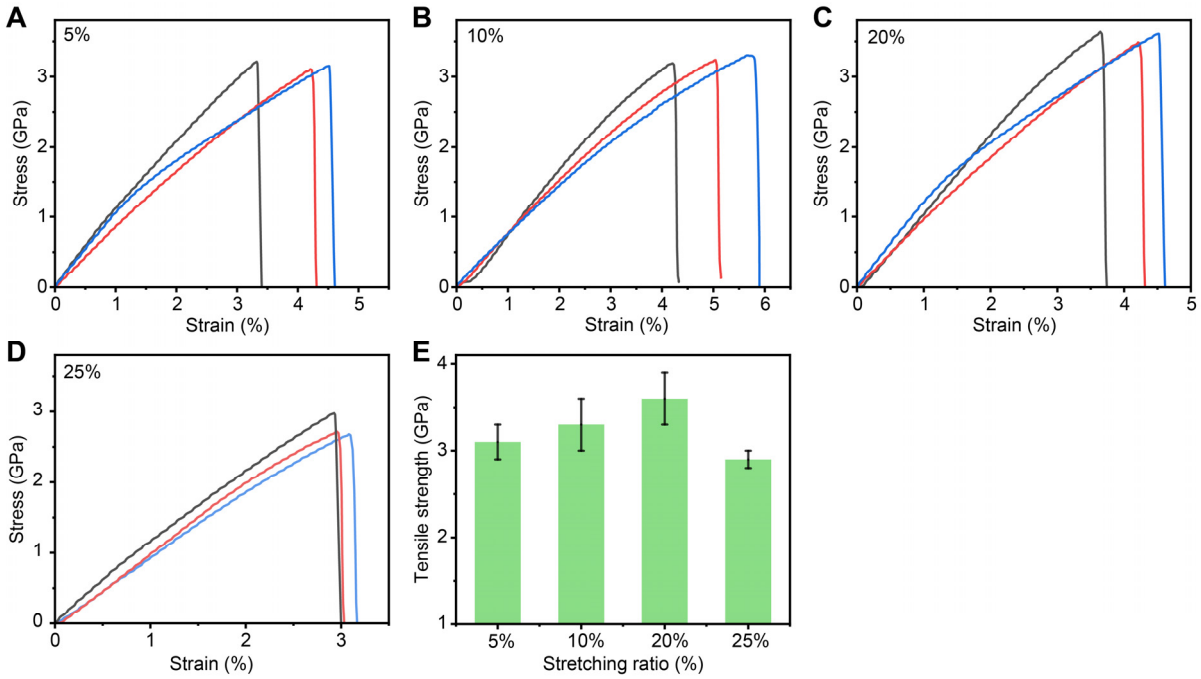

Fig. S11. Comparison of stress-strain curves and tensile strength of fibers with different stretching ratios.

Stress-strain curves of F-CNTFs treated in CSA solution with different stretching ratios of (**A**) 5%, (**B**) 10%, (**C**) 20%, and (**D**) 25%. (**E**) Comparison of the tensile strength of F-CNTFs treated in CSA solution with different stretching ratios.

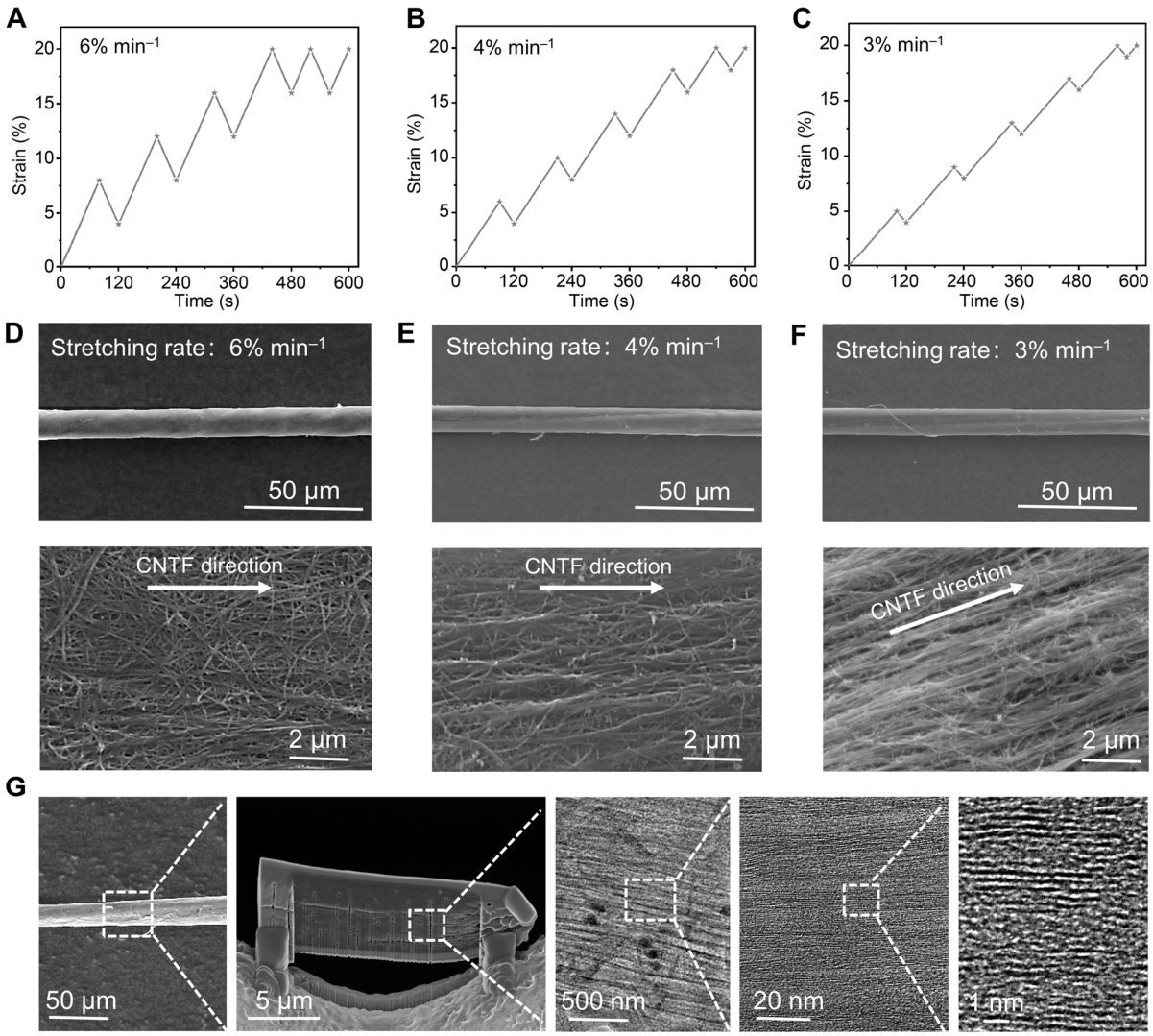

Fig. S12. Fibers prepared by the progressive stretching treatment and their morphology.
Progressive stretching treatment with different stretching rates of (**A**) 6% min^{-1}, (**B**) 4% min^{-1}, and (**C**) 3% min^{-1}. SEM images of F-CNTFs treated by a progressive stretching treatment in CSA solution using different stretching rates of (**D**) 6% min^{-1}, (**E**) 4% min^{-1}, and (**F**) 3% min^{-1}. (**G**) SEM and TEM images of the axial cross-section of F-CNTFs treated with a stretching rate of 3% min^{-1}.

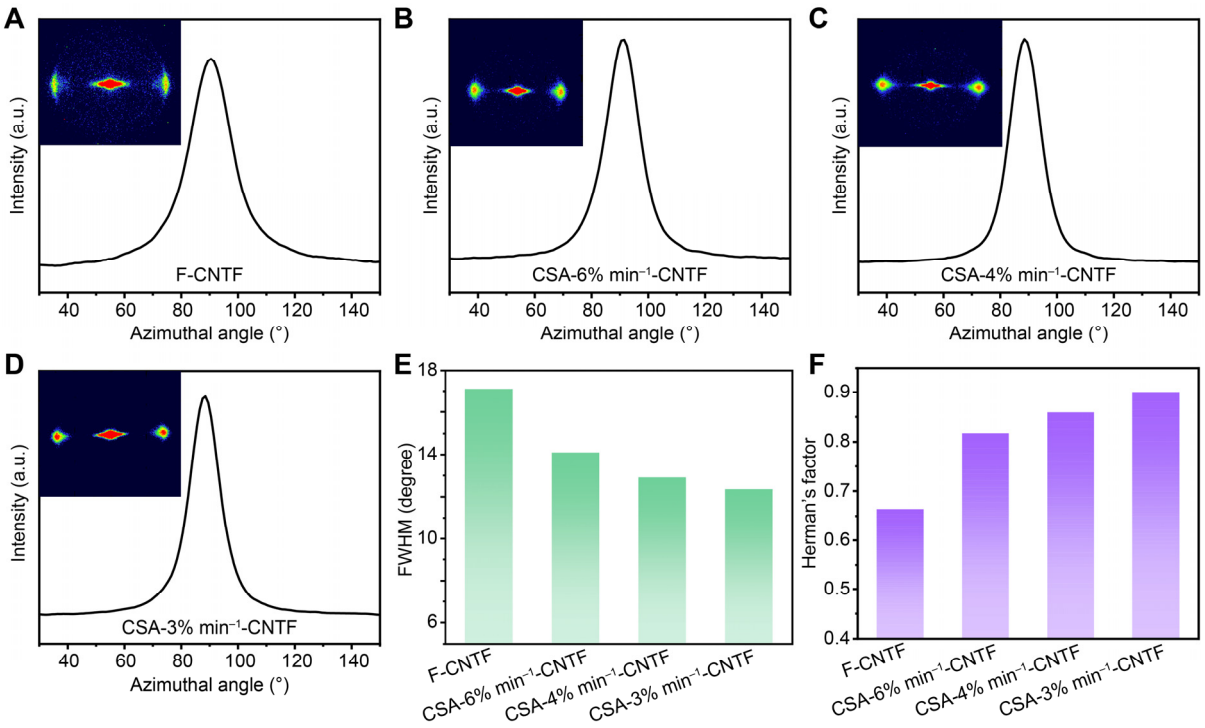

Fig. S13. WAXS analyses of fibers treated by the progressive stretching treatment with different stretching rates.

Two-dimensional (2D) wide angle X-ray scattering (WAXS) analyses of (**A**) F-CNTFs without the progressive stretching treatment and as-treated F-CNTFs by progressive stretching with different stretching rates of (**B**) 6% min^{-1}, (**C**) 4% min^{-1}, and (**D**) 3% min^{-1}. Comparison of the (**E**) full width at half maximum (FWHM) and (**F**) Herman's factor of different CNTFs.

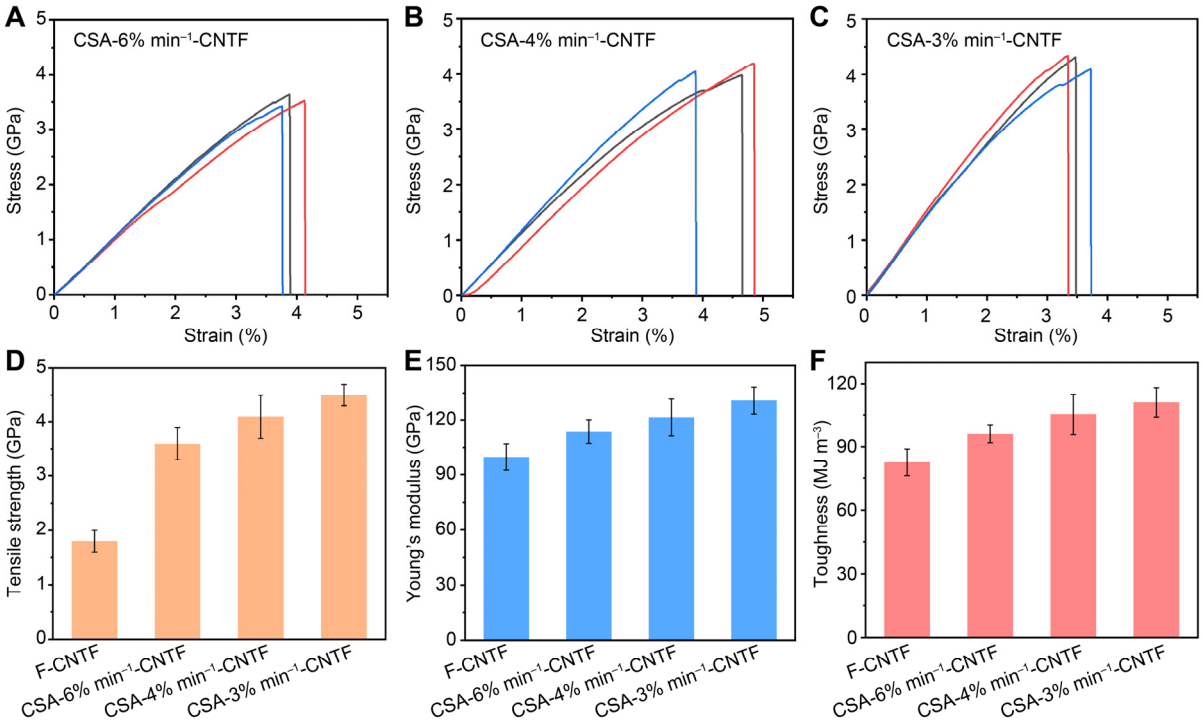

Fig. S14. Comparison of stress-strain curves and quasi-static mechanical properties of fibers treated by the progressive stretching treatment with different stretching rates.

Stress-strain curves of F-CNTFs treated by the progressive stretching treatment in CSA solution using different stretching rates of (**A**) 6% min^{-1}, (**B**) 4% min^{-1}, and (**C**) 3% min^{-1}. Comparison of the (**D**) quasi-static tensile strength, (**E**) Young's modulus, and (**F**) toughness of different fibers.

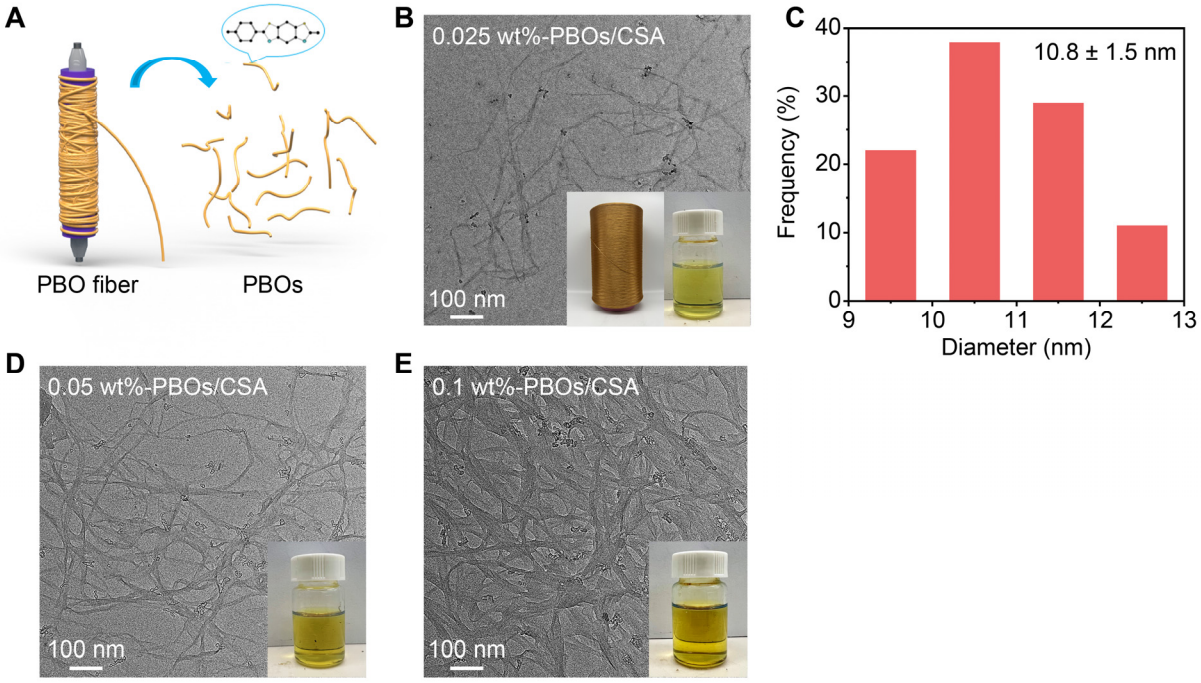

Fig. S15. Preparation and morphology characterization of PBOs.

(**A**) Schematic diagram for the preparation of PBOs derived from PBO fibers. (**B**) TEM image of PBO nanofibers with PBO concentration of 0.025 wt% in CSA solution. (**C**) Statistic analysis of diameters of PBO nanofibers. TEM images of PBO nanofibers with PBO concentration of (**D**) 0.05 wt% and (**E**) 0.1 wt%.

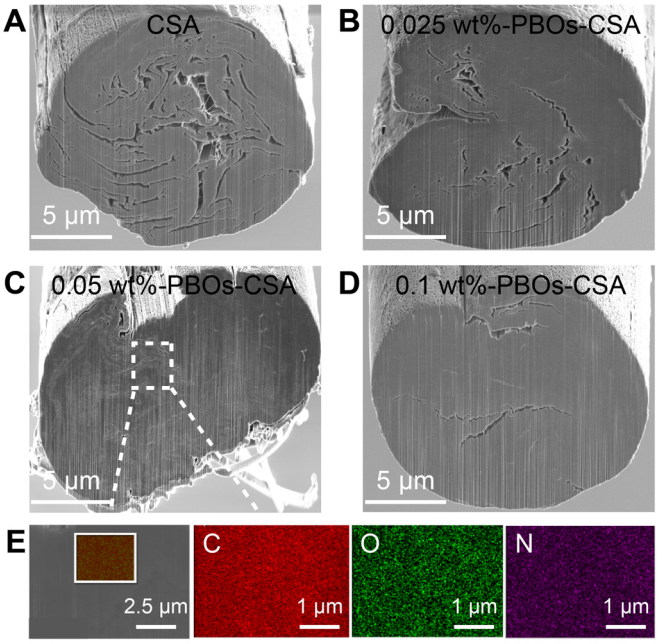

Fig. S16. SEM images and EDS results of the radial cross section of different fibers.

SEM images of cross sections (cut by a focused ion beam) of different fibers prepared by the progressive stretching treatment in (**A**) CSA solution, PBOs-CSA solution with the concentration of (**B**) 0.025 wt%, (**C**) 0.05 wt%, and (**D**) 0.1 wt%. (**E**) Corresponding selected area energy dispersive spectroscopy (EDS) of PBO-CNTFs in (C).

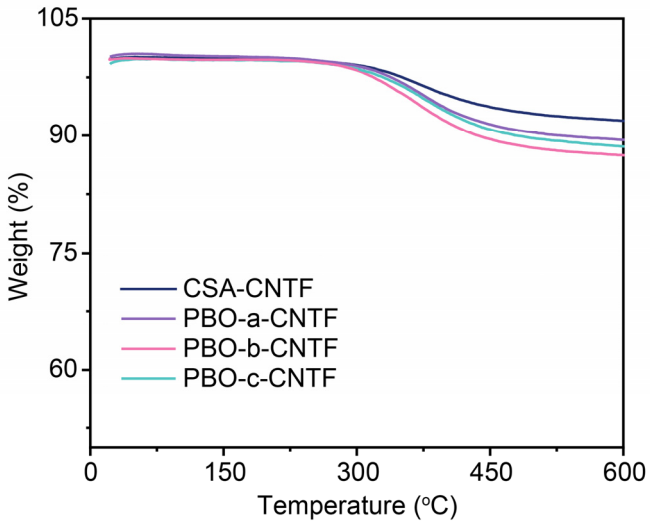

Fig. S17. Thermogravimetric analyses of different CNTFs.

Thermogravimetric analyses of CSA-CNTFs and PBO-CNTFs treated in PBOs-CSA solutions with the PBO concentration of 0.025 wt% (PBO-a-CNTFs), 0.05 wt% (PBO-b-CNTFs), 0.1 wt% (PBO-c-CNTFs) under a nitrogen atmosphere, respectively. The resultant PBOs contents of PBO-a-CNTFs, PBO-b-CNTFs, and PBO-c-CNTFs are 7.2 wt%, 10.9 wt%, and 8.9 wt%, respectively.

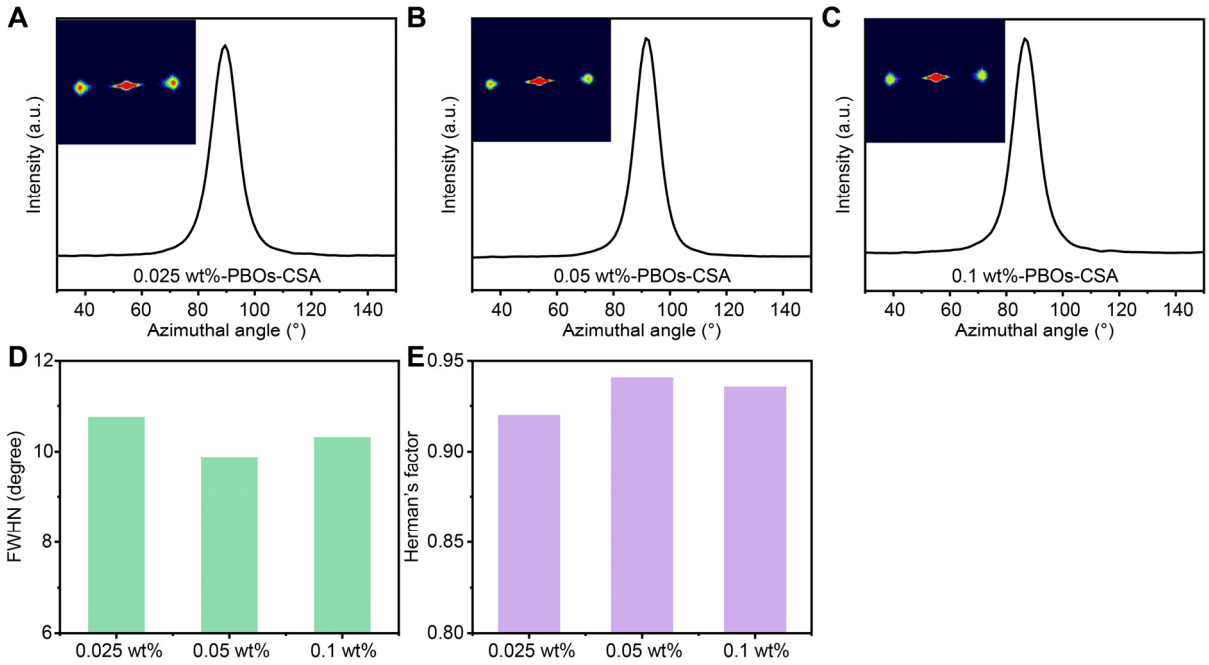

Fig. S18. 2D-WAXS analyses of different PBO-CNTFs.

2D-WAXS results of PBO-CNTFs produced by the progressive stretching treatment in PBOs-CSA solution with the concentration of (**A**) 0.025 wt%, (**B**) 0.05 wt%, and (**C**) 0.1 wt%. Comparison of the (**D**) FWHM and (**E**) Herman's factor of different fibers.

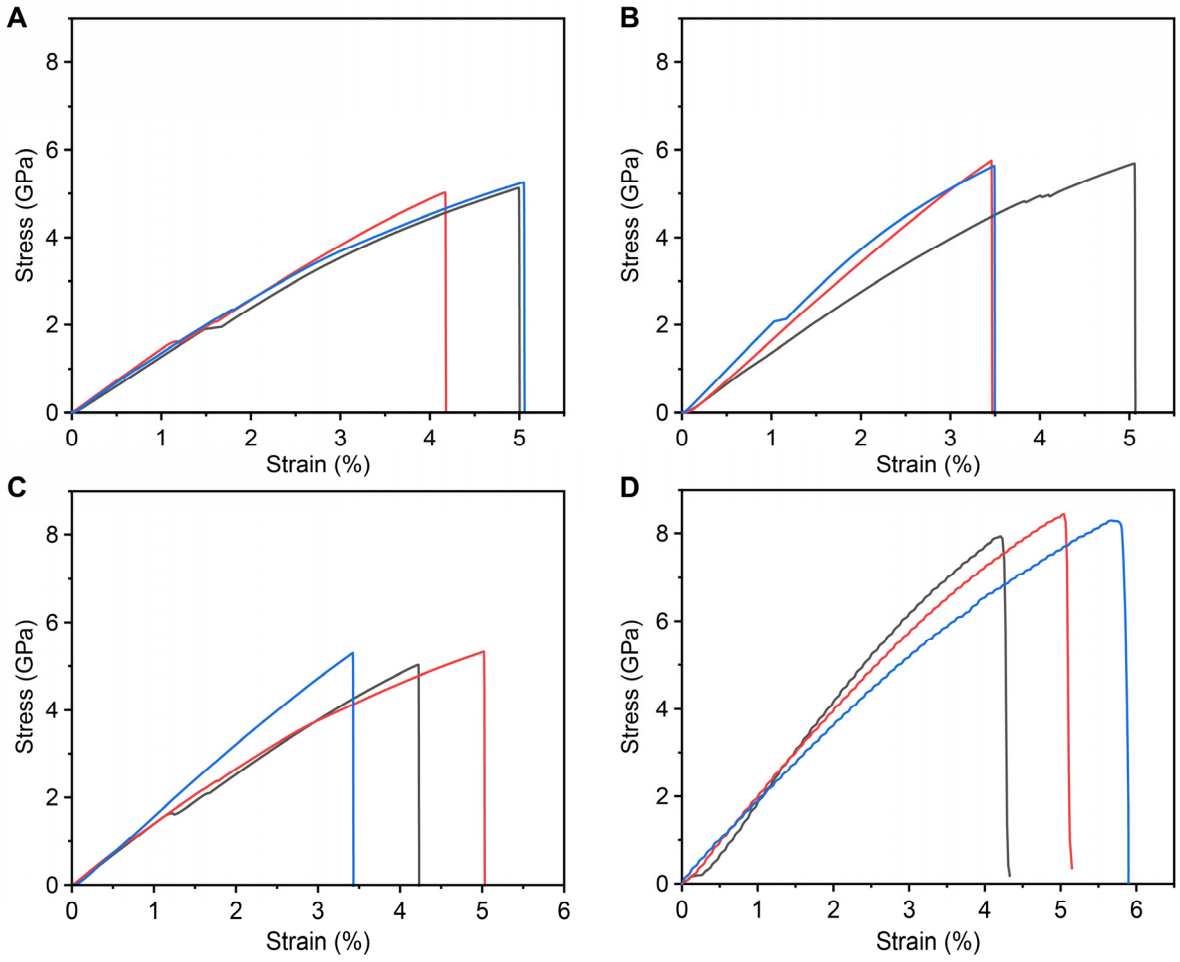

Fig. S19. Stress-strain curves of different PBO-CNTFs and D-PBO-CNTFs.

Stress-strain curves of PBO-CNTFs obtained by the progressive stretching treatment in PBOs-CSA solution with the concentration of (**A**) 0.025 wt%, (**B**) 0.05 wt%, and (**C**) 0.1 wt%. (**D**) Stress-strain curves of D-PBO-CNTFs prepared by the combination of progressive stretching treatment in PBOs-CSA solution with a concentration of 0.05 wt% and mechanical densification.

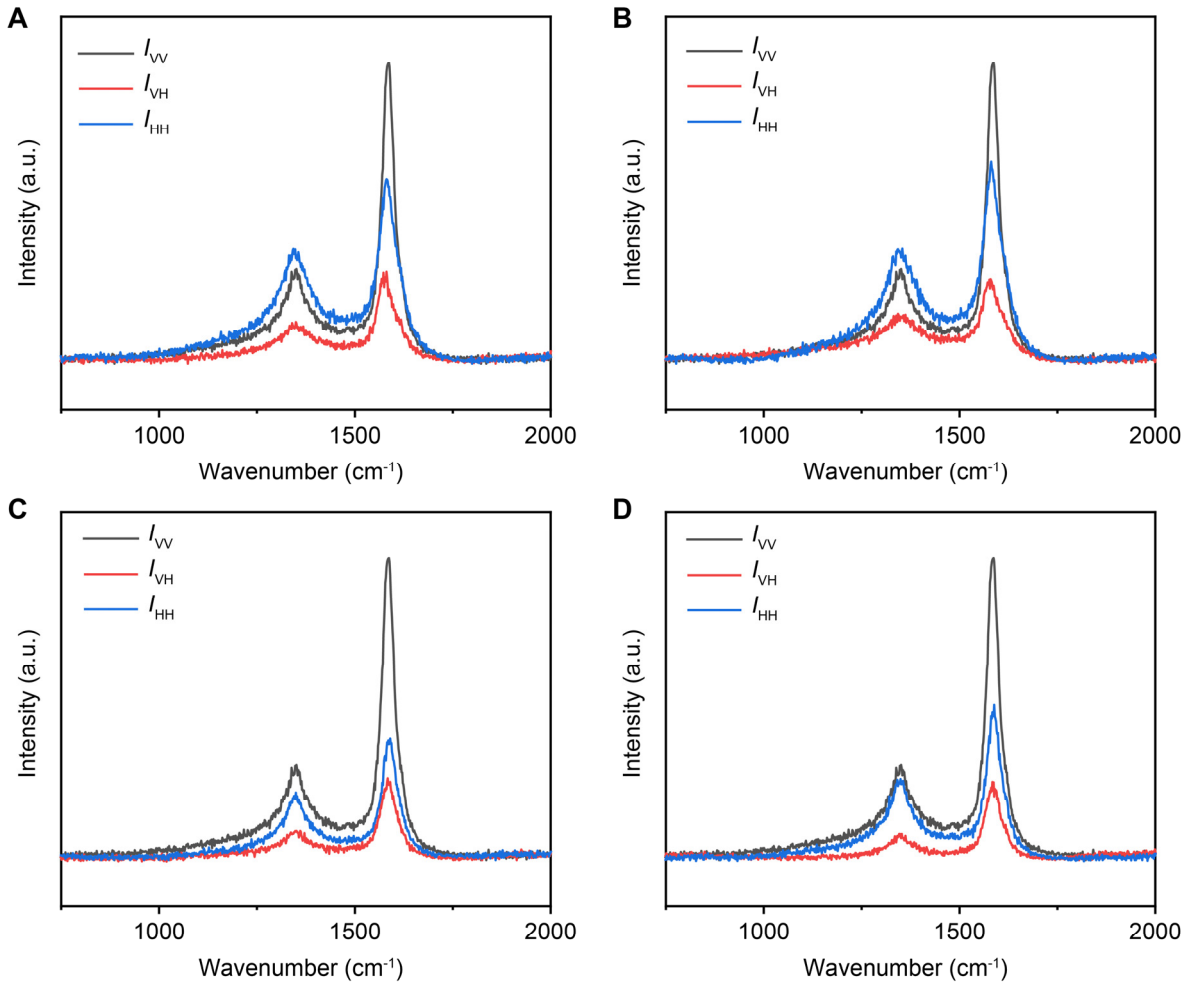

Fig. S20. Polarized Raman spectra of different CNTFs.

Polarized Raman spectra of (**A**) F-CNTFs, (**B**) CSA-CNTFs, (**C**) PBO-CNTFs, and (**D**) D-PBO-CNTFs. The values of orientational order parameters (*s*) for F-CNTFs, CSA-CNTFs, PBO-CNTFs, and D-PBO-CNTFs are 0.46 ± 0.2, 0.78 ± 0.1, 0.85 ± 0.3, and 0.82 ± 0.2, respectively.

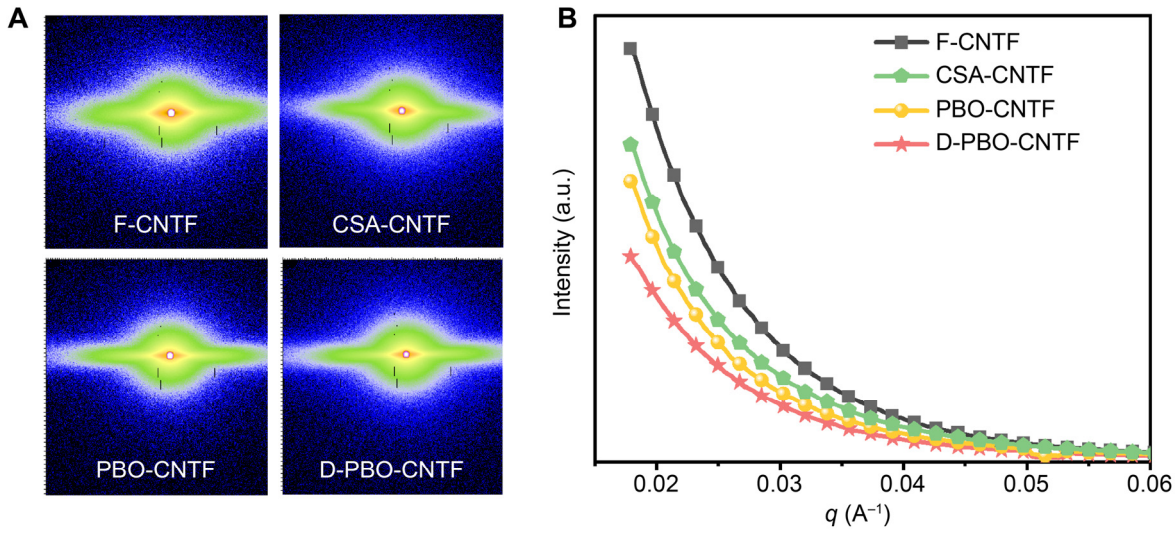

Fig. S21. SAXS analyses of different fibers.

(**A**) Small angle x-ray scattering (SAXS) pattern of F-CNTFs, CSA-CNTFs, PBO-CNTFs, and D-PBO-CNTFs. (**B**) Scattering intensity of the fiber streak as a function of q along the equator for different fibers.

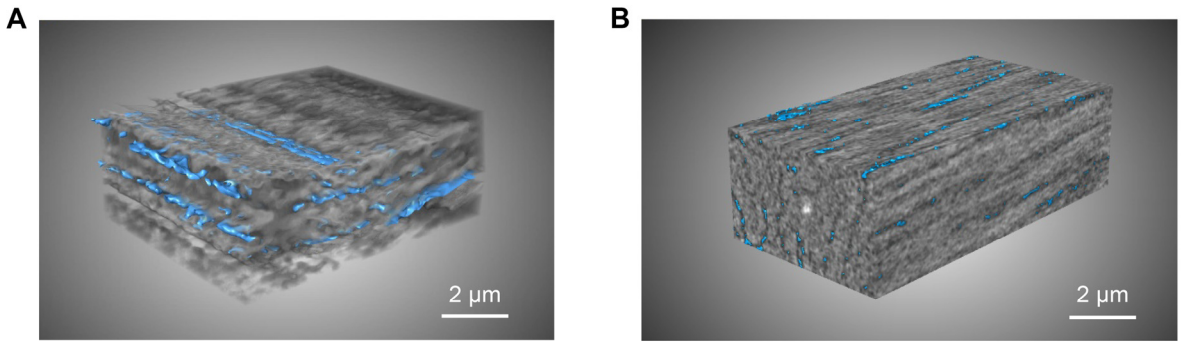

Fig. S22. 3D void microstructures of fibers reconstructed by nanoscale x-ray computed tomography.

Three-dimensional (3D) void microstructures of (**A**) CSA-CNTFs, and (**B**) D-PBO-CNTFs (blue represents the voids within the fibers).

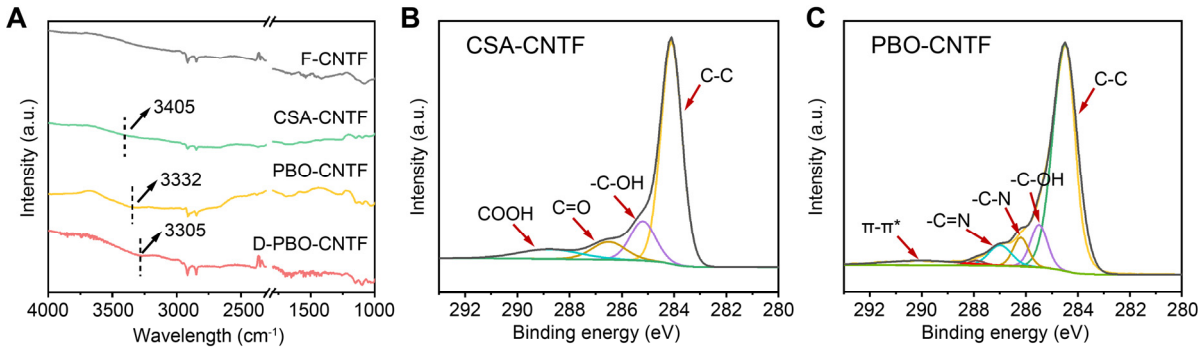

Fig. S23. FTIR and XPS spectra of different fibers.

(**A**) Fourier transform infrared (FTIR) spectra of F-CNTFs, CSA-CNTFs, and PBO-CNTFs. FTIR spectra show that the stretching vibration peak of hydroxy groups (-OH) for CSA-CNTFs (3405 cm^{-1}) is redshifted to 3332 cm^{-1} for PBO-CNTFs and 3305 cm^{-1} for D-PBO-CNTFs, verifying the hydrogen bonding between CNTs and PBOs. High-resolution XPS spectra of C 1s of (**B**) CSA-CNTFs and (**C**) PBO-CNTFs. Compared with the CSA-CNTFs, the XPS spectrum of PBO-CNTFs shows a new -C-N peak at 286.1 eV and a -C=N peak at 287.1 eV, demonstrating the successful introduction of PBOs into CNTFs.

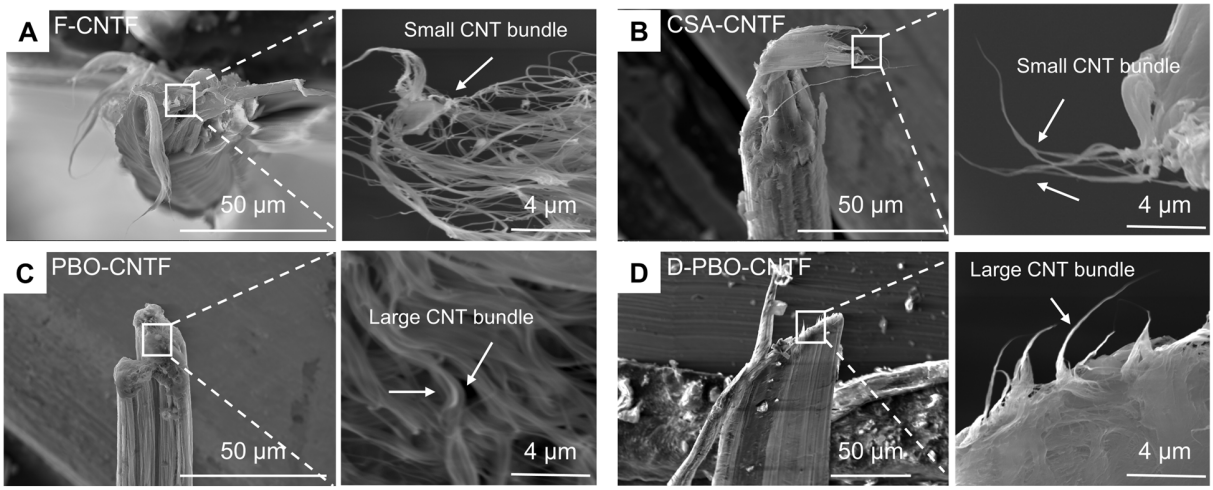

Fig. S24. SEM images of the fracture morphologies of different fibers.

SEM images of the fracture morphologies of (**A**) F-CNTFs, (**B**) CSA-CNTFs, (**C**) PBO-CNTFs, and (**D**) D-PBO-CNTFs under the quasi-static testing.

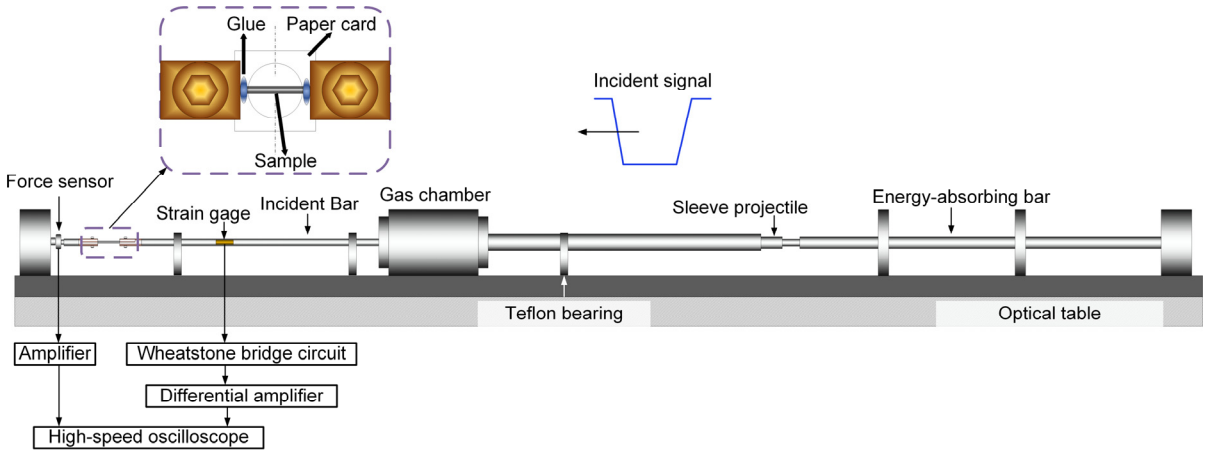

Fig. S25. Schematic diagram of the mini-split Hopkinson tension bar (mini-SHTB) experiment.

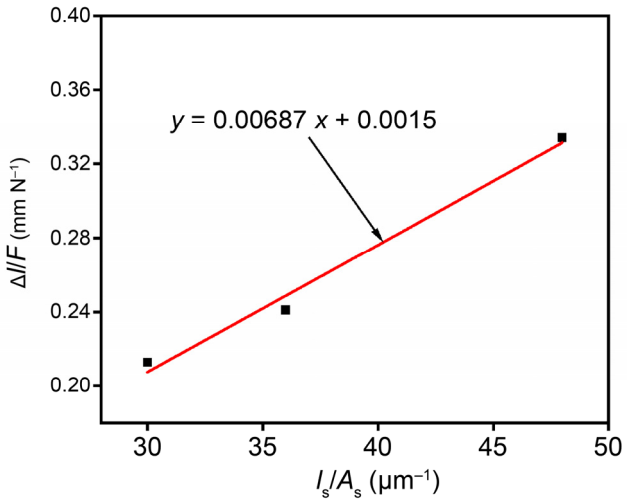

Fig. S26. Calculation of fixture compliance using the fitted curve's zero-gauge length intercept.

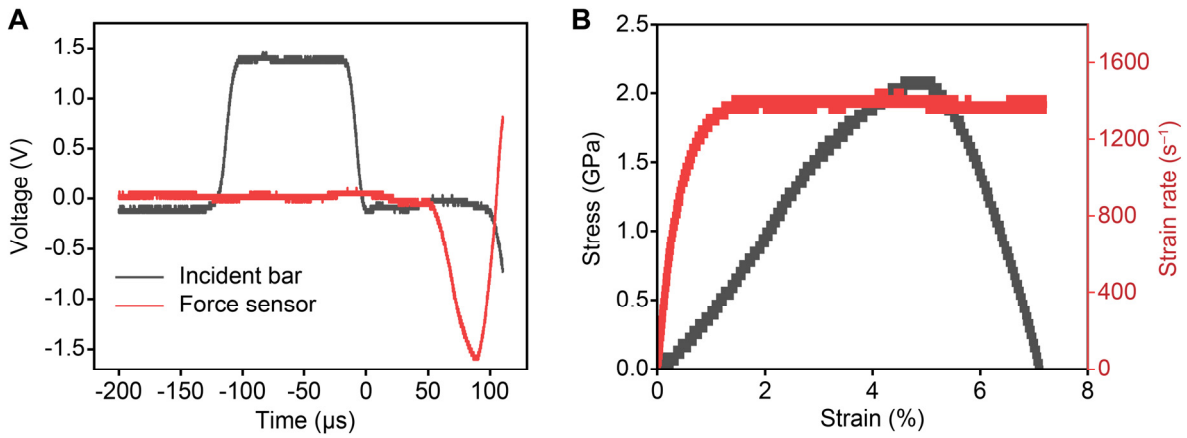

Fig. S27. Analyses of dynamic tensile strength of F-CNTFs.

(**A**) Typical signals of the incident wave and force. (**B**) Typical stress-strain curve and strain rate-strain curve.

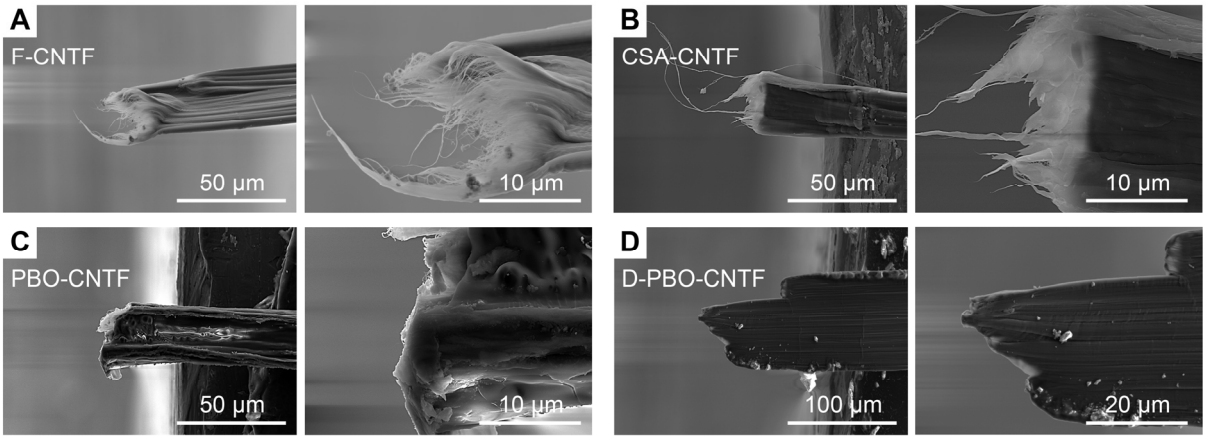

Fig. S28. SEM images of the fracture morphologies of different fibers under high strain rates. SEM images of the fracture morphologies of (**A**) F-CNTFs, (**B**) CSA-CNTFs, (**C**) PBO-CNTFs, and (**D**) D-PBO-CNTFs at the strain rates of about 1400 s^{-1}.

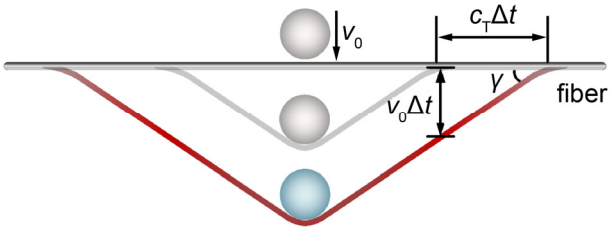

Fig. S29. Schematic diagram of high-velocity transverse impact on a fiber.

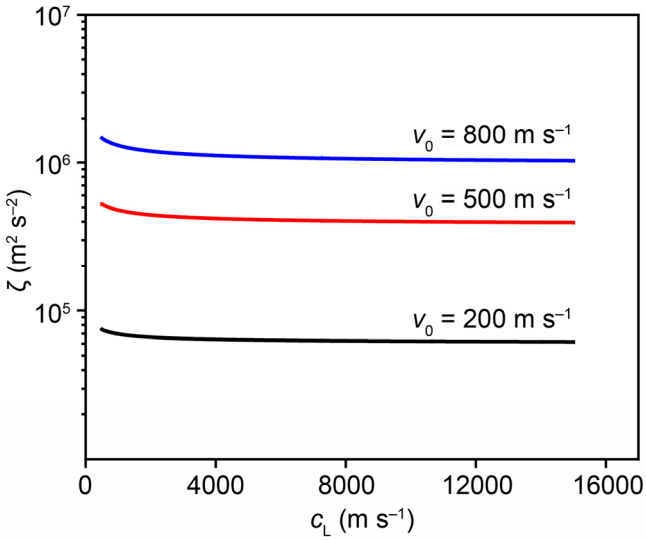

Fig. S30. Relationship between c_L and ζ in Eq. (28) for v_0 of 200, 500, and 800 m s^{-1}.

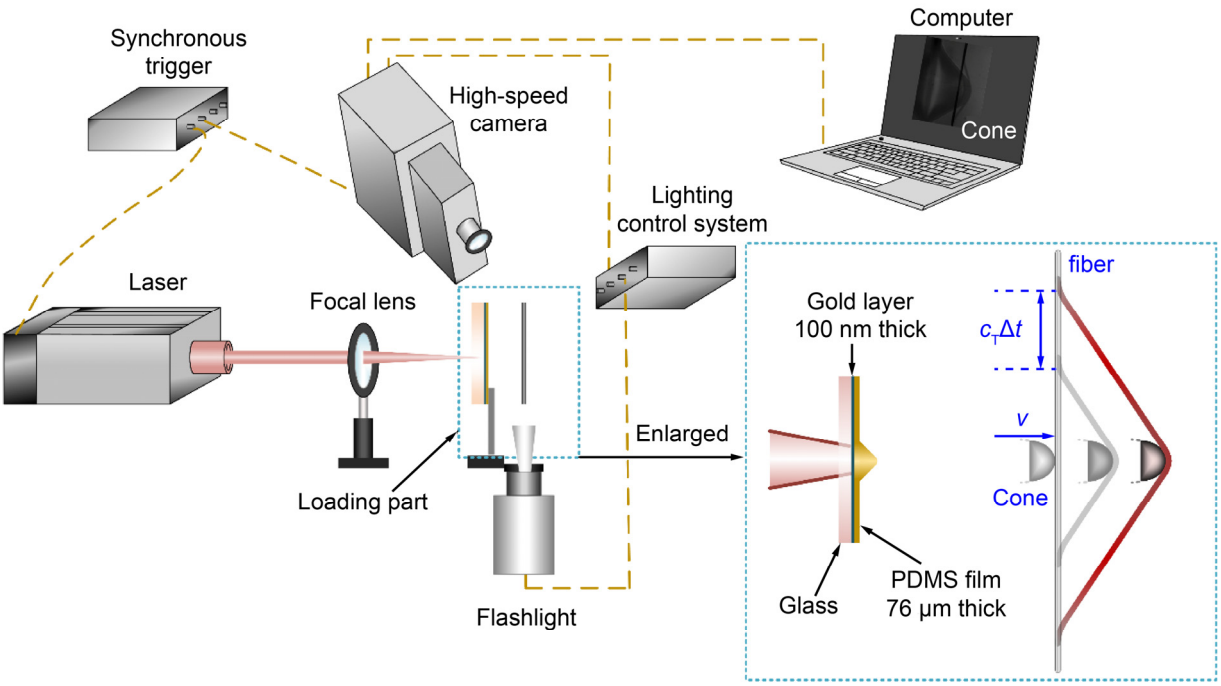

Fig. S31. Schematic diagram of the laser-induced high-velocity transverse impact on a fiber.

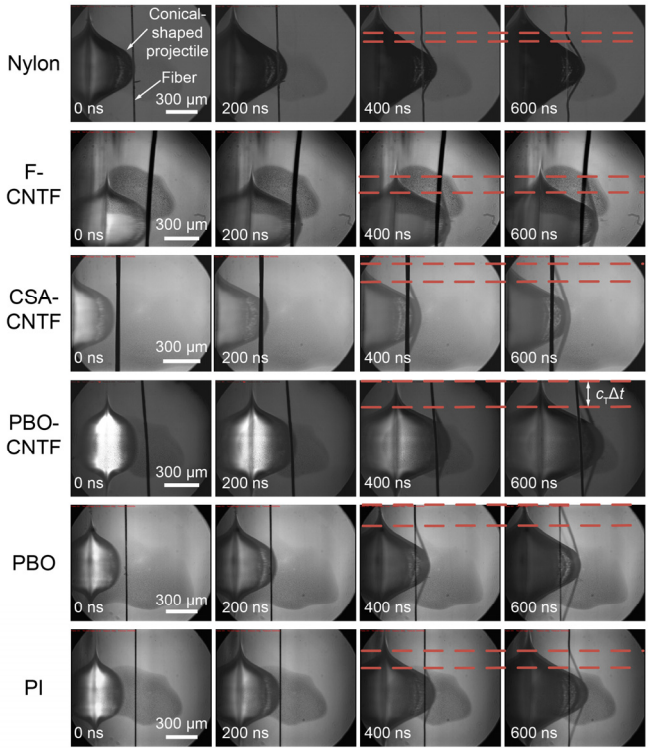

Fig. S32. Deformation processes of nylon fiber, F-CNTF, CSA-CNTF, PBO-CNTF, PBO fiber, and polyimide (PI) fiber under high-velocity transverse impact.

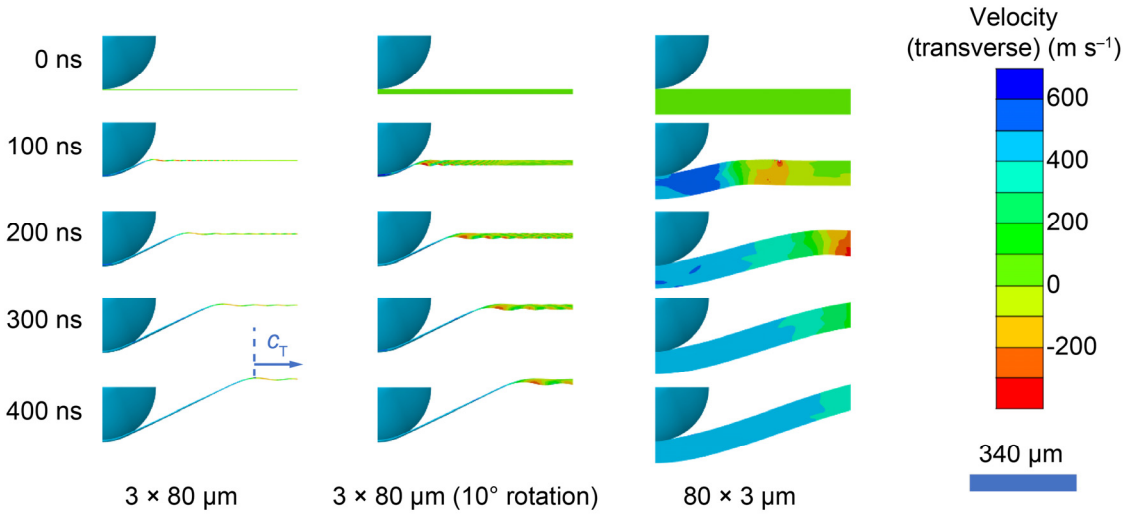

Fig. S33. Simulated impact responses of the single fibers with different bending stiffness along the impact direction. The fibers have the same cross-sectional area.

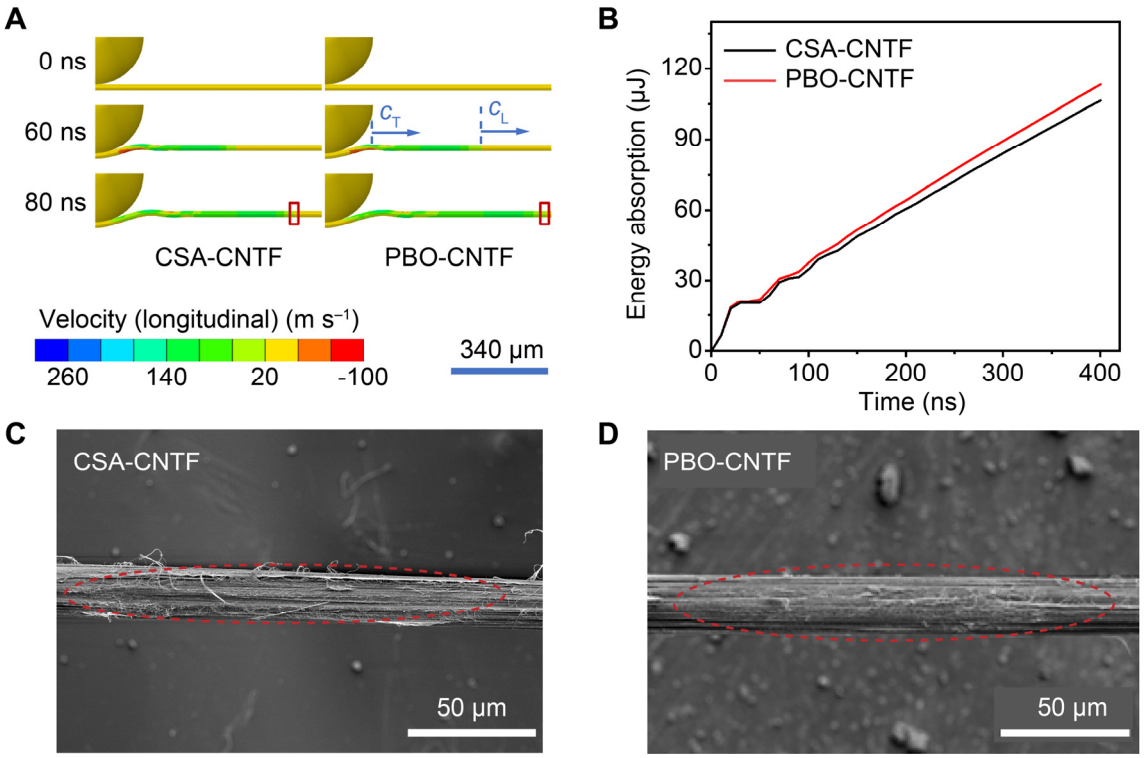

Fig. S34. Finite element simulations on the dynamic deformation processes of fibers and SEM images of fibers after the impact.

(**A**) Finite element simulated transverse impact behavior of CSA-CNTF and PBO-CNTF. (**B**) Energy absorption of CSA-CNTF and PBO-CNTF. SEM images of (**C**) CSA-CNTF and (**D**) PBO-CNTF after the transverse impact testing. The red dash boxes indicate the impact regions.

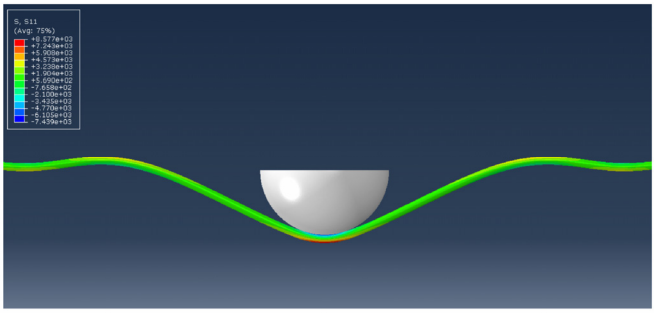

Fig. S35. Deformation of the fiber under an impact of 400 ns.

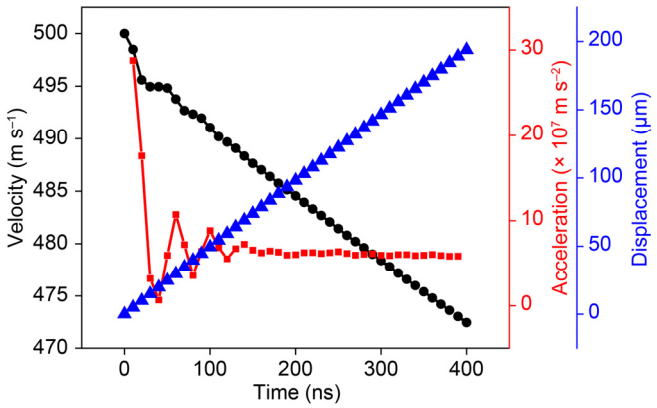

Fig. S36. Displacement, velocity, and acceleration history of the conic PDMS film.

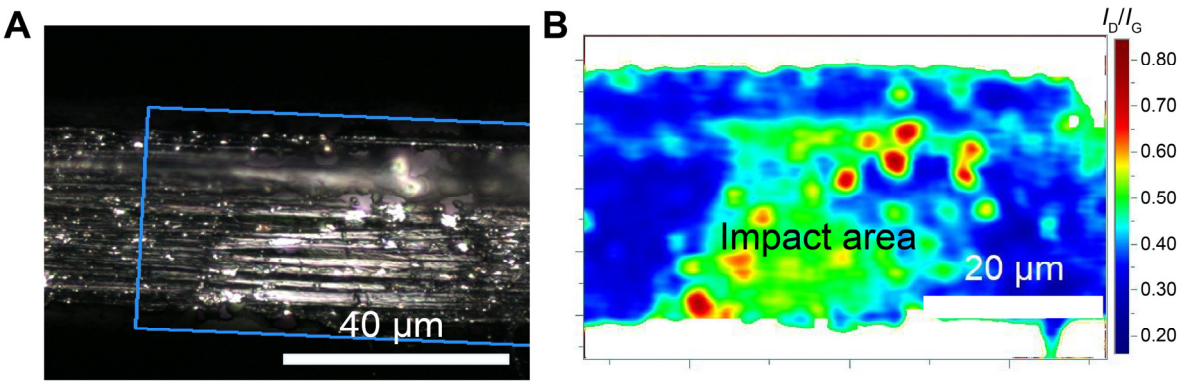

Fig. S37. Raman mapping of a PBO-CNTF after the high-velocity impact.

(**A**) Raman mapping area of the PBO-CNTF after the high-velocity impact. (**B**) Raman map of the I_D/I_G on the impact area of the fibers.

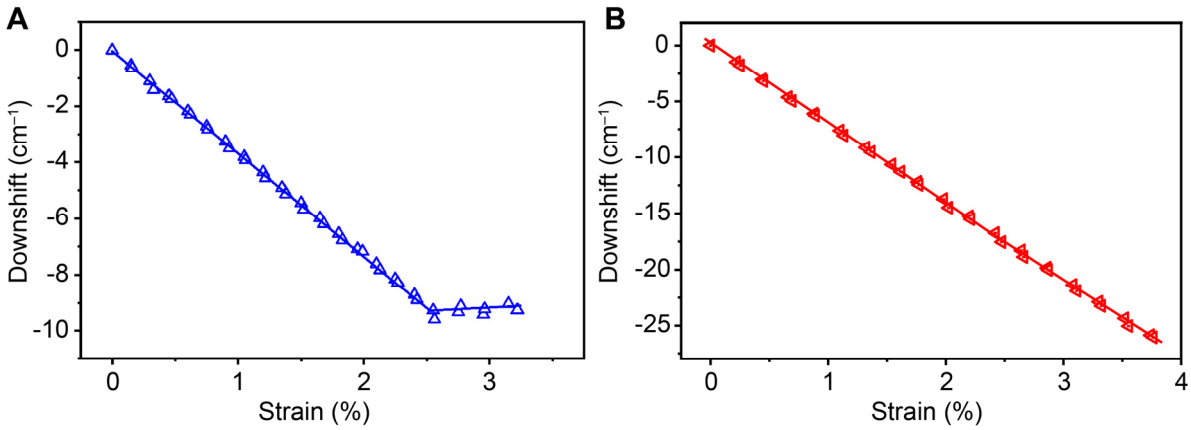

Fig. S38. Dependence of Raman frequency downshifts on the applied strains.
Raman frequency downshifts of (**A**) CSA-CNTFs and (**B**) D-PBO-CNTFs.

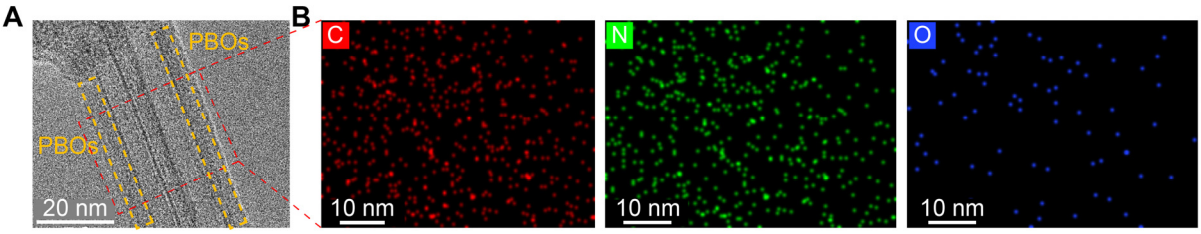

Fig. S39. TEM image and EDS characterization of modified fibers.
(**A**) TEM image of PBOs adsorbed onto CNTs and (**B**) EDS characterization of the corresponding selected area (nitrogen is only from PBOs).

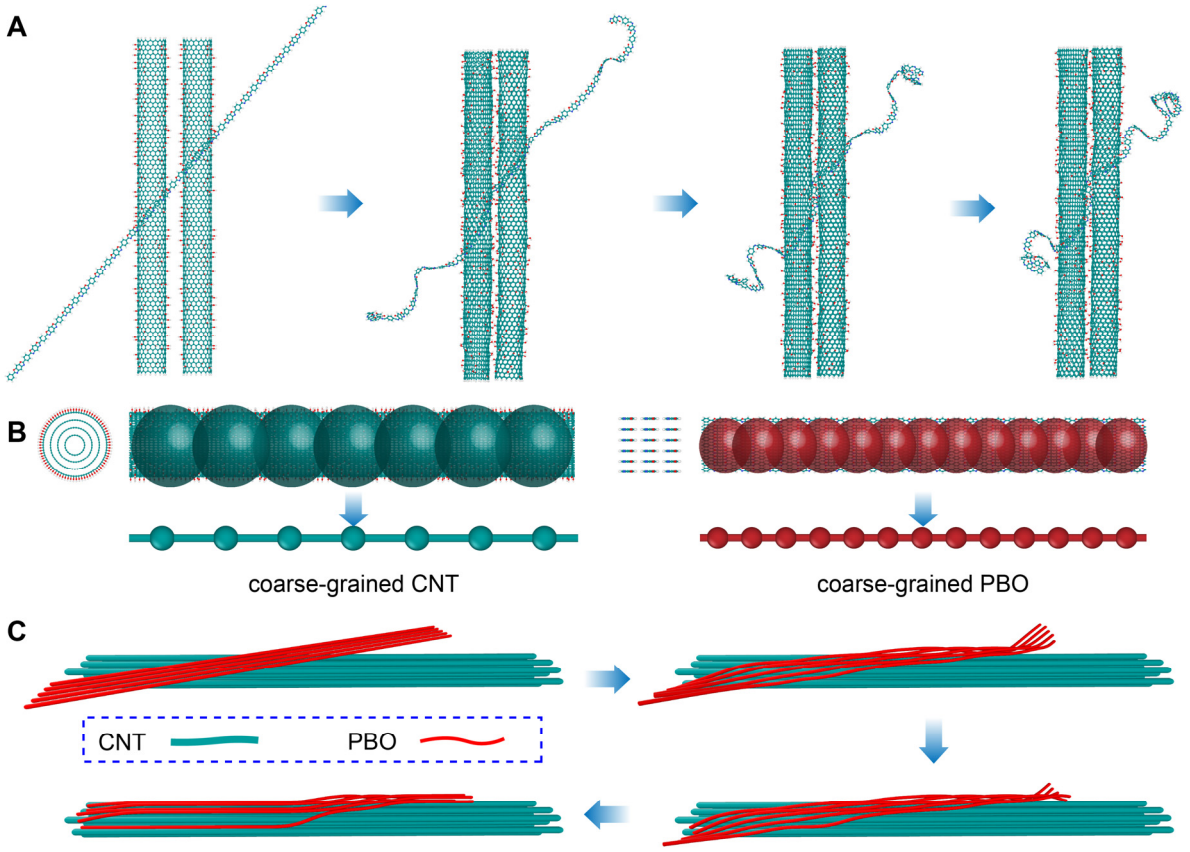

Fig. S40. Adsorption of PBOs on CNTs.

(**A**) Adsorption of a PBO chain on CNTs. (**B**) All-atom models and the corresponding coarse-grained models of CNTs and PBOs. (**C**) Adsorption of PBO nanofibers on CNT bundles.

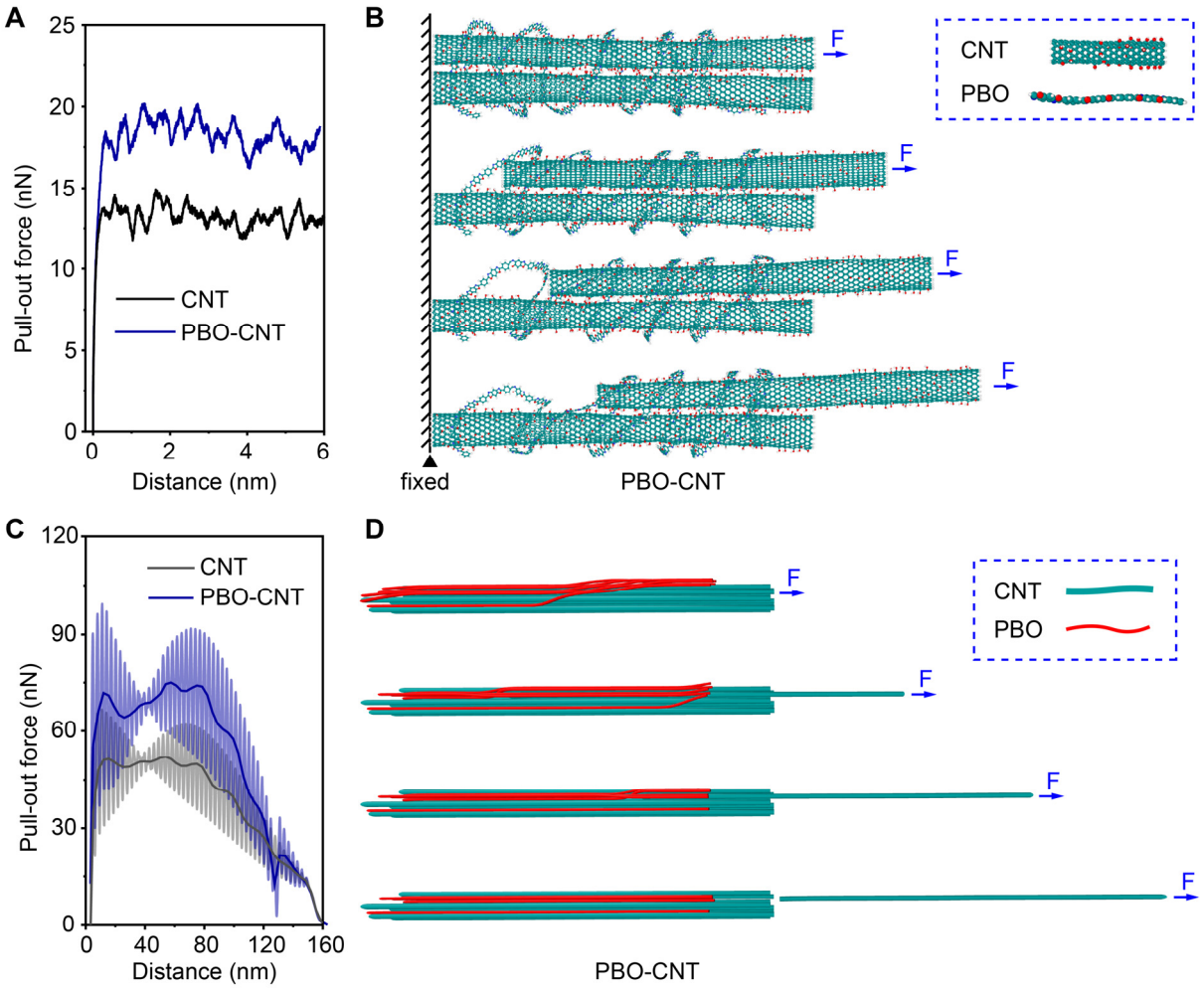

Fig. S41. Pull-out tests of CNTs with and without the addition of PBOs.

(**A**) Relationship between the pull-out force and distance of CNTs with and without the addition of PBO chains. (**B**) Snapshots of atomistic simulations of pull-out tests of CNTs with the addition of PBO chains. (**C**) Relationship between pull-out force and distance of CNTs with and without the addition of PBO nanofibers. (**D**) Snapshots of coarse-grained simulations of pull-out tests of CNTs with the addition of PBO nanofibers.

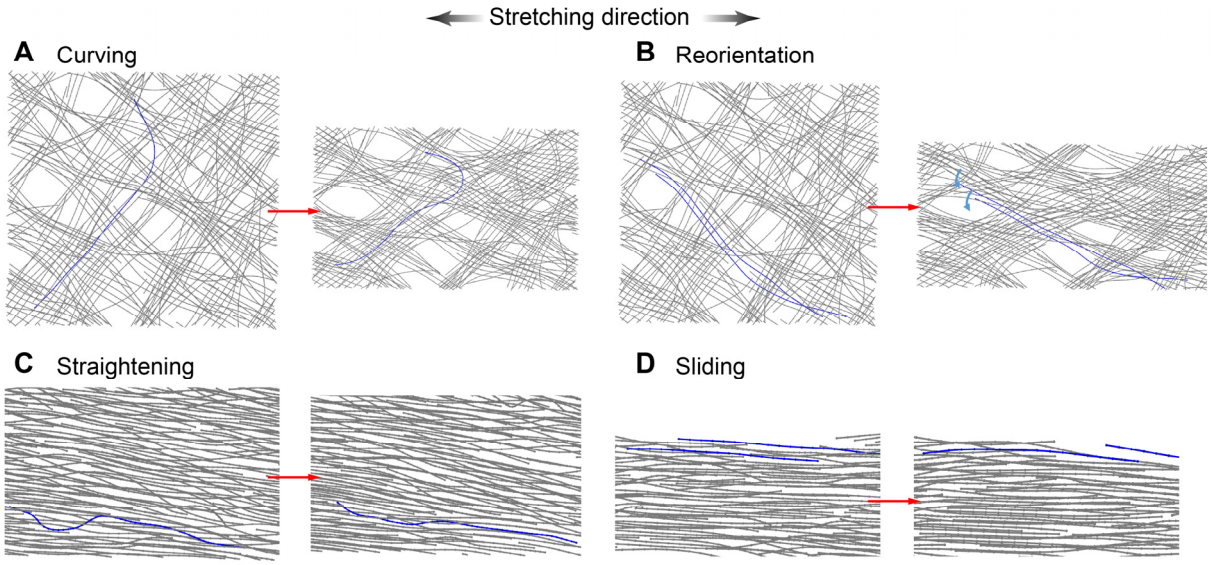

Fig. S42. Reorganization of microstructures of fibers during the progressive stretching treatment.

Reorganization of fibers movements (highlighted snapshots before and after movement) including (**A**) curving, (**B**) reorientation, (**C**) straightening, and (**D**) sliding.

Table S1. Degree of oxidation, I_G/I_D, residual mass, and tensile strength of pristine CNTFs and F-CNTFs with different oxidation time.

Oxidation time (h)	C/O ratio	Hydroxy group content (at. %)	I_G/I_D	Residual mass (%)	Tensile strength (GPa)
0	26.7	3.7	4.7	21.2	1.1 ± 0.2
6	12.9	10.2	4.5	9.5	1.4 ± 0.2
12	10.9	14.2	3.1	7.2	1.8 ± 0.2
24	4.8	15.6	2.6	6.1	1.3 ± 0.1

Table S2. Mechanical properties of F-CNTFs treated in a CSA bath with different time.

Immersion time (min)	Tensile strength (GPa)	Young's modulus (GPa)	Elongation at break (%)
0	1.8 ± 0.2	99.8 ± 7.3	5.5 ± 0.3
5	3.2 ± 0.4	105.2 ± 4.3	3.2 ± 0.2
10	3.3 ± 0.2	107.6 ± 6.4	3.7 ± 0.1
20	2.9 ± 0.5	102.7 ± 3.2	3.5 ± 0.1

Table S3. Mechanical properties of F-CNTFs treated in a CSA bath with different stretching ratios.

Stretching ratio (%)	Tensile strength (GPa)	Young's modulus (GPa)	Elongation at break (%)
5	3.1 ± 0.2	103.4 ± 7.9	4.1 ± 0.5
10	3.3 ± 0.3	105.3 ± 5.8	5.1 ± 0.6
20	3.6 ± 0.3	110.5 ± 8.3	4.2 ± 0.4
25	2.9 ± 0.1	102.7 ± 7.1	3.1 ± 0.1

Table S4. Full width at half maximum (FWHM) and Herman's orientation factor (*f*) of F-CNTFs without the progressive stretching treatment and fibers obtained by the progressive stretching treatment with different stretching rates.

Stretching rate (% min^{-1})	FWHM (degree)	*f*
Without the progressive stretching treatment	17.1	0.66
6	14.1	0.81
4	12.9	0.85
3	12.3	0.90

Table S5. Mechanical properties of F-CNTFs without the progressive stretching treatment and fibers obtained by the progressive stretching treatment with different stretching rates.

Stretching rate (% min^{-1})	Tensile strength (GPa)	Young's modulus (GPa)	Toughness (MJ m^{-3})
Without the progressive stretching treatment	1.8 ± 0.2	99.8 ± 7.3	82.5 ± 6.4
6	3.6 ± 0.3	113.7 ± 6.4	96.1 ± 4.2
4	4.1 ± 0.4	121.5 ± 10.1	105.4 ± 9.6
3	4.5 ± 0.2	130.8 ± 7.5	111.1 ± 7.1

Table S6. N, C, O, H, and PBO contents of PBO-CNTFs treated in different PBO concentrations.

PBO concentration (wt%)	N (wt%)	C (wt%)	O (wt%)	H (wt%)	PBO (wt%)
0.025	0.73	68.67	12.47	2.73	6.1
0.05	1.08	63.15	11.75	2.29	9.1
0.1	1.02	66.49	10.73	2.63	8.6

Table S7. Mechanical properties of F-CNTFs treated by the progressive stretching treatment in PBOs-CSA solutions with the PBO concentration of 0.025 wt% (PBO-a-CNTFs), 0.05 wt% (PBO-b-CNTFs), 0.1 wt% (PBO-c-CNTFs), and further mechanical densification (D-PBO-CNTFs).

Sample	Tensile strength (GPa)	Young's modulus (GPa)	Elongation at break (%)
PBO-a-CNTFs	5.1 ± 0.1	154.3 ± 4.5	4.7 ± 0.4
PBO-b-CNTFs	5.7 ± 0.2	167.4 ± 10.1	4.0 ± 0.7
PBO-c-CNTFs	5.3 ± 0.1	159.6 ± 6.3	4.2 ± 0.6
D-PBO-CNTFs	8.2 ± 0.2	172.7 ± 9.6	5.0 ± 0.6

Table S8. FWHM and Herman's orientation factors (*f*) of F-CNTFs, CSA-CNTFs, PBO-CNTFs, and D-PBO-CNTFs.

Sample	FWHM (degree)	*f*
F-CNTFs	17.1 ± 0.7	0.66 ± 0.03
CSA-CNTFs	12.3 ± 0.2	0.90 ± 0.01
PBO-CNTFs	9.8 ± 0.3	0.94 ± 0.02
D-PBO-CNTFs	11.0 ± 0.2	0.92 ± 0.01

Table S9. Average cross-sectional areas, tensile loadings, quasi-static mechanical properties, densities (measured by the density gradient column method) (*29*), and electrical conductivities of F-CNTFs, CSA-CNTFs, PBO-CNTFs, and D-PBO-CNTFs.

Sample	Average cross-sectional area (μm^2)	Tensile loading (N)	Strength (GPa)	Young's modulus (GPa)	Toughness (MJ m^{-3})	Density (g cm^{-3})	Electrical conductivity ($\times 10^6$ S m^{-1})
F-CNTFs	611.1	1.10 ± 0.12	1.8 ± 0.2	99.8 ± 7.3	82.5 ± 6.4	1.10	0.5
CSA-CNTFs	346.1	1.56 ± 0.06	4.5 ± 0.2	130.8 ± 7.5	111.1 ± 7.1	1.24	3.5
PBO-CNTFs	350.9	2.00 ± 0.07	5.7 ± 0.2	167.4 ± 10.1	142.5 ± 12.9	1.28	2.2
D-PBO-CNTFs	300.8	2.46 ± 0.06	8.2 ± 0.2	172.7 ± 9.6	170.3 ± 17.9	1.43	2.9

Table S10. Linear densities, densities (obtained by dividing the linear density by the cross-sectional area), specific strength, and specific moduli of different fibers.

Sample	Liner density (tex)	Specific strength (N tex^{-1})	Specific modulus (N tex^{-1})	Density (g cm^{-3})
F-CNTFs	0.641	1.7 ± 0.2	94.4 ± 5.2	1.05
CSA-CNTFs	0.426	3.8 ± 0.1	105.7 ± 6.1	1.23
PBO-CNTFs	0.441	4.5 ± 0.2	130.5 ± 7.4	1.26
D-PBO-CNTFs	0.421	5.8 ± 0.1	122.4 ± 5.9	1.40

Table S11. Comparison of mechanical properties of different fibers.

Sample	Density ($g\ cm^{-3}$)	Young's modulus (GPa)	Tensile strength (GPa)	Elongation at break (%)	Cunniff velocity ($m\ s^{-1}$)	Ref.
F-CNTFs	1.10	99.8 ± 7.3	1.8 ± 0.2	5.5 ± 0.4	754.0	**This work**
CSA-CNTs	1.24	130.8 ± 7.5	4.5 ± 0.2	3.5 ± 0.1	867.2	
PBO-CNTFs	1.28	167.4 ± 10.1	5.7 ± 0.2	4.0 ± 0.7	1006.1	
D-PBO-CNTFs	1.43	172.7 ± 9.6	8.2 ± 0.2	5.0 ± 0.6	1163.6	
UHMWPE fibers (SK76)	0.97	116.0	3.6	3.8	917.0	(*4*)
Carbon fibers (T1100G)	1.80	324.0	7.0	2.0	805.1	
Kevlar KM2 fibers	1.44	85.0	3.9	4.5	776.5	
PBO fibers (Zylon AS)	1.54	180.0	5.8	3.5	893.2	
M5 fibers (M5-HT)	1.70	330.0	5.5	1.7	726.3	
Carbon fibers (M60J)	1.93	588.0	3.8	0.7	493.6	

Table S12. Mechanical properties of various fibers under different strain rates.

Sample	Strain rate (s^{-1})	Strength (GPa)	Strain rate (s^{-1})	Strength (GPa)	Strain rate (s^{-1})	Strength (GPa)	Strain rate (s^{-1})	Strength (GPa)	Toughness (MJ m^{-3})	Ref.
F-CNTFs	0.001	1.8 ± 0.2	500	1.9 ± 0.2	950	2.0 ± 0.1	1400	2.3 ± 0.1	80.5 ± 21.3	This work
CSA-CNTFs		4.5 ± 0.2		4.8 ± 0.4		5.1 ± 0.6		6.0 ± 0.6	149.2 ± 24.9	
PBO-CNTFs		5.7 ± 0.2		7.2 ± 0.4		9.5 ± 0.5		10.0 ± 0.6	320.4 ± 104.7	
D-PBO-CNTFs		8.2 ± 0.2		9.2 ± 0.8		11.0 ± 0.7		14.0 ± 0.7	462.6 ± 102.1	
PBO fibers		6.5 ± 0.1		-		7.1 ± 0.9		7.2 ± 0.8	295.0 ± 59.5	
Kevlar 29 fibers		4.2 ± 0.3		-		4.5 ± 0.4		4.6 ± 0.2	174.6 ± 11.6	
Kevlar 129 fibers	-	-	-	-	1500	4.64	-	-	-	(*34*)
Kevlar KM2 fibers	0.01	3.88	-	-	1950	4.04	-	-	-	(*35*)
CNTFs	0.001	0.74	-	-	450	0.86	1300	1.04	-	(*23*)
Glass fibers	0.002	3.70	-	-	900	5.10	-	-	-	(*61*)
UHMWPE fibers	0.001	3.14	-	-	400	3.64	600	3.56	-	(*62*)
PBO fibers	0.001	6.61	-	-	720	7.01	1000	7.04	-	(*63*)
PI fibers	0.001	4.53	-	-	720	4.68	940	4.44	-	(*63*)
Aramid III fibers	0.001	4.35	-	-	750	4.48	950	4.64	-	(*63*)
CNT/Aramid fibers*	0.001	6.44	-	-	1400	7.36	-	-	-	(*3*)
CNT/Aramid fibers†	0.001	7.01	-	-	900	6.95	1400	7.49	-	(*64*)

CNT/Aramid* represents aramid fibers by a small addition of short (< 1 μm) aminated single-walled carbon nanotubes.
CNT/Aramid† represents aramid fibers by the addition of long (about 10 μm) single-walled carbon nanotubes.

Table S13. SEDP for different cross section areas (height × width) of D-PBO-CNTFs.

Cross section area (μm ×μm)	**SEDP (× 10^{13} m kg^{-1} s^{-1})**
80 × 3	11.87
3 × 80	7.85
3 × 80 (10° rotation)	7.86

Table S14. Impact-resistant performance of fibers from our measurements and literature survey.

Sample	SEDP ($\times 10^{13}$ m kg^{-1} s^{-1})	Ref.
F-CNTFs	5.2 ± 0.3	**This work**
CSA-CNTFs	6.7 ± 1.0	
PBO-CNTFs	8.7 ± 1.0	
PBO fibers	7.4 ± 0.5	
PI fibers	5.8 ± 0.3	
Nylon fibers	3.3 ± 0.2	
Kevlar fibers	5.9	(*2*)
CNTFs	6.9	
Nylon fibers	3.7	
CNT/Aramid fibers	8.2	(*3*)

Table S15. Values of γ, c_T, and ξ of different fibers in experiments. ($E_k(0)$ = 4.0 μJ)

Fibers	Aluminum	Nylon	Kevlar	CNTF
γ (°)	35	40	24	21
c_T (m s^{-1})	262	490	820	872
ξ (kg^{-1})	7.63×10^{10}	8.77×10^{10}	7.64×10^{10}	7.86×10^{10}

Table S16. Fiber properties used in finite element analysis.

Sample	Density (g cm^{-3})	E_1 (GPa)	E_2 (GPa)	G_{12} (GPa)	μ_1	μ_2
CSA-CNTFs	1.24	130.8	10	24.4	0.6	0.24
PBO-CNTFs	1.28	167.2	10	24.4	0.6	0.24
D-PBO-CNTFs	1.43	172.7	10	24.4	0.6	0.24

Table S17. Parameters used in the coarse-grained molecular dynamics model.

Parameters	CNT	PBO	CNT-PBO
Equilibrium bead distance R_0 (Å)	30	15	
Tensile stiffness parameter K_T (kcal mol^{-1} Å^2)	3548	1872	
Equilibrium angle θ (°)	180	180	
Bending stiffness parameter K_B (kcal mol^{-1})	775108	122340	
Van der Waals parameter ε (kcal mol^{-1})	61	12	50
Van der Waals parameter σ (Å)	34	18	28

Movie Captions

Movie S1. 3D observation of reconstructed void microstructure derived from nano-CT of F-CNTFs.

Movie S2. 3D observation of reconstructed void microstructure derived from nano-CT of PBO-CNTFs.

Movie S3. 3D observation of reconstructed void microstructure derived from nano-CT of CSA-CNTFs.

Movie S4. 3D observation of reconstructed void microstructure derived from nano-CT of D-PBO-CNTFs.

References and Notes

1. S. Eswarappa Prameela, T. S. Pollock, D. Raabe, M. A. Meyers, A. Aitkaliyeva, K. Chintersingh, Z. C. Cordero, L. Graham-Brady, Materials for extreme environments. *Nat. Rev. Mater.* **8**, 81–88 (2023). doi:10.1038/s41578-022-00496-z

2. W. Xie, R. Zhang, R. J. Headrick, L. W. Taylor, S. Kooi, M. Pasquali, S. Müftü, J. H. Lee, Dynamic strengthening of carbon nanotube fibers under extreme mechanical impulses. *Nano Lett.* **19**, 3519–3526 (2019). doi:10.1021/acs.nanolett.9b00350 Medline

3. J. Luo, Y. Wen, X. Jia, X. Lei, Z. Gao, M. Jian, Z. Xiao, L. Li, J. Zhang, T. Li, H. Dong, X. Wu, E. Gao, K. Jiao, J. Zhang, Fabricating strong and tough aramid fibers by small addition of carbon nanotubes. *Nat. Commun.* **14**, 3019 (2023). doi:10.1038/s41467-023-38701-4 Medline

4. Y. Q. Li, H. L. Fan, X. L. Gao, Ballistic helmets: Recent advances in materials, protection mechanisms, performance, and head injury mitigation. *Compos. Part B* **238**, 109890 (2022). doi:10.1016/j.compositesb.2022.109890

5. B. Fang, D. Chang, Z. Xu, C. Gao, A review on graphene fibers: Expectations, advances, and prospects. *Adv. Mater.* **32**, e1902664 (2020). doi:10.1002/adma.201902664 Medline

6. I. A. Kinloch, J. Suhr, J. Lou, R. J. Young, P. M. Ajayan, Composites with carbon nanotubes and graphene: An outlook. *Science* **362**, 547–553 (2018). doi:10.1126/science.aat7439 Medline

7. B. Peng, M. Locascio, P. Zapol, S. Li, S. L. Mielke, G. C. Schatz, H. D. Espinosa, Measurements of near-ultimate strength for multiwalled carbon nanotubes and irradiation-induced crosslinking improvements. *Nat. Nanotechnol.* **3**, 626–631 (2008). doi:10.1038/nnano.2008.211 Medline

8. Y. Bai, H. Yue, J. Wang, B. Shen, S. Sun, S. Wang, H. Wang, X. Li, Z. Xu, R. Zhang, F. Wei, Super-durable ultralong carbon nanotubes. *Science* **369**, 1104–1106 (2020). doi:10.1126/science.aay5220 Medline

9. Y. Wen, M. Jian, J. Huang, J. Luo, L. Qian, J. Zhang, Carbonene fibers: Toward next-generation fiber materials. *Nano Lett.* **22**, 6035–6047 (2022). doi:10.1021/acs.nanolett.1c04878 Medline

10. J. Mu, M. Jung de Andrade, S. Fang, X. Wang, E. Gao, N. Li, S. H. Kim, H. Wang, C. Hou, Q. Zhang, M. Zhu, D. Qian, H. Lu, D. Kongahage, S. Talebian, J. Foroughi, G. Spinks, H. Kim, T. H. Ware, H. J. Sim, D. Y. Lee, Y. Jang, S. J. Kim, R. H. Baughman, Sheath-run artificial muscles. *Science* **365**, 150–155 (2019). doi:10.1126/science.aaw2403 Medline

11. H. Chu, X. Hu, Z. Wang, J. Mu, N. Li, X. Zhou, S. Fang, C. S. Haines, J. W. Park, S. Qin, N. Yuan, J. Xu, S. Tawfick, H. Kim, P. Conlin, M. Cho, K. Cho, J. Oh, S. Nielsen, K. A. Alberto, J. M. Razal, J. Foroughi, G. M. Spinks, S. J. Kim, J. Ding, J. Leng, R. H. Baughman, Unipolar stroke, electroosmotic pump carbon nanotube yarn muscles. *Science* **371**, 494–498 (2021). doi:10.1126/science.abc4538 Medline

12. C. Chen, J. Feng, J. Li, Y. Guo, X. Shi, H. Peng, Functional fiber materials to smart fiber devices. *Chem. Rev.* **123**, 613–662 (2023). doi:10.1021/acs.chemrev.2c00192 Medline

13. L. W. Taylor, S. M. Williams, J. S. Yan, O. S. Dewey, F. Vitale, M. Pasquali, Washable, sewable, all-carbon electrodes and signal wires for electronic clothing. *Nano Lett.* **21**, 7093–7099 (2021). doi:10.1021/acs.nanolett.1c01039 Medline

14. N. Behabtu, C. C. Young, D. E. Tsentalovich, O. Kleinerman, X. Wang, A. W. K. Ma, E. A. Bengio, R. F. ter Waarbeek, J. J. de Jong, R. E. Hoogerwerf, S. B. Fairchild, J. B. Ferguson, B. Maruyama, J. Kono, Y. Talmon, Y. Cohen, M. J. Otto, M. Pasquali, Strong, light, multifunctional fibers of carbon nanotubes with ultrahigh conductivity. *Science* **339**, 182–186 (2013). doi:10.1126/science.1228061 Medline

15. S. G. Kim, G. M. Choi, H. D. Jeong, D. J. Lee, S. Y. Kim, K. H. Ryu, S. H. Lee, J. W. Kim, J. Y. Hwang, N. D. Kim, D. Y. Kim, H. S. Lee, B. C. Ku, Hierarchical structure control in solution spinning for strong and multifunctional carbon nanotube fibers. *Carbon* **196**, 59–69 (2022). doi:10.1016/j.carbon.2022.04.040

16. M. Zhang, K. R. Atkinson, R. H. Baughman, Multifunctional carbon nanotube yarns by downsizing an ancient technology. *Science* **306**, 1358–1361 (2004). doi:10.1126/science.1104276 Medline

17. Y. L. Li, I. A. Kinloch, A. H. Windle, Direct spinning of carbon nanotube fibers from chemical vapor deposition synthesis. *Science* **304**, 276–278 (2004). doi:10.1126/science.1094982 Medline

18. H. G. Chae, S. Kumar, Making strong fibers. *Science* **319**, 908–909 (2008). doi:10.1126/science.1153911 Medline

19. K. Koziol, J. Vilatela, A. Moisala, M. Motta, P. Cunniff, M. Sennett, A. Windle, High-performance carbon nanotube fiber. *Science* **318**, 1892–1895 (2007). doi:10.1126/science.1147635 Medline

20. W. Xu, Y. Chen, H. Zhan, J. N. Wang, High-strength carbon nanotube film from improving alignment and densification. *Nano Lett.* **16**, 946–952 (2016). doi:10.1021/acs.nanolett.5b03863 Medline

21. J. J. Vilatela, J. A. Elliott, A. H. Windle, A model for the strength of yarn-like carbon nanotube fibers. *ACS Nano* **5**, 1921–1927 (2011). doi:10.1021/nn102925a Medline

22. D. Y. Wang, P. F. Wang, Y. F. Wu, L. H. Bu, J. Tian, M. Liu, G. Z. Sun, L. Mei, S. L. Xu, Temperature and rate-dependent plastic deformation mechanism of carbon nanotube fiber: Experiments and modeling. *J. Mech. Phys. Solids* **173**, 105241–105267 (2023). doi:10.1016/j.jmps.2023.105241

23. P. F. Wang, X. Zhang, R. V. Hansen, G. Z. Sun, H. Zhang, L. X. Zheng, T. X. Yu, G. X. Lu, J. L. Yang, Strengthening and failure mechanisms of individual carbon nanotube fibers under dynamic tensile loading. *Carbon* **102**, 18–31 (2016). doi:10.1016/j.carbon.2016.02.009

24. X. P. Hu, Y. X. Zheng, D. Y. Wang, G. Z. Sun, X. H. Zhang, J. Tian, P. F. Wang, S. L. Xu, F. H. Zhou, Uncovering the mechanical behavior of twisted carbon nanotube assemblies under high-speed stretching. *Compos. Commun.* **28**, 100933 (2021). doi:10.1016/j.coco.2021.100933

25. Y. Jung, Y. S. Cho, J. W. Lee, J. Y. Oh, C. R. Park, How can we make carbon nanotube yarn stronger? *Compos. Sci. Technol.* **166**, 95–108 (2018). doi:10.1016/j.compscitech.2018.02.010

26. J. S. Bulmer, A. Kaniyoor, J. A. Elliott, A meta-analysis of conductive and strong carbon nanotube materials. *Adv. Mater.* **33**, e2008432 (2021). doi:10.1002/adma.202008432 Medline

27. J. Lee, D. M. Lee, Y. Jung, J. Park, H. S. Lee, Y. K. Kim, C. R. Park, H. S. Jeong, S. M. Kim, Direct spinning and densification method for high-performance carbon nanotube fibers. *Nat. Commun.* **10**, 2962 (2019). doi:10.1038/s41467-019-10998-0 Medline

28. X. Zhang, M. De Volder, W. Zhou, L. Issman, X. Wei, A. Kaniyoor, J. Terrones Portas, F. Smail, Z. Wang, Y. Wang, H. Liu, W. Zhou, J. Elliott, S. Xie, A. Boies, Simultaneously enhanced tenacity, rupture work, and thermal conductivity of carbon nanotube fibers by raising effective tube portion. *Sci. Adv.* **8**, eabq3515 (2022). doi:10.1126/sciadv.abq3515 Medline

29. D. Lee, S. G. Kim, S. Hong, C. Madrona, Y. Oh, M. Park, N. Komatsu, L. W. Taylor, B. Chung, J. Kim, J. Y. Hwang, J. Yu, D. S. Lee, H. S. Jeong, N. H. You, N. D. Kim, D. Y. Kim, H. S. Lee, K. H. Lee, J. Kono, G. Wehmeyer, M. Pasquali, J. J. Vilatela, S. Ryu, B. C. Ku, Ultrahigh strength, modulus, and conductivity of graphitic fibers by macromolecular coalescence. *Sci. Adv.* **8**, eabn0939 (2022). doi:10.1126/sciadv.abn0939 Medline

30. Y. J. Wang, S. Xia, H. Li, J. F. Wang, Unprecedentedly tough, folding-endurance, and multifunctional graphene-based artificial nacre with predesigned 3D nanofiber network as matrix. *Adv. Funct. Mater.* **29**, 1903876 (2019). doi:10.1002/adfm.201903876

31. Materials and methods are available as supplementary materials.

32. J. Qiu, J. Terrones, J. J. Vilatela, M. E. Vickers, J. A. Elliott, A. H. Windle, Liquid infiltration into carbon nanotube fibers: Effect on structure and electrical properties. *ACS Nano* **7**, 8412–8422 (2013). doi:10.1021/nn401337m Medline

33. Y. N. Zhang, L. X. Zheng, G. Z. Sun, Z. Y. Zhan, K. Liao, Failure mechanisms of carbon nanotube fibers under different strain rates. *Carbon* **50**, 2887–2893 (2012). doi:10.1016/j.carbon.2012.02.057

34. J. Lim, W. W. Chen, J. Q. Zheng, Dynamic small strain measurements of Kevlar 129 single fibers with a miniaturized tension Kolsky bar. *Polym. Test.* **29**, 701–705 (2010). doi:10.1016/j.polymertesting.2010.05.012

35. M. Cheng, W. N. Chen, T. Weerasooriya, Mechanical properties of Kevlar KM2 single fiber. *J. Eng. Mater. Technol.* **127**, 197–203 (2005). doi:10.1115/1.1857937

36. W. B. Lu, T. Chou, B. Kim, Radial deformation and its related energy variations of single-walled carbon nanotubes. *Phys. Rev. B* **83**, 134113 (2011). doi:10.1103/PhysRevB.83.134113

37. N. G. Chopra, L. X. Benedict, V. H. Crespi, M. L. Cohen, S. G. Louie, A. Zettl, Fully collapsed carbon nanotubes. *Nature* **377**, 135–138 (1995). doi:10.1038/377135a0

38. S. Ozden, P. A. S. Autreto, C. S. Tiwary, S. Khatiwada, L. Machado, D. S. Galvao, R. Vajtai, E. V. Barrera, P. M. Ajayan, Unzipping carbon nanotubes at high impact. *Nano Lett.* **14**, 4131–4137 (2014). doi:10.1021/nl501753n Medline

39. N. Fakhri, D. A. Tsyboulski, L. Cognet, R. B. Weisman, M. Pasquali, Diameter-dependent bending dynamics of single-walled carbon nanotubes in liquids. *Proc. Natl. Acad. Sci. U.S.A.* **106**, 14219–14223 (2009). doi:10.1073/pnas.0904148106 Medline

40. D. B. Roitman, M. McAdon, Persistence length of the "rodlike" molecule poly(p-phenylene-trans-benzobisthiazole) revisited. *Macromolecules* **26**, 4381–4383 (1993). doi:10.1021/ma00068a050

41. H. D. Jeong, S. G. Kim, G. M. Choi, M. Park, B. C. Ku, H. S. Lee, Theoretical and experimental investigation of the wet-spinning process for mechanically strong carbon nanotube fibers. *Chem. Eng. J.* **412**, 128650 (2021). doi:10.1016/j.cej.2021.128650

42. R. J. Headrick, D. E. Tsentalovich, J. Berdegué, E. A. Bengio, L. Liberman, O. Kleinerman, M. S. Lucas, Y. Talmon, M. Pasquali, Structure-property relations in carbon nanotube fibers by downscaling solution processing. *Adv. Mater.* **30**, 1704482 (2018). doi:10.1002/adma.201704482 Medline

43. J. D. Cole, C. B. Dougherty, J. H. Huth, Constant-strain waves in strings. *J. Appl. Mech.* **20**, 519–522 (1953). doi:10.1115/1.4010758

44. J. C. Smith, F. L. McCrackin, H. F. Schiefer, Stress-strain relationships in yarns subjected to rapid impact loading: Part V: Wave propagation in long textile yarns impacted transversely. *Text. Res. J.* **28**, 288–302 (1958). doi:10.1177/004051755802800402

45. B. Song, H. Park, W. Y. Lu, W. N. Chen, Transverse impact response of a linear elastic ballistic fiber yarn. *J. Appl. Mech.* **78**, 051023 (2011). doi:10.1115/1.4004310

46. M. R. O'Masta, V. S. Deshpande, H. N. G. Wadley, Mechanisms of projectile penetration in Dyneema encapsulated aluminum structures. *Int. J. Impact Eng.* **74**, 16–35 (2014). doi:10.1016/j.ijimpeng.2014.02.002

47. B. A. Newcomb, Processing, structure, and properties of carbon fibers. *Compos. Part A* **91**, 262–282 (2016). doi:10.1016/j.compositesa.2016.10.018

48. M. Lammers, E. A. Klop, M. G. Northolt, D. J. Sikkema, Mechanical properties and structural transitions in the new rigid-rod polymer fibre PIPD ('M5′) during the manufacturing process. *Polymer* **39**, 5999–6005 (1998). doi:10.1016/S0032-3861(98)00021-4

49. M. Afshari, D. J. Sikkema, K. Lee, M. Bogle, High performance fibers based on rigid and flexible polymers. *Polym. Rev.* **48**, 230–274 (2008). doi:10.1080/15583720802020129

50. G. A. Holmes, K. Rice, C. R. Snyder, Ballistic fibers: A review of the thermal, ultraviolet and hydrolytic stability of the benzoxazole ring structure. *J. Mater. Sci.* **41**, 4105–4116 (2006). doi:10.1007/s10853-005-5597-1

51. W. Lu, M. Zu, J. H. Byun, B. S. Kim, T. W. Chou, State of the art of carbon nanotube fibers: Opportunities and challenges. *Adv. Mater.* **24**, 1805–1833 (2012). doi:10.1002/adma.201104672 Medline

52. B. Farsi Dooraki, J. A. Nemes, M. Bolduc, Study of parameters affecting the strength of yarns. *J. Phys. IV* **134**, 1183–1188 (2006). doi:10.1051/jp4:2006134180

53. S. Plimpton, Fast parallel algorithms for short-range molecular dynamics. *J. Comput. Phys.* **117**, 1–19 (1995). doi:10.1006/jcph.1995.1039

54. H. Sun, S. J. Mumby, J. R. Maple, A. T. Hagler, An ab initio CFF93 all-atom force field for polycarbonates. *J. Am. Chem. Soc.* **116**, 2978–2987 (1994). doi:10.1021/ja00086a030

55. R. W. Hockney, J. W. Eastwood, *Computer Simulation Using Particles* (CRC Press, 1988).

56. L. Liu, Y. Gao, Q. Liu, J. Kuang, D. Zhou, S. Ju, B. Han, Z. Zhang, High mechanical performance of layered graphene oxide/poly(vinyl alcohol) nanocomposite films. *Small* **9**, 2466–2472 (2013). doi:10.1002/smll.201300819 Medline

57. Y. L. Liu, B. Xie, Z. Zhang, Q. S. Zheng, Z. P. Xu, Mechanical properties of graphene papers. *J. Mech. Phys. Solids* **60**, 591–605 (2012). doi:10.1016/j.jmps.2012.01.002

58. O. K. Park, W. Y. Kim, S. M. Kim, N. H. You, Y. Jeong, H. S. Lee, B. C. Ku, Effect of oxygen plasma treatment on the mechanical properties of carbon nanotube fibers. *Mater. Lett.* **156**, 17–20 (2015). doi:10.1016/j.matlet.2015.04.141

59. E. L. Gao, S. J. Wang, C. H. Duan, Z. P. Xu, Microstructural ordering of nanofibers in flow-directed assembly. *Sci. China Technol. Sci.* **62**, 1545–1554 (2019). doi:10.1007/s11431-018-9421-5

60. E. L. Gao, Y. Z. Guo, Z. Z. Wang, S. O. Nielsen, R. H. Baughman, The strongest and toughest predicted materials: Linear atomic chains without a Peierls instability. *Matter* **5**, 1192–1203 (2022). doi:10.1016/j.matt.2022.01.021

61. S. Tamrakar, B. Z. (Gama) Haque, J. W. Gillespie, High rate test method for fiber-matrix interface characterization. *Polym. Test.* **52**, 174–183 (2016). doi:10.1016/j.polymertesting.2016.04.016

62. M. Hudspeth, X. Nie, W. N. Chen, Dynamic failure of Dyneema SK76 single fibers under biaxial shear/tension. *Polymer* **53**, 5568–5574 (2012). doi:10.1016/j.polymer.2012.09.020

63. X. Lei, K. Xiao, X. Wu, C. Huang, Dynamic mechanical properties of several high-performance single fibers. *Materials* **14**, 3574 (2021). doi:10.3390/ma14133574 Medline

64. D. Yan, J. Luo, S. Wang, X. Han, X. Lei, K. Jiao, X. Wu, L. Qian, X. Zhang, X. Zhao, J. Di, Z. Zhang, Z. Gao, J. Zhang, Carbon nanotube-directed 7 GPa heterocyclic aramid fiber and its application in artificial muscles. *Adv. Mater.* **2306129**, e2306129 (2023). doi:10.1002/adma.202306129 Medline